OPTICAL DIFFERENCE FREQUENCY GENERATION OF FAR INFRARED RADIATION

James Russell Morris
(Ph. D. thesis)

July 1977

Prepared for the U. S. Energy Research and
Development Administration under Contract W-7405-ENG-48

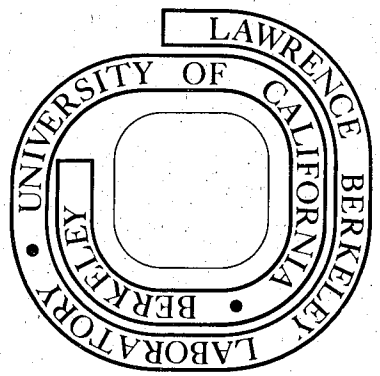

OPTICAL DIFFERENCE FREQUENCY GENERATION OF FAR INFRARED RADIATION

James Russell Morris

Materials and Molecular Research Division, Lawrence Berkeley Laboratory
and Department of Physics; University of California
Berkeley, California 94720

ABSTRACT

Three investigations of difference frequency generation (DFG) of far-infrared radiation by optical mixing are described: a theory of DFG by monochromatic, focused Gaussian pump laser beams, a theory of DFG by a picosecond pump laser pulse, and an experiment using ruby-pumped dye lasers. First, the theory of far-infrared generation by optical mixing of monochromatic, focused Gaussian beams in a uniaxial crystal is developed, taking into account the effects of diffraction, absorption, double refraction, and multiple reflections and total reflection at the boundary surfaces. (Reflection and transmission coefficients of a uniaxial crystal slab are derived by a new matrix technique.) Results of numerical calculations are presented. Focusing the pump beams appreciably enhances the far-infrared output despite the strong far-infrared diffraction. In a 1-cm long crystal, the optimum focal spot size is approximately equal to or smaller than the far-infrared wavelength for output frequencies less than 100 cm^{-1}. Double refraction of the pump beams is relatively unimportant. Both far-infrared absorption and boundary reflections have major effects on the far-infrared output and its angular distribution. The former is often the factor

which limits the output power. We show that a simple model treating the nonlinear polarization as a constant 1/e-radius Gaussian distribution of radiating dipoles adequately describes the effect of pump-beam focusing. We also compare the results of our calculations with those for second-harmonic generation. Second, a theoretical calculation of far-infrared power spectra generated by picosecond pulses in a nonlinear crystal is developed. The results are illustrated with two practical examples: $LiNbO_3$ slabs oriented for rectification of the optical e-ray and for beating of the optical o-ray with the optical e-ray. The former is phase matched at 0 cm^{-1}; the latter, at both the forward-(FCPM) and backward-collinear phase-matching frequencies. The one-dimensional, time-dependent electric field is discussed and then used to explain the origin of the oscillation periods in the power spectra. Finally, a series of experiments using a pair of ruby-pumped dye lasers and a novel dual-frequency dye laser system is described. With these two laser systems, continuously tunable far-infrared radiation in the frequency range 20 to 190 cm^{-1} was generated. Forward-, backward-, and non-collinear phasematching in $LiNbO_3$ at frequencies between 20 and 160 cm^{-1} were investigated; 90° noncritical FCPM was also observed in ZnO at 190 cm^{-1}, CdS at 180 cm^{-1}, and ZnS at 91 cm^{-1}. The highest peak power (~200 mW) and the broadest tuning range using a single crystal sample (40 to 160 cm^{-1}) were obtained with noncollinear phase matching in $LiNbO_3$.

CONTENTS

CHAPTER I. DIFFERENCE FREQUENCY GENERATION OF FAR-INFRARED RADIATION AS A NONLINEAR OPTICS RESEARCH TOPIC

I. Introduction

For the purposes of this thesis, optical difference frequency generation is defined as a process in which two optical waves mix in an electro-optic crystal to create a third electromagnetic wave at their difference frequency. There are three fundamental reasons why investigation of this process has been an active area of nonlinear optics research for over a decade. First, the generation process itself differs from second harmonic generation (SHG) enough to require a separate analysis. When the pump frequencies are a factor of ten or more larger than the difference frequency as in typical far-infrared generation experiments, the large diffraction angle of the difference frequency wave compared to the pump waves can make the approximations used to describe SHG inapplicable. Second, the dispersion of the DFG susceptibility provides data on the low frequency excitations of the nonlinear crystal (e.g., magnons and phonons) which do not contribute to the optical or near-infrared SHG susceptibilities. Finally, DFG is a means of transferring the tunability of optical lasers or parametric oscillators into lower frequency regions where tunable bright coherent sources have not yet been developed.

Since the 1920s, radio engineers have known how to generate coherent radiation from a few kHz to 100 MHz or more. In the 1930s, the split-anode magnetron extended radio frequency techniques to cm wavelengths, and in response to the need for cm wavelength radar, the klystron,

the multicavity magnetron, and the traveling wave tube - invented during the World War II years - extended the wavelength range to the millimeter regime. After the war, these techniques were pushed into sub-millimeter wavelengths so that now carcinotrons can reach 350 μm.[1] At the other end of the spectrum from the near-ultraviolet down through the near-infrared, organic dye lasers have provided bright tunable sources while parametric oscillators and spin-flip Raman lasers cover a region that extends down into the medium-infrared.

The 30 to 500 cm^{-1} (333 to 20 μm wavelength) part of the far-infrared region has proved more resistent to the development of bright tunable sources using either radio frequency or optical techniques. For decades one of the best radiation sources for far-infrared spectroscopy has been the quartz envelope high-pressure mercury arc lamp; when used in Fourier transform spectroscopy, it is still the most versatile far-infrared source. An ideal 5000°K blackbody of 1 cm^2 surface area is a convenient source to compare with, since between 30 and 70 cm^{-1} the high-pressure mercury arc radiates like a 5000 to 6000°K blackbody. (By 150 cm^{-1} its effective temperature has dropped to 1000°K.[2]) Although its total radiated power is 3.5 kW, only 0.54 W or 0.015% of this power is in the 30 to 500 cm^{-1} spectral region and only 0.13 mW is in a 1 cm^{-1} bandwidth at 100 cm^{-1}.

Many quantum electronic systems generate coherent far-infrared radiation without using difference frequency generation. Glow discharge pumped HCN, H_2O, H_2S, and SO_2 molecular gas lasers[3] provide bright coherent continuous wave (cw) or repetitively pulsed sources. Since

they are not tunable, they are of limited use for spectroscopy. Optically pumped molecular gas lasers[4] offer more promise as a spectroscopic source. With a single TEA CO_2 pump laser, many organic molecules can be made to lase - each at its own far-infrared wavelength. Although these sources are not tunable either, the sheer number of such wavelengths should make such a system useful for low resolution spectroscopy of broad band transitions and high resolution spectroscopy of line transitions (by means of a Stark shift, etc.). PbSe and $Pb_{1-x}Sn_xTe$ semiconductor p-n junction lasers have been operated in the far-infrared.[1] The PbSe laser has been pressure tuned from 455 to 1370 cm^{-1};[5,6] so a $Pb_{1-x}Sn_xTe$ laser system[7] might be pressure tunable over a significant part of the far-infrared. Stimulated Raman and stimulated polariton scattering have also provided tunable far-infrared sources.[8,9] Very recently, far-infrared radiation has also been observed in the output of the InSb spin-flip Raman laser.[9,10]

Relativistic electron beams can also generate far-infrared radiation at harmonics of the accelerator bunching frequency[11] or at a wavelength approximately equal to the Doppler-shifted period of a spatially periodic magnetic field.[12] The harmonics of the bunching frequency can be generated, for example, as Cerenkov radiation in a waveguide loaded with a periodic slow wave structure.[11] The Doppler shifted schemes have been of more interest lately due to the possibility of free-electron laser action[13] and a potentially much larger tuning range. Elias et al.[12] have measured a gain of 0.07 per pass at 10.6 μm using a 70 mA instantaneous peak electron current, 24 MeV electron beam

in a 5.2 m long, 3.2 cm pitch, 2.4 kG helical magnetic field. Using the same magnet with a 1 amp, 8 MeV electron beam, the output wavelength and the gain per pass would be 95 μm (105 cm^{-1} frequency) and e^{27}, respectively. Unfortunately, electron accelerators capable of reaching relativistic energies are expensive to build and operate; thus, far-infrared sources based on relativistic electron beams will probably be feasible, if at all, only at laboratories that possess the necessary accelerator for other purposes.

The experimental observations of far-infrared generation by nonlinear optical difference frequency mixing can be sorted into two groups by the spectral characteristics of the pump source. In the first group of experiments, the Fourier components of a single broad bandwidth laser form the pump source. With such a laser Zernike and Berman[14] observed the first reported nonlinear optical difference frequency generation of far-infrared radiation in 1965. They illuminated a quartz crystal that was cut for collinear phase matching at ~100 cm^{-1} with the broad bandwidth output of a free-running Nd^{+3}:glass laser and observed random difference frequency spikes. Yajima and Takeuchi[15] reported observing the far-infrared radiation generated by a Q-switched Nd^{+3}:glass laser in $LiNbO_3$ in their paper on DFG by picosecond pulses. Yajima and Takeuchi,[15,16] Yang et al.,[17] and Takeuchi et al.[18] have observed the self-beating of the frequency components of a picosecond mode-locked Nd^{+3} : glass laser pulse in various crystals: $LiNbO_3$,[15-17] ZnTe,[15,16] ZnSe,[15] CdS,[15] quartz,[15] and $LiIO_3$;[18] these experiments have demonstrated a means of generating tunable far-infrared pulses

a few tens of picoseconds in duration. More recently, Matsumoto and Yajima[19] have reported far-infrared generation in ZnTe, $LiNbO_3$, and ZnSe using the output of broad bandwidth ruby-pumped dye lasers.

The second group, which includes the majority of far-infrared generation by difference frequency mixing experiments, uses two nearly monochromatic pump beams. Such experiments have been reported by over half a dozen research groups under a wide variety of experimental conditions in the twelve years since Zernike and Berman's experiment. Many different combinations of laser systems and nonlinear crystals have been used to investigate the DFG process: CO_2 laser lines in InSb,[20-25] GaAs,[26-42] and $ZnGeP_2$;[43] a CO_2 laser and a spin-flip Raman laser beam in InSb;[44-49] R_1 and R_2 lines from a specially constructed ruby laser in ZnTe;[50-52] temperature tuned ruby laser lines from a pair of simultaneously Q-switched ruby lasers in $LiNbO_3$[53-57] and quartz;[53] ruby-pumped Raman lasers in GaP;[58-60] and ruby-pumped dye lasers in $LiNbO_3$, ZnO, ZnS, and CdS[61-63] and in reduced (black) $LiNbO_3$.[64]

The most common experimental scheme uses collinear pump beams and generates a far-infrared wave that propagates in the same direction as the pump waves. Usually the mixing process is phase matched for efficient far-infrared generation, but in a few experiments[20,25,28,50-52] phase matching was unnecessary; in most of these cases the coherence length for far-infrared generation was longer than the effective sample length due to either a fortunate coincidence[20,28,50-52] or to a large optical absorption coefficient.[64] Usually collinear phase matching is attained through the dependence of the birefringence of uniaxial crystals

on their orientation. This mechanism doesn't exist in isotropic crystals, so various ingenious methods have been employed to achieve collinear phase matching: Nguyen and Patel[22,23] used a static magnetic field to induce birefringence in InSb through the Voigt[22] or Faraday[23] effects; Zernike[21] temperature tuned the 9.6 and 10.6 μ refractive indices of InSb; Nguyen and Bridges[44-48] used the free carrier concentration (by selecting a properly doped sample) to set the plasma frequency and hence the 9.6 and 10.6 μ refractive indices of InSb; finally, Thompson and Coleman,[29-31] the Bell Labs groups,[26,27] and Bogatkin et al.[32] have used the waveguide dispersion of GaAs (or GaAs filled) waveguides.

In isotropic materials the most generally useful phase matching technique is noncollinear phase matching (NCPM) in which a slight angle between the pump beams is used to compensate for the higher far-infrared refractive index. Of course, NCPM can also be used in birefringent crystals. DeMartini,[58-60] the Berkeley group,[62] and the National Magnet Lab group[34-42] have successfully employed this technique; the latter two groups have demonstrated that far-infrared generation in the NCPM geometry can be very efficient. In particular, the Magnet Lab group has developed a folded noncollinear geometry,[39-42] a modification of the multiple internal reflection scheme first suggested by Armstrong et al.,[65] in which the pump beams propagate in a zig-zag pattern down a long crystal with a rectangular cross section while the far-infrared beam propagates parallel to the long axis of the sample. This scheme has increased the far-infrared power that can be obtained from mixing CO_2 lasers in GaAs by several orders of magnitude while

preserving the convenient "one crystal works for all difference frequencies" feature of noncollinear phase matching in an isotropic crystal. With this efficient folded geometry Aggarwal et al.[41,42] have generated continuous wave far-infrared radiation that is step-tunable from 10 to 140 cm^{-1} with less than a 100 kHz bandwidth at significant power levels; at 100 cm^{-1} two 25W CO_2 lasers generated ~.2 μW of far-infrared power.

The largest group of theoretical papers on DFG of far-infrared radiation have treated the two pump beams and the far-infrared wave as diffractionless apertured plane waves. De Martini[60] discussed DFG in an isotropic medium for a pair of plane pump waves with a common plane of incidence when the nonlinear polarization vector is perpendicular to this plane. He has included the far-infrared absorption and the polariton dispersion of both the linear and nonlinear susceptibilities as well as the single surface boundary conditions.[66] Shen[10] has discussed the connection between DFG and stimulated polariton scattering due to the spin-flip Raman transition in InSb and has shown that the interference between the resonant magnetic dipole and the non-resonant electric dipole terms of the nonlinear difference frequency susceptibility explains the asymmetry of the experimentally measured[25] dependence of the difference frequency power on the static magnetic field strength. In an earlier paper, Brown and Wolff[67] have discussed the resonant magnetic dipole DFG process by itself. Paraire et al.[56] have generalized the plane wave solution to treat a wedge-shaped sample of a uniaxial crystal in the special case when

the c-axis is normal to the input surface and the pump wave vectors, the surface normal vectors, and the c-axis are all coplanar. They discuss generation of both far-infrared o- and e-rays, single surface reflection and transmission at the output surface of the wedge, and the dispersion of the nonlinear susceptibility.

Prior to the research discussed in chapter II, several models which include diffraction effects have appeared in the literature. In their experimental papers, Zernike and Berman[14] and Faries et al.[53] used the far-field diffraction pattern of the nonlinear polarization created by a uniformly illuminated cylinder with plane wave fronts normal to the axis of the cylinder and included the effect of total reflection at the exit surface. Our results show that this model or its generalization to Gaussian beam illumination is a good description of far-infrared generation when walk-off effects are not too large. Boyd and Kleinman[68] and Faries[54] have given the nonlinear polarization for DFG by interacting Gaussian beams, but they have not given any results using this polarization. Abdullin et al.[69] have also described far-infrared generation by a pair of interacting Gaussian beams. They restricted their treatment to isotropic media and ignored boundary reflections, total reflection, and far-infrared absorption to emphasize the physical explanation of the phase matched cone seen in our calculations as Cerenkov radiation. (Note: Abdullin et al.'s power formula is an asymptotic expression that is valid only when the Cerenkov cone is significantly narrower than its opening angle.)

The theory of DFG of far-infrared radiation by picosecond optical pulses has been developed independently by Yajima and Takeuchi[15,16] and by Morris and Shen.[70] While we have emphasized the intensity variation in the far-infrared radiation by considering the case of a single coherent picosecond pump pulse, Yajima and Takeuchi have expanded the pump beam as a sum of laser cavity longitudinal modes to compare the power generated by a mode-locked (coherent case) pulse to that generated by the random fluctuations of a Q-switched Nd^{+3}:glass laser or a broad bandwidth dye laser.[19] They have also included the effect of optical dispersion which we have omitted for simplicity; for $LiNbO_3$ this merely displaces the phase matched frequencies or changes the coherence length slightly, but for crystals like ZnTe in which the difference between the optical and far-infrared refractive indices is small, it can change the coherence length appreciably. Yajima and Takeuchi have neglected the backward phase matched signal[70] without which the experimental results[15,17] for $LiNbO_3$ cannot be understood.

There are two review articles that deal with DFG. Shen's[71] review covers the status of far-infrared generation by optical mixing research up to 1974; this paper is an excellent introduction to the DFG literature. Warner's[72] review article emphasizes up-conversion and includes only a very sketchy treatment of DFG; it does, however, discuss DFG at frequencies above the far-infrared.

In the subsequent chapters of this thesis, we describe three investigations of far-infrared generation by difference frequency mixing of optical or near-infrared laser beams in nonlinear crystals -

two theoretical and one experimental. In chapter II we present a theory of far-infrared generation by difference frequency mixing of two monochromatic TEM_{oo} mode laser beams and a series of computer calculations based on this theory.[73] We discuss the important effects of a far-infrared diffraction angle that is much larger than the optical diffraction angles: loss of far-infrared power to totally reflected modes and variation of the phase mismatch from one far-infrared plane wave mode to another. We also discuss the effects of far-infrared absorption and optical walk-off, and we present the solution to the crystal-vacuum boundary conditions for a uniaxial crystal in a matrix form that focuses attention on the physical reflection processes rather than on the many simultaneous equations. In chapter III we describe a theory[70] of DFG from the beating of the Fourier components of a single picosecond pulse (or a mode-locked train of such pulses) using a quasi-plane wave approximation. We discuss two types of DFG of far-infrared radiation with picosecond pulses: (1) the propagating wave analog of optical rectification in which an optical o-ray or e-ray beats with itself and (2) the beating of an optical o-ray with an optical e-ray in which spectral narrowing due to phase matching can dominate. Both forward and backward propagating far-infrared waves are generated by this process, and reflection off the surfaces of the nonlinear crystal mixes the two waves. The theory predicts that, with an appropriately chosen backward collinear phase matching frequency, generation of the backward propagating wave should be easily observable in $LiNbO_3$ slabs less than several mm thick; this prediction and the general features of our theory have been experimentally verified by

Yang, Richards, and Shen.[17] In chapter IV, we discuss the experimental observation of far-infrared radiation from 20 to 160 cm^{-1} in $LiNbO_3$ and at the maximum forward collinear phase matching frequency in ZnO, CdS, and ZnS using two nearly monochromatic dye laser beams. Substantial signal-to-noise ratios are observed for forward collinear, backward collinear, and noncollinear phase matched DFG in $LiNbO_3$ and for forward collinear phase matched DFG in ZnO; of these, noncollinear phase matched DFG in $LiNbO_3$ is the most efficient process. The direct observation of backward collinear phase matched generation of a far-infrared wave with nearly monochromatic laser beams in $LiNbO_3$ is indisputable verification of the origin of the low frequency peak in the mixed polarization mode picosecond pulse experiment of Yang, Richards, and Shen.[17] We also describe a novel dual frequency dye laser that was developed for and used in some of these experiments. Appendicies A and B describe some of the mathematical details of chapter II. Appendix C describes the numerical methods used for the computer calculations presented in chapter II and contains a listing of the computer code. Appendix D gives the far-infrared field for the square optical pulse case discussed in chapter III. Appendix E describes the nonlinear least-squares fitting procedure used to obtain the dispersion of the o-ray far-infrared absorption coefficient from our experimental data. The remainder of this chapter describes the connection between DFG and other nonlinear optical processes.

II. Relationship Between Difference Frequency Generation of Far-Infrared Radiation and Other Nonlinear Optical Processes

Difference frequency generation, sum frequency generation, second harmonic generation, optical rectification, up-conversion, parametric amplification or oscillation, and the linear electro-optic effect are all described by the second order nonlinear susceptibility tensor and Maxwell's equations. These processes are all manifestations of a single nonlinear optical interaction in different frequency regimes and under different initial or boundary conditions. Parametric amplification, parametric oscillation, and optical rectification have especially close connections to DFG. When both parametric amplification (or oscillation) and DFG involve the same set of three frequencies, they differ only in their initial and boundary conditions. Drastically reducing the intensity of the low frequency pump (signal) beam, lengthening the nonlinear crystal sample, and enclosing the crystal in an optical resonator for the signal or idler (difference frequency) waves converts a phase matched DFG experiment into a parametric amplifier experiment. In the parametric oscillator, the signal beam builds up from spontaneous emission noise at the set of cavity modes that are most nearly phase matched.[74] Optical rectification, when observed through propagating waves, is the zero frequency limit of difference frequency generation; however, in the more common experimental arrangement optical rectification is observed as an electrical pulse across parallel capacitor plates and is thus the longitudinal or

electro-static solution to Maxwell's equations rather than the transverse, propagating wave solution observed in DFG experiments.

The electro-optic effect is the DC field limit of the combined sum- and difference-frequency processes which are degenerate when one mixing frequency is zero (i.e. when the optical input and output waves have the same frequency). When absorption at the pump and at very low far-infrared frequencies is negligible, the second order susceptibility (discussed below) obeys a permutation symmetry[65,75] and the optical rectification and electro-optic effect susceptibilities are equal.

A brief description of the pertinent part of nonlinear optical susceptibility theory[76,77] will clarify these interrelationships.

Since nonlinear optical effects are observed with high photon flux laser beams, we can use the semi-classical theory of radiation to describe the growth and propagation of the nonlinearly generated electric fields. Furthermore, because we are only concerned with effects induced by external fields, the electromagnetic field is described by Maxwell's equations in which the induced current density, $\vec{J}$, can be expanded in a multipole series[76,78]

$$\vec{J} = \frac{\partial \vec{P}}{\partial t} + c\vec{\nabla} \times \vec{M} - \frac{\partial}{\partial t} (\vec{\nabla} \cdot \overleftrightarrow{Q}) + \ldots \qquad (1)$$

where $\vec{P}$, $\vec{M}$, and $\overleftrightarrow{Q}$ are the electric dipole, magnetic dipole, and electric quadrupole polarizations, respectively. Although each of these terms can have both linear and nonlinear contributions, I shall discuss

only the electric dipole polarization term, $\partial\vec{P}/\partial t$, as this is sufficient to illustrate the phenomena that are related to difference frequency generation. To further simplify the discussion, I shall make the customary dipole or local field approximation in which $\vec{P}$ depends only on the history of $\vec{\mathcal{E}}$ at the same point in space.

When the applied fields are much smaller than the atomic fields seen by electrons in the medium, the polarization $\vec{P}(\vec{r},t)$ can be expanded into a power series in the applied electric field $\vec{\mathcal{E}}(\vec{r},t)$. Each term of this series has associated with it a response function tensor, $\overleftrightarrow{R}^{(n)}$, such that

$$P_i(\vec{r},t) = \sum_n P_i^{(n)}(\vec{r},t) \tag{2}$$

with

$$P_i^{(n)}(\vec{r},t) = \sum_{j_1} \cdots \sum_{j_n} \int_{-\infty}^{0} d\tau_1 \cdots \int_{-\infty}^{0} d\tau_n R^{(n)}_{i,j_1\ldots,j_n}(\tau_1\ldots,\tau_n)$$

$$\mathcal{E}_{j_1}(\vec{r},t+\tau_1)\ldots\mathcal{E}_{j_n}(\vec{r},t+\tau_n) \ . \tag{3}$$

Since the part of $\overleftrightarrow{R}^{(n)}$ that is antisymmetric in the exchange of any two of the pairs $(j_1,\tau_1)\ldots(j_n,\tau_n)$ does not contribute to $\vec{P}^{(n)}$, the tensor $\overleftrightarrow{R}^{(n)}$ can be rendered unique by requiring that it be invariant under all the permutations of the pairs $(j_1,\tau_1)\ldots(j_n,\tau_n)$;[76] this property is called the intrinsic permutation symmetry.

The dipole susceptibility tensors are simply the Fourier transforms of these dipole response tensors:

$$\overleftrightarrow{\phi}^{(n)}(\omega;\omega_1,\ldots,\omega_n) = \int_{-\infty}^{0} d\tau_1 \ldots \int_{-\infty}^{0} d\tau_n \, \overleftrightarrow{R}^{(n)}(\tau_1,\ldots,\tau_n)$$

$$\times \exp[-i(\omega_1\tau_1 + \ldots + \omega_n\tau_n)] \qquad (4)$$

Then, the Fourier transform of $\vec{P}^{(n)}(t)$ is given by:

$$\vec{P}^{(n)}(\omega) = \int d\omega_1 \ldots \int d\omega_n \, \delta(\omega-\omega_1-\ldots-\omega_n) \, \overleftrightarrow{\phi}^{(n)}(\omega;\omega_1,\ldots,\omega_n):$$

$$\vec{\mathcal{E}}(\omega_1)\ldots\vec{\mathcal{E}}(\omega_n) \qquad (5)$$

with

$$\vec{\mathcal{E}}(t) = \int \vec{\mathcal{E}}(\omega) \exp(-i\omega t) \, d\omega$$

and

$$\vec{P}(t) = \int \vec{P}(\omega) \exp(-i\omega t) \, d\omega \quad .$$

(The dependence of $\vec{\mathcal{E}}$ and $\vec{P}$ on $\vec{r}$ has been omitted to simplify the notation.) The tensor $\phi^{(n)}_{i,j_1,\ldots,j_n}(\omega;\omega_1,\ldots,\omega_n)$ is invariant under any permutation of the pairs (j_1,ω_1) ... (j_n,ω_n) due to the intrinsic permutation symmetry of $\overleftrightarrow{R}^{(n)}$, and it also obeys the additional permutation symmetry:[65,75]

$$\phi^{(n)}_{i,j_1,\ldots,j_n}(\omega;\omega_1,\ldots,\omega_n) = \phi^{(n)*}_{j_1,\ldots,j_n,i}(-\omega_1;\omega_2,\ldots,-\omega) \quad . \qquad (6)$$

Furthermore, since the fields $\vec{\mathcal{E}}(t)$ and $\vec{P}(t)$ are real valued, $\overleftrightarrow{\phi}^{(n)}$ satisfies the further symmetry relation

$$\overleftrightarrow{\phi}^{(n)}(\omega;\omega_1,\ldots,\omega_n)^* = \overleftrightarrow{\phi}^{(n)}(-\omega^*;-\omega_1^*,\ldots,-\omega_n^*) \quad . \tag{7}$$

Although Eq. (5) also describes the mixing of the Fourier components of a mode-locked or other broad bandwidth laser, the second order nonlinear optical frequency mixing processes are most simply discussed using monochromatic laser fields. For a single monochromatic laser with $\vec{\mathcal{E}}(\omega) = \vec{\mathcal{E}}_1\delta(\omega-\omega_1) + \vec{\mathcal{E}}_1^*\delta(\omega+\omega_1)$, only second harmonic generation (SHG) and optical rectification (OR) are caused by $\overleftrightarrow{\phi}^{(2)}$ and

$$\vec{P}(\omega) = \overleftrightarrow{\phi}^{(2)}(2\omega_1;\omega_1,\omega_1):\vec{\mathcal{E}}_1\vec{\mathcal{E}}_1\ \delta(\omega-2\omega_1)$$

$$+ 2\overleftrightarrow{\phi}^{(2)}(0;\omega_1,-\omega_1):\vec{\mathcal{E}}_1\vec{\mathcal{E}}_1^*\ \delta(\omega) \tag{8}$$

where from Eq. (8) on I shall omit those terms which are merely the negetive frequency counterparts of some explicitly displayed term. With two monochromatic laser beams, $\vec{P}^{(2)}$ becomes

$$\vec{P}^{(2)}(\omega) = 2\overleftrightarrow{\phi}^{(2)}(\omega_1-\omega_2;\omega_1,-\omega_2):\vec{\mathcal{E}}_1\vec{\mathcal{E}}_1^*\ \delta(\omega-\omega_1+\omega_2)$$

$$+ 2\overleftrightarrow{\phi}^{(2)}(\omega_1+\omega_2;\omega_1,\omega_2):\vec{\mathcal{E}}_1\vec{\mathcal{E}}_2\ \delta(\omega-\omega_1-\omega_2) \tag{9}$$

$$+ \text{SHG and OR terms.}$$

The linear electro-optic effect is described by the mixing of a laser field, $\vec{\mathcal{E}}_1$, with a DC field, $\vec{\mathcal{E}}_{dc}$, which can be obtained from Eq. (9) by setting ω_2 to zero and replacing $(\vec{\mathcal{E}}_2+\vec{\mathcal{E}}_2^*)$ with $\vec{\mathcal{E}}_{dc}$:

$$\vec{P}^{(2)}_{eo}(\omega) = 2\overleftrightarrow{\phi}^{(2)}(\omega_1;\omega_1,0):\vec{\mathcal{E}}_1\vec{\mathcal{E}}_{dc}\ \delta(\omega-\omega_1) \ . \tag{10}$$

The tabulated electro-optic coefficients, r_{ijk}, are expressed in-terms-of the induced change in the inverse of the linear dielectric tensor $\overleftrightarrow{\varepsilon}(\vec{\mathcal{E}}_{dc})$ so that in the principal axis coordinate system of a crystal:

$$\begin{aligned} r_{ijk} &= \frac{\partial}{\partial \mathcal{E}_{dc,k}} \left[\overleftrightarrow{\varepsilon}(\vec{\mathcal{E}}_{dc})\right]^{-1}_{ij} \\ &= \frac{\partial}{\partial \mathcal{E}_{dc,k}} \left[\overleftrightarrow{\varepsilon}(0) + 8\pi\overleftrightarrow{\phi}^{(2)}(\omega_1;\omega_1,0)\vec{\mathcal{E}}_{dc}\right]^{-1}_{ij} \\ &= -8\pi\varepsilon^{-1}_{ii}(0)\varepsilon^{-1}_{jj}(0)\overleftrightarrow{\phi}^{(2)}_{ijk}(\omega_1;\omega_1,0) \ . \end{aligned} \tag{11}$$

Throughout the remainder of this thesis, I shall use Bloembergen's notation for the susceptibility $\overleftrightarrow{\chi}^{(2)}$ for historical reasons and because it eliminates the miscellaneous factors of two in Eqs. (8), (9), and (10); in this notation

$$P_i(\omega) = \sum_{jk} \overleftrightarrow{\chi}^{(2)}_{ijk}(\omega;\omega_1,\omega_2):\mathcal{E}_j(\omega_1)\ \mathcal{E}_k(\omega_2)\ \delta(\omega-\omega_1-\omega_2) \tag{12}$$

and the peak electric field at $\omega_1 \neq 0$ is $2|\vec{\mathcal{E}}(\omega_i)|$. The relationship between the two notations and between them and the $\overleftrightarrow{d}$ tensor of Boyd and Kleinman[68] which is used in the SHG tabulations of the Landoelt-Boernstein series[79] are summarized below:

$$\overleftrightarrow{\chi}^{(2)}_{SHG} = 2\overleftrightarrow{d}^{(2)}_{SHG} = \overleftrightarrow{\phi}^{(2)}_{SHG} \tag{13a}$$

$$\overleftrightarrow{\chi}^{(2)}_{OR} = 4\overleftrightarrow{d}^{(2)}_{OR} = 2\overleftrightarrow{\phi}^{(2)}_{OR} \tag{13b}$$

$$\overleftrightarrow{\chi}^{(2)}_{eo} = \overleftrightarrow{d}^{(2)}_{eo} = 2\overleftrightarrow{\phi}^{(2)}_{eo} \tag{13c}$$

$$\overleftrightarrow{\chi}^{(2)}_{mix} = 2\overleftrightarrow{d}^{(2)}_{mix} = 2\overleftrightarrow{\phi}^{(2)}_{mix} \tag{13d}$$

When the optical frequencies are far from the electronic resonances of the material, Raman scattering from its simultaneously infrared and Raman active far-infrared elementary excitations is responsible for the dispersion of $\overleftrightarrow{\chi}^{(2)}$ for DFG. Although spin-flip transitions,[10] magnons, plasmons, etc. can also lead to dispersion of $\overleftrightarrow{\chi}^{(2)}$, TO phonons cause the dispersion of $\overleftrightarrow{\chi}^{(2)}$ in all of our experiments. In section IV of his review paper, Shen[71] has given a clear, concise derivation of the dispersion of $\overleftrightarrow{\chi}^{(2)}$ due to Raman scattering from polaritons associated with a TO phonon mode. He starts with Maxwell's equations for the high frequency pump (ω_1), low frequency pump or Raman Stokes (ω_2), and difference frequency ($\omega_3 \equiv \omega_1 - \omega_2$) electromagnetic fields, a damped simple harmonic oscillator (SHO) equation for the TO phonon mode, and nonlinear coupling terms that can be derived from the phenominological energy density:

$$\begin{aligned} \mathcal{F} = {} & \vec{Q}^*(\omega_3)\cdot\overleftrightarrow{f}:\vec{E}(\omega_1)\vec{E}^*(\omega_2) + \vec{E}^*(\omega_3)\cdot\overleftrightarrow{\chi}^{(2)}_{\infty}:\vec{E}(\omega_1)\vec{E}^*(\omega_2) \\ & + \vec{Q}^*(\omega_3)\cdot\overleftrightarrow{A}\cdot\vec{E}(\omega_3) + \text{c.c.} \quad . \end{aligned} \tag{14}$$

The nonlinear polarization at the three frequencies ω_i (i=1,2,3) and the force on the SHO are given by the equations $\vec{P}^{(2)}(\omega_i) = \partial F/\partial \vec{E}^*(\omega_i)$ and $\vec{F}(\omega_3) = \partial F/\partial \vec{Q}^*(\omega_3)$, respectively. Solving the SHO equation for $\vec{Q}(\omega_3)$ and eliminating $\vec{Q}(\omega_3)$ from the three Maxwell's equations. Shen obtains the Raman Stokes and difference frequency wave equations:

$$\{\vec{\nabla}x\vec{\nabla}x - (\omega_2/c)^2[\overleftrightarrow{\varepsilon}(\omega_2) + 4\pi\overleftrightarrow{\chi}_R^{(3)}:\vec{E}(\omega_1)\vec{E}^*(\omega_1)]\}\vec{E}(\omega_2)$$

$$= (4\pi\omega_2^2/c^2)\overleftrightarrow{\chi}^{(2)*}:\vec{E}(\omega_1)\vec{E}^*(\omega_3) \tag{15}$$

$$[\vec{\nabla}x\vec{\nabla}x - (\omega_3/c)^2\overleftrightarrow{\varepsilon}(\omega_3)]\vec{E}(\omega_3) = (4\pi\omega_3^2/c^2)\overleftrightarrow{\chi}^{(2)}:\vec{E}(\omega_1)\vec{E}^*(\omega_2) \tag{16}$$

where[80]

$$\overleftrightarrow{\varepsilon}(\omega_3) = \overleftrightarrow{\varepsilon}_\infty(\omega_3) + 4\pi\overleftrightarrow{A}^*\cdot\overleftrightarrow{A}/(\omega_0^2-\omega_3^2-i\omega_3\Gamma)$$

$$\overleftrightarrow{\chi}^{(2)} = \overleftrightarrow{\chi}_\infty^{(2)} + \overleftrightarrow{A}^*\cdot\overleftrightarrow{f}/(\omega_0^2-\omega_3^2-i\omega_3\Gamma)$$

$$\overleftrightarrow{\chi}_R^{(3)} = \overleftrightarrow{f}\cdot\overleftrightarrow{f}^*/(\omega_0^2-\omega_3^2+i\omega_3\Gamma) .$$

Fog fixed $\omega_1 \gg \omega_3$, the tensors $\overleftrightarrow{A}$, $\overleftrightarrow{f}$, $\overleftrightarrow{\varepsilon}_\infty$, and $\overleftrightarrow{\chi}_\infty^{(2)}$ are all nearly independent of ω_3 unless ω_1 is close to an electronic transition of the crystal. As can be seen from Eqs. (15) and (16), far-infrared reflection experiments determine $\overleftrightarrow{A}$ through $\overleftrightarrow{\varepsilon}(0)$ and $\overleftrightarrow{\varepsilon}_\infty$, and Raman scattering experiments measurements determine $\overleftrightarrow{f}$ through $\overleftrightarrow{\chi}_R^{(3)}$. The linear electro-optic coefficient determines $\overleftrightarrow{\chi}^{(2)}$ $(\omega_1-\omega_2;\omega_1,\omega_2)$ through Eqs. (11), (13c), and the permutation symmetry of $\overleftrightarrow{\chi}^{(2)}$; together with

$\overleftrightarrow{A}$ and $\overleftrightarrow{f}$ this determines $\overleftrightarrow{\chi}^{(2)}_{\infty}$ (If its dispersion can be neglected, $\overleftrightarrow{\chi}^{(2)}_{\infty}$ can also be determined from the results of SHG experiments.)

REFERENCES

1. L. C. Robinson, Physical Principles of Far-Infrared Radiation vol. 10 of Methods of Experimental Physics, L. Marton ed., (Academic Press, New York, 1973) pp. 10-81.

2. L. Genzel, "Far-Infrared Sources" in Far-Infrared Properties of Solids, S. S. Mitra and S. Nudelman eds., (Plenum, New York, 1970) pp. 52-56.

3. See, for example, P. D. Coleman, IEEE J. Quantum Electron. 9, 130 (1973).

4. See H. R. Fetterman and H. R. Schlossberg, IEEE Trans. Microwave Theory Tech. 22, 35 (1974) and references therein.

5. J. F. Butler, and A. R. Calawa, R. J. Phelan, A. J. Strauss, and R. H. Redicker, Solid State Commun. 2, 303 (1964).

6. J. M. Besson, J. F. Butler, A. R. Calawa, W. Paul, and R. H. Redicker, Appl. Phys. Lett. 7, 206 (1965); J. M. Besson, W. Paul, and A. R. Calawa, Phys. Rev. 173, 699 (1968).

7. E. D. Hinkley and P. L. Kelley, Science 171, 635 (1971); J. F. Butler and T. C. Harman, Appl. Phys. Lett. 12, 347 (1968).

8. J. M. Yarborough, S. S. Sussman, H. E. Puthoff, R. H. Pantel, and B. C. Johnson, Appl. Phys. Lett. 15, 102 (1969); B. C. Johnson, H. E. Puthoff, J. Soo Hoo, and S. S. Sussman, Appl. Phys. Lett. 18, 181 (1971).

9. E. D. Shaw, Appl. Phys. Lett. 29, 28 (1976).

10. Y. R. Shen, Appl. Phys. Lett. 23, 516 (1973).

11. L. C. Robinson, Op. Cit. p. 28.

12. L. R. Elias, W. M. Fairbank, J. M. J. Madey, H. A. Schwettman, and T. I. Smith, Phys. Rev. Lett. 36, 717 (1976).

13. See, for example, J. M. J. Madey, J. Appl. Phys. 42, 1906 (1971) or F. A. Hopf, P. Meystre, M. O. Scully, and W. H. Louisell, Phys. Rev. Lett. 37, 1215 (1976); 37, 1342 (1976).

14. F. Zernike, Jr. and P. R. Berman, Phys. Rev. Lett. 15, 999 (1965).

15. T. Yajima and N. Takeuchi, Jap. J. Appl. Phys. 9, 1361 (1970).

16. T. Yajima and N. Takeuchi, Jap. J. Appl. Phys. 10, 907 (1971).

17. K. H. Yang, P. L. Richards, and Y. R. Shen, Appl. Phys. Lett. 19, 320 (1971).

18. N. Takeuchi, N. Matsumoto, T. Yajima, and S. Kishida, Jap. J. Appl. Phys. 11, 268 (1972).

19. N. Matsumoto and T. Yajima, Jap. J. Appl. Phys. 12, 90 (1973).

20. F. Zernike, Bull. Am. Phys. Soc. 12, 687 (1967).

21. F. Zernike, Phys. Rev. Lett. 22, 931 (1969).

22. V. T. Nguyen and C. K. N. Patel, Phys. Rev. Lett. 22, 463 (1969).

23. C. K. N. Patel and V. T. Nguyen, Appl. Phys. Lett. 15, 189 (1969).

24. V. T. Nguyen, A. R. Strand, A. M. Jean-Louis, and G. Duraffourg, in The Physics of Semimetals and Narrow Gap Semiconductors, D. L. Carter and R. T. Bates, eds., (Pergamon, New York, 1971) p. 231.

25. V. T. Nguyen and T. J. Bridges, Phys. Rev. Lett. 29, 359 (1972).

26. T. Y. Chang, V. T. Nguyen, and C. K. N. Patel, Appl. Phys. Lett. 13, 357 (1968).

27. T. J. Bridges and T. Y. Chang, Phys. Rev. Lett. 22, 811 (1969).

28. T. J. Bridges and A. R. Strnad, Appl. Phys. Lett. 20, 382 (1972).

29. D. E. Thompson and P. D. Coleman, in International Conference on Submillimeter Waves and their Applications, Atlanta, 1974, Conference Digest, pp. 24-25.

30. D. E. Thompson and P. D. Coleman, IEEE Trans. Microwave Theory Tech. 22, 995 (1974).

31. D. E. Thompson, Ph.D. dissertation, 1974, University of Illinois, (unpublished).

32. V. I. Bogatkin, G. D. Lobov, and V. V. Shtykov, Sov. J. Quantum Electron. 3, 447 (1974).

33. A. A. Vedenov, G. D. Mylinkov, V. A. Roslyakov, D. N. Sobolenko, and A. N. Starostin, Phys. Lett. A 50, 79 (1974).

34. R. L. Aggarwal, B. Lax, and G. Favrot, Appl. Phys. Lett. 22, 329 (1973).

35. B. Lax, R. L. Aggarwal, and G. Favrot, Appl. Phys. Lett. 23, 679 (1973).

36. R. L. Aggarwal, N. Lee, and B. Lax, in International Conference on Submillimeter Waves and their Applications, Atlanta, 1974, Conference Digest, pp. 19-20.

37. B. Lax and R. L. Aggarwal in Laser Spectroscopy, R. G. Brewer and A. Mooradian, eds., (Plenum, New York, 1974), pp. 504-512.

38. B. Lax and R. L. Aggarwal, J. Opt. Soc. Am. 64, 533 (1974).

39. N. Lee, R. L. Aggarwal, and B. Lax, Opt. Commun. 11, 339 (1974).

40. B. Lax and R. L. Aggarwal, Microwave J. 17, 31 (1974).

41. R. L. Aggarwal, B. Lax, H. R. Fetterman, P. E. Tannenwald, and B. J. Clifton, J. Appl. Phys. 45, 3972 (1974).

42. N. Lee, B. Lax, and R. L. Aggarwal, Opt. Commun. 18, 50 (1976).

43. G. D. Boyd, T. J. Bridges, C. K. N. Patel, and E. Buehler, Appl. Phys. Lett. 21, 553 (1972).

44. T. J. Bridges and V. T. Nguyen, Appl. Phys. Lett. 23, 107 (1973).

45. V. T. Nguyen and T. J. Bridges, in International Conference on Submillimeter Waves and their Applications, Atlanta, 1974, Conference Digest, p. 41.

46. V. T. Nguyen and T. J. Bridges, in Laser Spectroscopy, R. G. Brewer and A. Mooradian, eds., (Plenum, New York, 1974) pp. 513-521.

47. T. J. Bridges and V. T. Nguyen, J. Opt. Soc. Am. 64, 532 (1974).

48. V. T. Nguyen and T. J. Bridges, Appl. Phys. Lett. 26, 452 (1975).

49. T. J. Brignall, R. A. Wood, C. R. Pidgeon, and B. S. Wherrett, Opt. Commun. 12, 17 (1974).

50. T. Yajima and K. Inoue, Phys. Lett. A 26, 281 (1968).

51. T. Yajima and K. Inoue, IEEE J. Quantum Electron. 4, 319 (1968).

52. T. Yajima and K. Inoue, IEEE J. Quantum Electron. 5, 140 (1969).

53. D. W. Faries, K. A. Gehring, P. L. Richards, and Y. R. Shen, Phys. Rev. 180, 363 (1969).

54. D. Faries, Ph.D. dissertation, 1969, Phys. Dept. University of California, Berkeley, (unpublished).

55. D. W. Faries, P. L. Richards, Y. R. Shen, and K. H. Yang, Phys. Rev. A 3, 2148 (1971).

56. N. Paraire, A. Koster, S. Biraud-Laval, and R. Reinisch, Phys. Status Solidi B 68, 543 (1975).

57. A. Koster and A. Vossougi, J. Phys. E 9, 340 (1976).

58. F. De Martini, Phys. Lett A 30, 319 (1969).

59. F. De Martini, Phys. Lett. A 30, 547 (1969).

60. F. De Martini, Phys. Rev. B 4, 4556 (1971).

61. K. H. Yang, J. R. Morris, P. L. Richards, and Y. R. Shen, Bull. Am. Phys. Soc. series 2, 18, 350 (1973).

62. K. H. Yang, J. R. Morris, P. L. Richards, and Y. R. Shen, Appl. Phys. Lett. 23, 669 (1973).

63. K. H. Yang, Ph.D. dissertation 1974, Physics Dept. University of California, Berkeley (unpublished).

64. D. H. Auston, A. M. Glass, and P. Le Fur, Appl. Phys. Lett. 23, 47 (1973).

65. J. A. Armstrong, N. Bloembergen, J. Ducuing, and P. S. Pershan, Phys. Rev. 127, 1918 (1962).

66. See, for example, N. Bloembergen, Nonlinear Optics, (Benjamin, New York, 1965).

67. T. L. Brown and P. A. Wolff, Phys. Rev. Lett. 29, 362 (1972).

68. See, for example, G. D. Boyd and D. A. Kleinman, J. Appl. Phys. 39, 3597 (1968).

69. U. A. Abdullin, G. A. Lyakhov, O. V. Rudenko, and A. S. Chirkin, Sov. Phys.-JETP 39, 633 (1974).

70. J. R. Morris and Y. R. Shen, Opt. Commun. 3, 81 (1971).

71. Y. R. Shen, Prog. Quantum Electron 4, 207 (1976).

72. J. Warner, "Difference Frequency Generation and Up Conversion" in Quantum Electronics: A Treatise, vol. Ib, H. Rabin and C. L. Tang eds., (Academic Press, New York, 1975) pp. 703-737.

73. J. R. Morris and Y. R. Shen, Phys. Rev. A 15, 1143 (1977).

74. R. G. Smith, "Optical Parametric Oscillators" in Laser Handbook, vol. 1, F. T. Arecchi and E. O. Schultz-DuBois eds., (North-Holland, Amsterdam, 1972) p. 868.

75. Y. R. Shen, Phys. Rev. 167, 818 (1968).

76. C. Flyzanis, "Theory of Nonlinear Optical Susceptibilities," in Quantum Electronics: A Treatise, vol. Ia, H. Rabin and C. L. Tang eds., (Academic Press, New York, 1975) pp. 9-207.

77. P. N. Butcher, Nonlinear Optical Phenomena, Ohio State Univ. Eng. Publ.

78. J. D. Jackson, Classical Electrodynamics, (John Wiley and Sons, New York, 1972), p. 194ff.

79. Landoelt-Boernstein New Series, K. H. Hellwege ed., III/2, (Springer-Verlag, Berlin, 1969), p. 167ff.

80. In the definitions of $\overleftrightarrow{\varepsilon}(\omega_3)$, $\overleftrightarrow{\chi}^{(2)}$, and $\overleftrightarrow{\chi}_R^{(3)}$, the "$\cdot$" means sum over the index that corresponds to $\vec{Q}^*$. Also, the index of $\overleftrightarrow{\chi}_R^{(3)}$ which is not summed over in Eq. (15) is the index of the first $\overleftrightarrow{f}$ that corresponds to $\vec{E}^*(\omega_2)$.

CHAPTER II. THEORY OF FAR-INFRARED GENERATION BY DIFFERENCE FREQUENCY MIXING OF MONOCHROMATIC LASER BEAMS

I. Introduction

Far-infrared generation by optical mixing has recently received increasing attention.[1] It has the potential of providing a coherent tunable far-infrared source which compliments far-infrared molecular lasers. The most commonly used scheme is that of difference-frequency generation (DFG) by mixing of two laser beams in a non-centrosymmetric crystal. With dye lasers,[2-3] CO_2 lasers,[4-16] or spin-flip Raman lasers[17-20] as the pump beams, DFG can provide a far-infrared source discretely or continuously tunable from 1 cm^{-1} to 200 cm^{-1} or more. The output linewidth can easily be less than 0.1 cm^{-1} as determined by the pump laser linewidths. In most cases, the output is in pulses with pulsewidths between 10 nsec and 10 μsec, but CW operation has recently been achieved.

A serious limitation of far-infrared generation by optical mixing has been the attainable average power, although so far as spectral power per unit solid angle is concerned it is already better than a blackbody source at 5000°K.[1] While focusing of the pump beams may increase the far-infrared output, it is not clear how tight the focusing can be before the detrimental effect of far-infrared diffraction sets in. No adequate theoretical calculation of nonlinear far-infrared generation with focusing and diffraction properly taken into account has been reported. Experimentally, on the other hand, a tight focusing geometry has so far been avoided. As a result, the full potential of

nonlinear far infrared generation has not been assessed.

In the literature, the plane-wave theory was often used to interprete the results of far-infrared generation experiments.[2,6,7,11,12,21-25] The theory assumes a single spatial Fourier component for each monochromatic wave so that the nonlinear process is characterized by a single phase matching relation. However, when the pump beams are focused to a spot comparable in size to the far-infrared wavelength, far-infrared diffraction is important and the spatial Fourier components of the output extend over a large cone. Each Fourier component now has its own phase matching relation with respect to the pump beams. Since it is not possible to phase match all the Fourier components simultaneously, focusing of the pump beams does not improve the far-infrared output power as much as the plane-wave theory predicts.

The plane-wave theory also assumes a single transmission coefficient for the far-infrared output across the boundary surface. Actually, with the far-infrared output extending over a large cone, the transmission coefficient is different for each Fourier component and falls to zero at the total reflection angle. Thus, the real output can be considerably less than what the plane wave theory predicts. Finally, the plane wave theory often ignores the reduction in output power due to double refraction which can be significant for small spot sizes in crystalline media.

Improvement in the calculations of far-infrared generation by optical mixing has been achieved by Faries et al.[26] using the far-field diffraction theory for a distribution of oscillating dipoles induced

by the pump beams.[26-28] They used an average transmission coefficient for the far-infrared output across the boundary and excluded the contribution from the totally reflected modes. The effect of double refraction was, however, ignored. As we shall see later, in the absence of double refraction, this approach in fact gives a remarkably good estimate of the far-infrared output.

In this paper, we present a more rigorous calculation of far-infrared generation by optical mixing. It proceeds by first calculating separately each Fourier component of the output field and then evaluating the output power by summing over the Fourier components. The effects of focusing, absorption, phase matching, and double refraction can all be properly taken into account. For the sake of simplicity, the pump beams are assumed to be of single mode with Gaussian profiles. Our approach is essentially the same as that used by Bjorkholm[29] and by Kleinman et al.[30] for second-harmonic generation by focused beams.

The main difference between second-harmonic (or sum-frequency) generation in the visible or near infrared and difference-frequency generation in the far-infrared is diffraction. Validity of the scalar Fresnel approximation for the pump beams guarantees its validity for the sum frequency but not for the difference frequency. Because of its much longer wavelength and hence stronger diffraction, the far-infrared output extends over a much broader cone. Thus, the phase matching condition varies much more appreciably among the output Fourier components in difference-frequency generation (DFG) than in

sum-frequency generation (SFG). All the Fourier components can often be nearly simultaneously phase matched for SFG but not for DFG. An accurate description of DFG also requires knowledge of the difference-frequency transmission coefficients over a very broad output cone.

The body of the paper is organized into the following sections: Section II describes the theory of DFG by monochromatic Gaussian laser beams which is valid even when the pump focal spot size is smaller than a far-infrared wavelength. This theory is developed from a generalization of the non-linear polarization used by Boyd and Kleinman[31] and by Faries.[28] Section III contains the results of numerical calculations obtained from this theory. First, we present the results for the ideal case of no double refraction. Then, we discuss briefly the reductions in attainable power due to far-infrared absorption and double refraction. Finally, in Section IV, we compare our results with the results of three other calculations: a simple plane wave calculation, a far-field diffraction calculation assuming a constant 1/e radius Gaussian distribution of induced dipoles, and the second harmonic generation calculations of Boyd and Kleinman.[31]

II. Theory

A. Nonlinear Polarization

We assume that the pump beams are monochromatic with Gaussian TEM_{oo} mode. If focusing and diffraction of the pump beams are not too strong, the focused pump fields in a slab medium can be written as[28,31]

$$\vec{E}_i(\vec{r},t) = \frac{\vec{\mathcal{E}}_i}{1+i\xi_i} \exp\left[-\frac{(x-a_i-\zeta_i z)^2+y^2}{w_i^2(1+i\xi_i)} + ik_i z - \omega_i t\right] \qquad (17)$$

for $0 \leqslant z \leqslant \ell$, where the subindex i denotes the i-th beam; w_i is the e^{-2} beam radius in the focal plane which is located at $z = z_{0i}$; the beam axis intersects the front surface of the medium at $x = a_i$ and $y = 0$; the quantity ξ_i is defined by $\xi_i = 2(z-z_{0i})/k_i w_i^2$ with $k_i = \omega_i n_i/c$, n_i being the refractive index; finally, ζ_i is the walk-off angle given by $\zeta_i = \frac{1}{2}\sin(2\theta_i)\ n_i^2(n_{em,i}^{-2}-n_{o,i}^{-2})$ if the beam is an extraordinary ray propagating in a uniaxial medium along a direction at an angle θ with respect to the optical axis where $n_{o,i}$ and $n_{em,i}$ are respectively the ordinary and extra-ordinary refractive indices at $\theta = 90°$. The derivation of Eq. (17) involves some approximations which can easily be justified as shown in Appendix A. In the following, to simplify the calculations in practical cases, we can assume that the largely overlapping pump beams are focused to the same spot size at the same point with $w_i \equiv w$, $\xi_i \equiv \xi$ and $z_{0i} \equiv z_o$. This is a good approximation when the refractive indices of the pump beams are not very different, as is true in all practical cases which have been investigated.

The pump fields now induce a nonlinear polarization at the far-infrared frequency in the medium. We consider here only the case of DFG in a uniaxial crystal as an example although the formalism can be easily extended to more general cases of optical mixing. The nonlinear polarization at the difference frequency ω is then given by

$$\vec{P}^{(2)}(\vec{r},\omega) = \overleftrightarrow{\chi}^{(2)}(\omega = \omega_1 - \omega_2): \vec{E}_1(\vec{r},\omega_1)\vec{E}_2^*(\vec{r},\omega_2) \tag{18}$$

where $\overleftrightarrow{\chi}^{(2)}$ is the second-order nonlinear susceptibility tensor. We assume that $\vec{E}_1$ is an ordinary ray and $\vec{E}_2$ is extraordinary. The nonlinear polarization $\vec{P}^{(2)}(\vec{r})$ dan be readily found by substituting the expression of $\vec{E}_i$ of Eq. (17) into Eq. (18). For convenience of solving the wave equation later, we are however interested in the transverse Fourier components of $\vec{P}^{(2)}(\vec{r})$. The transverse Fourier transform gives

$$\vec{P}^{(2)}(\vec{k}_T,z) = \frac{1}{2\pi}\int_{-\infty}^{\infty} dxdy\ \vec{P}^{(2)}(\vec{r})\ \exp(-ik_x x - ik_y y)$$

$$= \overleftrightarrow{\chi}^{(2)}: \hat{\varepsilon}_1\hat{\varepsilon}_2^*\ \frac{1}{4}w^2\ \exp\{i[(k_1-k_2^*)z - k_x(a_i-\zeta z)/2]\}$$

$$\times\ \exp\left[-\frac{(a_1-\zeta z)^2}{2w^2} - \frac{1}{8}k_T^2 w^2(1+\xi^2) - \frac{1}{2}k_x(a_1-\zeta z)\xi\right] \tag{19}$$

where $\vec{k}_T = \hat{x}k_x + \hat{y}k_y$ and we set $a_2 = 0$. For economy of notation, we omit explicit mention of the argument ω.

B. Solution of Wave Equations

Far-infrared generation by optical mixing is described by the set of wave equations

$$[\nabla \times (\nabla x) - (\omega^2/c^2)\overleftrightarrow{\varepsilon}]\vec{E}(\vec{r},\omega) = 4\pi(\omega^2/c^2)\vec{P}^{NL}(\vec{r},\omega) \tag{20a}$$

$$\nabla \cdot [\overleftrightarrow{\varepsilon}\cdot\vec{E}(\vec{r},\omega)] = -4\pi\nabla \cdot \vec{P}^{NL}(\vec{r},\omega) \tag{20b}$$

where the nonlinear polarization P^{NL} acts as a driving source for the nonlinear process. For DFG in a uniaxial medium $P^{NL} = P^{(2)}$ given by Eq. (18). Since the normal to slab boundary planes is $\hat{z}$, the easiest method is to Fourier transform the x and y variables in Eq. (20) and to solve for each Fourier component $\vec{E}(\vec{k}_T, z)$ separately.[32] The corresponding source term for $\vec{E}(\vec{k}_T, z)$ is $4\pi(\omega^2/c^2)\ \vec{P}^{(2)}(\vec{k}_T, z)$ with $\vec{P}^{(2)}(\vec{k}_T, z)$ given by Eq. (19).

The general solution for $\vec{E}(\vec{k}_T, z)$ consists of two parts, the homogeneous solution and the particular solution respectively. The homogeneous solution is well known. For ordinary and extraordinary polarizations respectively, it can be written as

$$\vec{E}^h_{o\pm}(\vec{k}_T, z) = \mathcal{E}_{o\pm}\hat{o}_\pm \exp\ (ik_{o\pm,z} \cdot z)$$

$$\vec{E}^h_{e\pm}(\vec{k}_T, z) = \mathcal{E}_{e\pm}\ \hat{e}_\pm \exp\ (ik_{e\pm,z} \cdot z) \qquad (21)$$

where the subindices + and - denote forward and backward propagating waves respectively with the same $\vec{k}_T$, and $k_{o\pm,z} = \pm[\ \omega n_o/c)^2 - k_T^{\ 2}]^{1/2}$ with a similar expression for $k_{e\pm,z}$. To find the particular solution, let us first assume that the nonlinear slab is imbedded in a linear medium with an equal linear dielectric constant. Thus, reflection and refraction at the crystal boundaries can be ignored. The boundary effects will be taken into account later. As shown in Appendix B, the particular solution for $E(\vec{k}_T, z)$ is then given by

$$\vec{E}^{p}(\vec{k}_T,z) = E^{p}_{o+}(\vec{k}_T,z)\ \hat{o}_+ + E^{p}_{o-}(\vec{k}_T,z)\ \hat{o}_- + E^{p}_{e+}(\vec{k}_T,z)\ \hat{e}_+$$

$$+ E^{p}_{e-}(\vec{k}_T,z)\ \hat{e}_- - (4\pi n_e^2/n_o^2 n_{em}^2)\ \hat{z}\ P_z^{(2)}\ (\vec{k}_T,z) \tag{22}$$

where n_{em} is the refractive index for extraordinary ray propagating perpendicular to the optical axis,

$$E^{p}_{o-}\ (\vec{k}_T,z) = \frac{2\pi i\omega^2}{c^2 k_{oz}} \int_o^z \hat{o}_+ \cdot \vec{P}^{(2)}(\vec{k}_T,z')e^{ik_{oz}(z-z')}\,dz'$$

$$E^{p}_{o-}\ (\vec{k}_T,z) = \frac{2\pi i\omega^2}{c^2 k_{oz}} \int_z^{\ell} \hat{o}\ \cdot \vec{P}^{(2)}(\vec{k}_T,z')e^{-ik_{oz}(z-z')}dz'$$

$$E^{p}_{e+}(\vec{k}_T,z) = \frac{2\pi i\omega^2}{c^2 (k_{ez})_{eff}} \int_o^z \hat{e}_+ \cdot \vec{P}^{(2)}(\vec{k}_T,z')e^{ik_{e+,z}(z-z')}\,dz'$$

$$E^{p}_{e-}(\vec{k}_T,z) = \frac{2\pi i\omega^2}{c^2 (k_{ez})_{eff}} \int_z^{\ell} \hat{e}_- \cdot \vec{P}^{(2)}(\vec{k}_T,z')e^{ik_{e-,z}(z-z')}\,dz'$$

$$(k_{ez})_{eff,\pm} = (k_{e+,z} - k_{e-,z})n_{em}^2 \Big/ \left\{ 2n_e^2 \left[1 - \left(\frac{n_o^2 - n_{em}^2}{n_o^2} \right) \frac{(\hat{c}\cdot\vec{k}_{e+})^2}{k_o^2} \right] \right\} \tag{23}$$

$\hat{c}$ is the optical axis of the crystal. The last term in Eq. (22) is a longitudinal field which leads to optical rectification[33] when $\omega = \omega_1 - \omega_2 = 0$. It is, however, a non-radiating term and we shall neglect it in the following discussion.

The solution in Eqs. (22) and (23) appear in the form normally obtained for nonlinear optical processes in the slowly varying envelope approximation. However, no such approximation has been made. As shown in Appendix B, Eq. (22) together with Eq. (23) is an exact solution of Eq. (20) with $\vec{P}^{(2)}(\vec{k}_T,z)$ as the source term. The field $\vec{E}^p(\vec{k}_T,z)$ in the medium does not have a slowly varying amplitude since $\partial^2|\vec{E}^p(\vec{k}_T,z)|/\partial z^2$ is not negligible in comparison with $2k\partial|\vec{E}^p(\vec{k}_T,z)|/\partial z$. In fact, the slowly varying envelope approximation is equivalent to assuming for each polarization a wave propagating in one direction only.

As a check, we can use Eqs. (22) and (23) to derive the solution for the special case of optical mixing at an infinite boundary surface discussed by Bloembergen.[34] We have $k_y = 0$, $\ell \to \infty$, and $\vec{P}^{(2)}(\vec{k}_T,z) = P_0\hat{y}e^{ik_{sz}z}$ in the medium. Equation (23) gives for the reflected output

$$\vec{E}^p_r = -\frac{2\pi\omega^2}{c^2k_{oz}(k_{oz}+k_{sz})}\hat{y}P_0e^{-ik_{oz}z} \quad \text{for} \quad z<0 \tag{24a}$$

and for the transmitted output

$$\vec{E}^p_t = \frac{2\pi\omega^2}{c^2k_{oz}}\hat{y}P_0\left[\frac{2k_{oz}}{k_s^2-k_o^2}e^{ik_{sz}z} - \frac{1}{k_{sz}-k_{oz}}e^{ik_{oz}z}\right] \quad \text{for } z>0 \tag{24b}$$

The above solution is, however, only true for the case with no reflection at the boundary, but the boundary effects can be easily incorporated by taking into account the linear reflection of $\vec{E}^p_r$ at the boundary surface. The complete solution for the problem with a crystal-vacuum plane boundary is then given by

$$\vec{E}_R^p = \frac{2k_{oz}}{k_{oz}+k_z}\,\vec{E}_r^p(z=0)\,e^{-ik_z z} \qquad \text{for} \quad z<0$$

$$\vec{E}_T^p = \vec{E}_t^p - \frac{k_z-k_{oz}}{k_z+k_{pz}}\,\vec{E}_r^p(z=0)\,e^{ik_o z} \qquad \text{for} \quad z>0 \tag{25}$$

where $k_z = [(\omega/c)^2 - k_x^2]^{1/2}$. Substitution of the expressions for $\vec{E}_r^p$ and $\vec{E}_t^p$ in Eq. (24) into Eq. (25) yields results identical to those derived by Bloembergen.[34]

The above example suggests that the boundary effects can indeed be taken care of separately. In Sec. IIC, we shall use the same procedure to take into account the boundary conditions of optical mixing in a slab medium. Then, with the expression of $\vec{P}^{(2)}(\vec{k}_T,z)$ in Eq. (19), we can calculate from Eqs. (21) - (23) and the appropriate boundary conditions the Fourier component $\vec{E}(\vec{k}_T,z)$ of the DFG output and hence the difference-frequency field $\vec{E}(\vec{r})$ in space. In many cases, only one of the four waves in Eq. (23) is nearly phase-matched. When this happens, we need to retain only the phase-matched component in a good approximate calculation.

C. Boundary Effects

We have seen in Sec. IIB how we can take into account the boundary effects of a crystal-vacuum interface by simply incorporating linear reflection and transmission of the waves at the boundary into the solution. We now discuss the boundary effects of the more general case of a slab crystalline medium. We can consider $\vec{E}_+^p$ in Eq. (22) as forward propagating waves starting from z = 0 in the medium and

subsequently undergoing multiple partial reflections at the two slab surfaces. Similarly, we consider $\vec{E}^{p}_{-}$ in Eq. (22) as backward propagating waves starting from $z = \ell$ in the medium. Thus, the field outside the slab is given by the sum of $\vec{E}^{p}_{+}$ and $\vec{E}^{p}_{-}$ weighted respectively by appropriate Fabry-Perot factors due to multiple reflections and transmissions. To find the Fabry-Perot factors, we first calculate the transmission and reflection matrices for ordinary and extraordinary waves at a single crystal-vacuum boundary surface, and then find the overall transmission and reflection matrices of the slab for the two waves by summing over multiple transmissions and reflections at the slab surfaces.

Consider first the case defined in Fig. 1a. The incident monochromatic plane wave $\vec{E}_{i+}(\vec{k}_T) = E^{\parallel}_{i+}\,\hat{\parallel}_{+} + E^{\perp}_{i+}\hat{\perp}$ and the reflected plane wave $\vec{E}_{r-}(\vec{k}_T) = E^{\parallel}_{r-}\,\hat{\parallel}_{-} + E^{\perp}_{r-}\hat{\perp}$ are related to the refracted ordinary and extraordinary waves $\vec{E}_{o+}(\vec{k}_T)$ and $\vec{E}_{e+}(\vec{k}_T)$ respectively, by the matrix relations[35]

$$\begin{pmatrix} E^{\perp}_{i+} \\ E^{\parallel}_{i+} \end{pmatrix} = \overleftrightarrow{A}_{+} \begin{pmatrix} E_{o+} \\ E_{e+} \end{pmatrix}$$

$$\begin{pmatrix} E^{\perp}_{r-} \\ E^{\parallel}_{r-} \end{pmatrix} = \overleftrightarrow{B}_{+} \begin{pmatrix} E_{o+} \\ E_{e+} \end{pmatrix} \qquad (26)$$

where

$$\overleftrightarrow{A}_{\pm} \equiv \begin{pmatrix} \alpha_o^{\pm}/(1+r_o^{\perp}), & \alpha_e^{\pm}/(1+r_{e\pm}^{\perp}) \\ \beta_o^{\pm}\, k_o/(1+r_o^{\parallel})k, & \beta_e^{\pm}\, k_e/(1+r_{e\pm}^{\parallel})k \end{pmatrix}$$

$$\overleftrightarrow{B}_{\pm} \equiv \begin{pmatrix} \alpha_o^{\pm}\, r_0^{\perp}/(1+r_o^{\perp}), & \alpha_e^{\pm} r_{e\pm}^{\perp}/(1+r_{e\pm}^{\perp}) \\ \beta_o^{\pm} r_o^{\parallel} k_o/(1+r_o^{\parallel})k, & \beta_e^{\pm} r_{e\pm}^{\parallel} k_e/(1+r_{e\pm}^{\parallel})k \end{pmatrix}$$

$$r_o^{\perp} \equiv (k_z - k_{oz})/(k_z + k_{oz}),\ r_o^{\parallel} \equiv (k_o^2 k_z - k^2 k_{oz})/(k_o^2 k_z + k^2 k_{oz}) ,$$

$$r_{e\pm}^{\perp} \equiv (-k_{ez}^{\pm} \pm k_z)/(k_{ez}^{\pm} \pm k_z),\ r_{e\pm}^{\parallel} \equiv (-k^2\gamma_e^{\pm} \pm k_z k_e^{\pm}\beta_e^{\pm})/(k^2\gamma_e^{\pm} \pm k_z k_e^{\pm}\beta_e^{\pm})$$

$$\alpha_o^{\pm} \equiv \hat{o}_{\pm} \cdot (\hat{z} \times \hat{k}_T), \qquad \beta_o^{\pm} \equiv \hat{o}_{\pm} \cdot \left[(\hat{z} \times \hat{k}_T) \times \hat{k}_o^{\pm}\right]$$

$$\alpha_e^{\pm} \equiv \hat{e}_{\pm} \cdot (\hat{z} \times \hat{k}_T), \qquad \beta_e^{\pm} \equiv \hat{e}_{\pm} \cdot \left[(\hat{z} \times \hat{k}_T) \times \hat{k}_e^{\pm}\right]$$

$$\gamma_e^{\pm} \equiv \hat{e}_{\pm} \cdot \hat{k}_T .$$

With subindex "-" applied to the case of Fig. 1b with

$$\begin{pmatrix} E_{i-}^{\perp} \\ E_{i-}^{\parallel} \end{pmatrix} = \overleftrightarrow{A}_- \begin{pmatrix} E_{o-} \\ E_{e-} \end{pmatrix} , \qquad \begin{pmatrix} E_{r+}^{\perp} \\ E_{r+}^{\parallel} \end{pmatrix} = \overleftrightarrow{B}_- \begin{pmatrix} E_{o-} \\ E_{e-} \end{pmatrix}$$

We next consider transmission and reflection of ordinary and extraordinary waves incident from the crystal side onto the boundary surface as described by Diagram a in Fig. 2. Clearly, Diagram a is equivalent

to the sum of Diagram b and Diagram c, and Diagrams b and c are identical to those in Fig. 1a and Fig. 1c respectively. We therefore have

$$\vec{E}_{t-} = \vec{E}'_{t-} + \vec{E}''_{t-} = \overleftrightarrow{T}_- \begin{pmatrix} E_{o-} \\ E_{e-} \end{pmatrix}$$

$$\begin{pmatrix} E_{o+} \\ E_{e+} \end{pmatrix} = \overleftrightarrow{R}_- \begin{pmatrix} E_{o-} \\ E_{e-} \end{pmatrix} \tag{27}$$

where

$$\overleftrightarrow{T}_\pm = \overleftrightarrow{A}_\pm - \overleftrightarrow{B}_\mp \overleftrightarrow{A}_\mp^{-1} \overleftrightarrow{B}_\pm$$

$$\overleftrightarrow{R}_\pm = - \overleftrightarrow{A}_\mp^{-1} \overleftrightarrow{B}_\pm \ ;$$

the subindices "+" and "-" now refer to cases where the crystalline medium occupy the left half-space and the right half-space, respectively.

We can now use the results in Eq. (27) to calculate the effect of multiple transmissions and reflections at the boundaries of a crystal slab. In particular, we are interested in finding the forward and backward propagating far-infrared waves outside the slab created by optical mixing inside the slab. As we mentioned earlier, we can imagine that optical mixing generates waves $\vec{E}^p_+$ starting at $z = 0$ and $\vec{E}^p_-$ starting at $z = \ell$ and in getting out of the slab, these waves undergo multiple transmissions and reflections. Therefore, for the generated field outside the slab, we readily find for $z = \ell$

$$\vec{E}_{T+} = \overleftrightarrow{T}_+ \overleftrightarrow{F}_+ \left[\begin{pmatrix} E_{o+}(\ell) \\ \\ E_{e+}(\ell) \end{pmatrix} + \overleftrightarrow{P}_+ \overleftrightarrow{R}_- \begin{pmatrix} E_{o-}(o) \\ \\ E_{e-}(o) \end{pmatrix} \right] \tag{28a}$$

and for $z < 0$

$$\vec{E}_{T-} = \overleftrightarrow{T}_- \overleftrightarrow{F}_- \left[\begin{pmatrix} E_{o-}(o) \\ \\ E_{e-}(o) \end{pmatrix} + \overleftrightarrow{P}_- \overleftrightarrow{R}_+ \begin{pmatrix} E_{o+}(\ell) \\ \\ E_{e+}(\ell) \end{pmatrix} \right] \tag{28b}$$

where

$$\overleftrightarrow{P}_\pm = \begin{pmatrix} \exp(ik_{oz}\ell) & \\ & \exp(\pm ik_{ez}^{\pm}) \end{pmatrix}$$

and

$$\overleftrightarrow{F}_\pm = [\overleftrightarrow{1} - \overleftrightarrow{P}_\pm \overleftrightarrow{R}_\mp \overleftrightarrow{P}_\mp \overleftrightarrow{R}_\pm]^{-1} = \sum_{n=0}^{\infty} [\overleftrightarrow{P}_\pm \overleftrightarrow{R}_\mp \overleftrightarrow{P}_\mp \overleftrightarrow{R}_\pm]^n \tag{29}$$

Because of the generalized Fabry-Perot factor $\overleftrightarrow{F}_\pm$, the output fields $\vec{E}_{T\pm}$ can be rapidly varying functions of $\vec{k}_T$, ω, and ℓ. In some cases, however, when the pump laser beams have fairly bread linewidths or the crystal slab is wedged or not sufficiently well polished, it is more appropriate to find an average Fabry-Perot factor or the average output by averaging over one Fabry-Perot period. For example, in the nearly isotropic case, we find from Eq. (28) after some manipulation,

$$\langle |\vec{E}_{T+}|^2 \rangle \propto \langle (\overleftrightarrow{T}_+ \overleftrightarrow{F}_+)^\dagger \ (\overleftrightarrow{T}_+ \overleftrightarrow{F}_+) \rangle$$

$$= \begin{pmatrix} \alpha^{+*} & \beta^{+*} \\ \beta^{+*} & -\alpha^{+*} \end{pmatrix} \begin{pmatrix} \dfrac{|1-r_\perp|^2}{1-|r_\perp|^4 \exp(-\gamma\ell)} & 0 \\ 0 & \dfrac{|(1-r_\parallel)n|^2}{1-|r_\parallel|^4 \exp(-\gamma\ell)} \end{pmatrix} \begin{pmatrix} \alpha^+ & \beta^+ \\ \beta^+ & -\alpha^+ \end{pmatrix} \tag{30}$$

where γ is the attenuation constant along $\hat{z}$.

D. Far-Infrared Output Power and Its Far-Field Angular Distribution.

The total far-infrared power outputs from the slab in the forward and backward directions are

$$P_\pm = \frac{c}{2\pi} \int dxdy(\hat{z}\cdot\hat{\Omega}) |\vec{E}_{T\pm}(x,y)|^2 \tag{31}$$

evaluated at large z. By Parseval's Theorem, this can be written as

$$P_\pm = \frac{c}{2\pi} \int_{k_x^2+k_y^2 \leq k^2} dk_x dk_y (\hat{z}\cdot\hat{k}^\pm) |\vec{E}_{T\pm}(\vec{k}_T)|^2 \tag{32}$$

where $\vec{E}_{T\pm}(\vec{k}_T)$ is given by Eq. (28).

In most practical cases, we are also interested in the far-field angular distribution of the output power. As shown in the Appendix of Miyamoto and Wolf,[36] it has the expression

$$\frac{dP_\pm(\theta,\phi)}{d\Omega} = \frac{c}{2\pi} \frac{\omega^2}{c^2} \cos^2\theta |\vec{E}_{T\pm}\{\vec{k}_T = \frac{\omega}{c} \sin\theta(\hat{x}\cos\phi+\hat{y}\sin\phi)\}|^2 \tag{33}$$

III. Results of Numerical Calculations

In this section, we shall present numerical calculations of far-infrared generation by difference-frequency mixing using the equations given in the previous section. We choose somewhat arbitrarily the following values for the characteristic parameters of the nonlinear crystal: $n_o = 2$, $n(\omega) = 4$, and $\chi^{(2)} = 1.87 \times 10^{-6}$ esu. The two nearly overlapped pump beams, one ordinary and one extraordinary, are assumed to have the same focal spot in the crystal with both beams always along the normal to the slab. The question we propose to answer is how various quantities such as phase mismatch, focusing, beam walkoff, and absorption affect the far-infrared output at different frequencies.

A. Far-infrared Generation in the Absence of Absorption and Optical Walkoff

We assume in this case that the optical axis of the crystal is in the plane of the slab along $\hat{x}$. The two pump beams, one ordinary and one extraordinary, propagate along the normal to the slab, $\hat{z}$, with essentially no walkoff, the nonlinear polarization $\vec{P}^{NL}$ is along $\hat{y}$, and the common focal spot of the two pump beams is at the center of the slab. We also assume that the extraordinary refractive index n_{em} of the pump beam can be varied by external means such as temperature in order to adjust the amount of phase mismatch in DFG and that only the ordinary far infrared waves in the forward direction can be nearly phase matched. Since the phase mismatch is different for different Fourier components $\vec{E}(\vec{k}_T,\omega)$ of the far-infrared output, we define an axial phase mismatch $\Delta k_a = k_1(\omega_1) - k_2(\omega_2) - k_o(\omega)$ to describe the overall phase matching condition.

Figure 3 shows the far-field angular distribution of the far-infrared output, $dP(\theta)/d\Omega$ versus θ, at 100 cm^{-1} calculated from Eq. (33). In the calculation the slab has a thickness of 1 cm, the focal spot size is w = 25 μm, and the axial phase mismatch corresponds to $\Delta k_a = -5.1$ cm^{-1}. Since the far-infrared output is approximately symmetric about $\hat{z}$ (i.e., nearly independent of the azimuth angle $\phi = \tan^{-1}(k_y/k_x)$), Fig. 3 actually shows a distribution in the form of a hollow cone. The radiation peaks at the angle $\theta_m = \sin^{-1}\{n_o^2(\omega) - [n_o(\omega) + \Delta k_a c/\omega]^2\}^{1/2}$ at which phase matching $\Delta k_z = k_1 - k_2 - k_{oz}(\omega) = 0$ occurs. The secondary maxima of the phase-matching curve can also be seen. They become more pronounced for shorter far-infrared wavelengths as the effect of diffraction becomes less important. From the expression of θ_m, it is seen that if $\Delta k_a = 0$, then $\theta_m = 0$ and the far-infrared output appears as a narrow solid cone along the z axis. If $\Delta k_a > 0$, then there is no solution for θ_m and the far-infrared output is strongly suppressed by phase mismatch; the angular distribution may show a weak central peak at $\theta = 0$ and some secondary maxima at finite θ. For negative Δk_a, the phase-matched peak shifts to larger θ_m until $\theta_m = \pi/2$; then because of total reflection at the surface, the far-infrared radiation in the phase-matched direction can no longer get out of the slab and the output peak at $\theta = \pi/2$ drops quickly.

The total far-infrared power output P versus Δk_a is shown in Fig. 4 with the same set of parameters used for Fig. 3. The curve has a maximum around $\Delta k_a = -5.1$ cm^{-1} corresponding to the full development of the hollow phase-matched cone in Fig. 3. The steep rise of the

curve at $\Delta k_a \sim 0$ cm^{-1} is due to the initial appearance of the phase-matched cone. The gradual decrease between $\Delta k_z \approx -10$ cm^{-1} and -75 cm^{-1} is due to the combined effects of decrease of the far-infrared transmission coefficients and decrease of the effective $P^{(2)}$ for the generation of ordinary far-infrared waves around the phase-matched direction. The steep drop after $\Delta k_a \approx -75$ cm^{-1} is due to total reflection of an increasing portion of those far-infrared waves generated near phase matching.

If the far-infrared wavelength λ inside the crystal becomes much smaller than the focal spot size w, the variation of far-infrared output versus phase mismatch Δk_a appears more like the usual phase-matching function $(\sin^2 x)/x^2$ for the ideal plane wave case. An example is shown in Fig. 5 for the case of $\lambda = w/8$. Because of the smaller λ/w ratio, the off-axis Fourier components of the far-infrared become relatively less important and hence the output drops more rapidly with increase of Δk_a. The curve in Fig. 5 is, however, still noticeably asymmetric and its peak occurs at $\Delta k_a = -2$ cm^{-1} rather than $\Delta k_a = 0$. As the ratio of λ/w decreases further, the effect of far-infrared diffraction becomes even smaller; the phase-matching curve P versus Δk_a then develops more clearly defined secondary peaks and approaches the symmetric form $\sin^2(\Delta k_a \ell/2)/(\Delta k_a \ell/2)^2$.

The focusing geometry of the Gaussian pump beams is completely characterized by the focal spot size w. In order to see how the far-infrared output varies with focusing, we calculate the $\zeta = 0$ curve in Fig. 6 which shows the maximum of $P(\Delta k_a)$ as a function of w. Because

of the higher pump intensity resulting from tighter focusing, the far-infrared output increases sharply with decrease of w. It, however, reaches a maximum at w = 13 μm as the corresponding reduction of the longitudinal focal dimension takes its toll. It is interesting to note that in the model of collimated Gaussian pump beams with a radius w and with $w^2|E_1E_2|$ = constant, P versus w has no maximum. This is because when $k_T w \ll 1$ for all significant far-infrared Fourier components, $P^{(2)}(\vec{k}_T,z)$ in Eq. (19) becomes independent of k_T and w.

While Figs. 3-6 are for $\omega = 100\ cm^{-1}$, Figs. 7-9 show results of similar calculation for $\omega = 10\ cm^{-1}$. The far-field angular distribution of the output is given in Fig. 7 for two values of the azimuth angle $\phi = \tan^{-1}(k_y/k_x) = 0$ and $\pi/2$. In this case, because $\lambda/w = 10$ is large, far-infrared diffraction is more important; phase matching occurs around $\theta = \pi/4$ and the phase-matched peak is very broad. As a result, the output asymmetry with respect to ϕ shows up because at relatively large θ, the transmission coefficient for the ordinary far-infrared wave across the slab boundaries is different for different ϕ. For $\phi = 0$, the wave is linearly polarized perpendicular to the plane of incidence, while for $\phi = \pi/2$, the wave is linearly polarized in the plane of incidence. The latter case has a Brewster angle at $\theta = 76°$.

Figure 8 shows the total far-infrared output at $\omega = 10\ cm^{-1}$ as a function of the axial phase mismatch Δk_a. The curve again resembles the well-known phase-matching curve $(\sin^2 x)/x^2$ for the plane wave case except that its maximum is at $\Delta k_a = -4\ cm^{-1}$ instead of $\Delta k_a = 0$ and it has no well-defined nodes. However, this resemblance does not

occur because diffraction is unimportant. It occurs because, when the far-infrared wavelength is sufficiently long, then all the far-infrared Fourier components $\vec{E}(\vec{k}_T, z)$ have roughly the same $\Delta k_z \ell \approx \Delta k_a \ell$; in other words, if $\Delta k_a \ell = 0$, then all the far-infrared Fourier components are nearly phase matched. The small difference of $\Delta k_z \ell$ among the Fourier components, however, broadens the phase-matching peak and obscures the fine structure.

The $\zeta = 0$ curve in Fig. 9 describes the peak value of $P(\Delta k_a)$ at $\omega = 10\ cm^{-1}$ as a function of the focal spot size w. We notice that in the range of our calculation, this maximum output power $P_{max}(\Delta k_a)$ always increases with decrease of w. In this case, $k_T w$ becomes so much smaller than 1 at small w that the nonlinear polarization $\vec{P}^{(2)}(\vec{k}_T)$ approaches a constant independent of k_T, w, and z in spite of the factor $(1+\xi^2)$ in the exponential function in Eq. (19). Consequently, the $\zeta = 0$ curve of Fig. 9 flattens out at small w. Eventually, for even smaller w, we should expect the curve to go through a maximum like the $\zeta = 0$ curve in Fig. 6 for $\omega = 100\ cm^{-1}$.

B. Far-Infrared Generation with a Finite Walkoff Angle Between the Pump Beams

We now consider the effect of optical walkoff on far-infrared generation. We still assume that the pump beams propagate normal to the slab and absorption is negligible, but the orientation of the optical $\hat{c}$ axis of the crystal is now varied in the $\hat{x}$-$\hat{z}$ plane in order to vary the walkoff angle ζ. The primary effect of optical walkoff is that it limits the effective interaction length of the beams. When ζ is much larger than the divergence angle of the pump beams, the two

pump beams overlap in the focal region only over a distance of $2w/|\zeta|$; most of the far-infrared radiation is generated from this overlapping region. As $|\zeta|$ increases, the effective interaction length decreases, and hence the phase-matching peak in the far-field angular distribution becomes weaker and broader as shown in Fig. 10 for $\omega = 10\ cm^{-1}$. For smaller focal spot sizes w, the walkoff effect is stronger. This gives rise to a lower maximum at a larger w for the $\zeta \neq 0$ curves in Figs. 6 and 9.

The far-infrared output should in general consist of both ordinary and extraordinary waves. We have so far assumed that the e-wave is strongly phase-mismatched and can be neglected. This is true for $\theta_c = \cos^{-1}(\hat{c}\cdot\hat{z})$ larger than the total reflection angle θ_R. However, when $\hat{c}$ approaches $\hat{z}$ or θ_c approaches zero, the phase mismatch of the e-wave is greatly reduced and the e-wave output becomes non-negligible. For $\theta \approx 0$, we have the nearly degenerate case where the e-wave and the o-wave contribute almost equally to the far-infrared output.

There are two other less important effects of optical walkoff on far-infrared generation. First, the $\exp(ik_x \zeta z/2)$ term in Eq. (19) contributes to the phase matching relation which now becomes $\Delta k_z = k_1 - k_2 + k_x\zeta - k_z = 0$. This term shifts the center of the phase-matching cone in Figs. 3, 7, and 10 from $k_x = 0$ to $k_x = \zeta(\Delta k_a + n_o\omega/c)/2$. Since for $\phi = 0$, the far-infrared transmission coefficient for o-waves at the boundary falls off monotonically with increase of θ, this increases the phase-matched output for $k_x > 0$ and decreases that for $k_x < 0$. Second, as seen from Eq. (19), the maximum of $|\vec{P}^{(2)}(\vec{k}_T, z)|$ is

shifted from $k_x = k_y = 0$ to $k_x = k_1 \zeta\xi^2/(1+\xi^2)$ and $k_y = 0$; its effect on the far-field angular distribution is just the opposite of that due to the shift of the phase matching cone. Depending on the situation, one effect may dominate over the other. They are responsible for the slight asymmetry of the $\zeta = 0$ curves in Fig. 10. The phase-matching effect is more important for the $\zeta = -0.01$ case while the $|P^{(2)}(k_T)|$ effect is more important for the $\zeta = -0.02$ case. For shorter crystals ($\ell \lesssim 0.5$ cm), the phase-matching effect is more important.

C. Effects of Linear Absorption on Far-Infrared Generation

In practice, nonlinear far-infrared generation in crystals is always limited by far-infrared absorption. This is the main reason why far-infrared DFG in solids has in most cases been restricted to the range between 1 and 200 cm^{-1}. Roughly speaking, with an absorption coefficient γ, the effective length of the crystal for DFG cannot be much more than $2/\gamma$.

Figure 11 shows how the far-infrared output from a 1-cm slab decreases as a function of the far-infrared absorption coefficient γ for $\omega = 10$ and 100 cm^{-1}. In the calculation, the focal spot size was chosen as $w = 25$ μm and the location of the focal spot was at the center of the slab for $\gamma = 0$, while for increasing γ it moves towards the end surface of the slab. As we mentioned earlier in Sec. IIIA, for $\omega = 10$ cm^{-1}, all the significant far-infrared Fourier components are nearly phase-matched ($\Delta k_z \ell < \pi$). Therefore, the curve for $\omega = 10$ cm^{-1} in Fig. 11 agrees fairly well with that described by $[1-\exp(-\gamma\ell/2)]^2/(\gamma\ell/2)^2$ for the phase-matched plane wave case. For

$\omega = 100\ cm^{-1}$, since not all the significant far-infrared Fourier components can be nearly phase-matched, the reduction of far-infrared output with increasing absorption is slower and cannot be approximated by the phase matched plane-wave form at small γ.

In some respects, the effects of γ for $\gamma\ell \geqslant 2$ can be simulated by an absorptionless crystal with a length $2\gamma^{-1}$. An increase of γ increases the phase-matching angle and broadens the phase-matched peak in the angular distribution of the far-infrared output. It also makes $(\Delta k_a)_{opt}$, the optimum axial phase mismatch for maximum total far-infrared output, more negative. This latter effect is quite pronounced for $\omega = 100\ cm^{-1}$ as shown in Fig. 12.

IV. Comparison with Other Models and with Calculations of Second Harmonic Generation

We now compare the results of our detailed calculations with those obtained from two simple models for the case where the optical walk-off effect is negligible. One is the Gaussian distribution (GD) model in which we assume a Gaussian profile for the nonlinear polarization at the difference frequency.

$$\vec{P}^{(2)}(\vec{r},t) = (\overleftrightarrow{\chi}^{(2)} : \vec{\mathcal{E}}_1 \vec{\mathcal{E}}_2^*) \exp[-2(x^2+y^2)/w^2 + i(k_1-k_2)z - i\omega t] \qquad (34)$$

in the crystal slab where the pump fields are given by

$$\vec{E}_j(\vec{r},t) = \vec{\mathcal{E}}_j \exp[-(x^2+y^2)/w^2 + ik_j z - i\omega_j t], \quad j = 1,2 .$$

This is an extension of an earlier model used by Zernike and Berman[27] and Faries et al.[26] which assumes a uniform amplitude for $\vec{P}^{(2)}(\vec{r},t)$ throughout a cylinder with a finite radius. The other simple model is the usual plane wave model in which we assume that the geometric ray approximation is valid and that each beam can be described by a cylindrical pencil of rays with a single wave vector.

From the GD model, we obtain for the lossless case a total output power at ω of

$$P_{+}^{GD}(\omega) = \frac{\pi^2 \omega^3 w^4}{4c^2} \left| \overleftrightarrow{\chi}^{(2)} : \vec{\mathcal{E}}_1 \vec{\mathcal{E}}_2^* \right|^2 \ell^2 \times \int_0^{\omega/c} dk_T (k_T/k_{oz}) \langle T(k_T) \rangle_\phi \, C(\Delta k_z) \, e^{-w^2 k_T^2/4} \tag{35}$$

where $\langle T(k_T) \rangle_\phi$ is the far-infrared transmission factor averaged over the azimuthal angle ϕ with multiple reflections at the slab boundaries taken into account, and $C(\Delta k_z)$ describes the effect of phase mismatch. They are given by

$$\langle T(k_T) \rangle_\phi = \frac{1}{2(k_o + k_{oz})} \left[\frac{k_o (k_{oz} + n_o^2 k_z)^2}{k_{oz}^2 + n_o^4 k_z^2} + \frac{(k_{oz} + k_z)^2}{k_{oz}^2 + k_z^2} k_{oz} \right]$$

$$C(\Delta k_z) = \sin^2 (\Delta k_z \ell/2) / (\Delta k_z \ell/2)^2 \tag{36}$$

with $\Delta k_z = n_o \omega/c + \Delta k_a - k_{oz}$ and $\Delta k_a = k_1 - k_2 - n_o \omega/c$.

The output powers at 100 cm^{-1} and 10 cm^{-1} calculated from Eq. (35) as a function of w are shown in Figs. 13 and 14 respectively in comparison with the results of Eq. (32) from our more exact calculations. At 100 cm^{-1}, the only perceptible difference between the two curves occurs at small beam sizes and amounts to 6% at w = 13 μm. At 10 cm^{-1}, the two curves are virtually indistinguishable. Thus, the GD model appears to be a very satisfactory approximation.

The output power from the plane wave model without boundary conditions is given by

$$P^{PW}(\omega) = \frac{\pi^2 \omega^2 w^2}{2\, cn_o} |\chi^{(2)} : \hat{\xi}_1 \hat{\xi}_2^*|^2 \, \ell^2 \langle T(0) \rangle_\phi \qquad (37)$$

The result calculated from Eq. (37) is also shown in Fig. 13. It is 20% higher than the correct value at w = 0.02 cm. The deviation becomes much worse at smaller w and diverges as w approaches zero. This shows that the plane wave model gives unacceptable results at small w because of its diffractionless approximation. With diffraction, the total far-infrared output power is decreased by total reflection of those Fourier components with large k_T and by phase mismatch (described by $C(\Delta k_z)$ in Eq. (35)) for other Fourier components.

The plane wave calculation is, however, simple and does not require numerical integration. It is therefore preferred when one wants to crudely estimate the output power. We can make the estimate more exact by multiplying the calculated result by a correction factor. Comparison of Eq. (35) and (37) shows that this correction factor is given by

$$F = P^{GD}/P^{PW}$$
$$= \frac{k_o w^2}{2\langle T(0)\rangle_\phi} \int_0^{\omega/c} dk_T \left(\frac{k_T}{k_{oz}}\right) \langle T(k_T)\rangle_\phi \; C(\Delta k_z) \; e^{-w^2 k_T^2/4} \quad . \tag{38}$$

We approximate $\langle T(k_T)\rangle_\phi \; C(\Delta k_z)/k_{oz}$ in the integral by $\langle T(0)\rangle_\phi/k_o$ for $k_T < k_M$ and by 0 for $k_T > k_M$[37] where k_M is defined as $k_M = \sqrt{2\Delta k_c (n_o\omega/c - \Delta k_c/2)}$ with Δk_c being the smaller of the two quantities $2\pi/\ell$ and $(n_o - \sqrt{n_o^2-1})\omega/c$. Physically, at $k_T = k_M$, $dP/d\Omega$ either has dropped to half of its peak value or has been cutoff by total reflection. The correction factor then becomes

$$F = 1 - \exp(-k_M^2 w^2/4) \quad . \tag{39}$$

The output power calculated from FP^{PW} using Eqs. (37) and (39) is within 20% of the correct value.

We now discuss similarities and differences between difference-frequency generation (DGF) and second-harmonic generation (SHG). In both cases, each pump field $\vec{E}_i$ with finite beam radius has a distribution of Fourier components with wave vectors spreading effectively over an angle $2\delta_i$. The output of DFG or SHG from a nonlinear slab is significant only when part of these significant Fourier components within the angular spread $2\delta_i$ can satisfy the axial phase matching condition $\Delta k_z = 0$. As shown in Fig. 15, this happens for SHG only if $\Delta k_a^S \equiv 2k(\omega_1) - k(2\omega_1) \geq 0$ and $\Delta k_R^S \equiv 2k(\omega_1)(1-\cos\delta_1) \geq \Delta k_a^S$, and for DFG only if $\Delta k_a^D \equiv k_1 - k_2 - k(\omega) \leq 0$ and $\Delta k_R^D \equiv k(\omega)(1-\cos\delta) \geq -\Delta k_a^D$, where 2δ is the angular spread of the significant far-infrared Fourier components which can get out of the crystal slab. We emphasize that for an efficient nonlinear interaction we must have $\Delta k_a^S \leq 0$ for SHG and $\Delta k_a^D \geq 0$ for DFG.

The quantity Δk_R^S in SHG or Δk_R^D in DFG governs the qualitative behavior of the phase-matching curve P versus Δk_a. As we mentioned before, the output is most efficient when Δk_a^S (or $-\Delta k_a^D$) falls in the range between 0 and Δk_R^S (or Δk_R^D). Therefore, if Δk_R^S (or $\Delta k_R^D \ell$) $\gg 2\pi$, then the phase-matching curve has a broad peak; it rises sharply to the peak around Δk_a^S (or Δk_a^D) = 0, then slopes downward as $\Delta k_a^S \ell$ (or $-\Delta k_a^D$) increases from 0 to Δk_R^S (or Δk_R^D), and finally in the case of DFG falls rapidly at a certain Δk_a^D value because of the cutoff due to total reflection at the boundaries. Examples are shown in Fig. 4 for DFG with $\Delta k_R^D \ell = 80$ and in Fig. 16 for SHG with $\Delta k_R^S \ell = 100$.[31] Such a phase-matching curve is characteristic of SHG with strong focusing of the pump beam. In DFG, it occurs when the pump beams are more weakly focused because of large far-infrared diffraction. When $\Delta k_R^S \ell$ (or Δk_R^D) $\lesssim 2\pi$ the range of Δk_a^S (or Δk_a^D) for efficient output is much narrower, and the phase-matching curve now shows a central peak and secondary maxima and minima, resembling the well-known plane-wave phase-matching curve described by $\sin^2(\Delta k \ell/2)/(\Delta k \ell/2)^2$. Examples are shown in Fig. 5 for DFG at 100 cm^{-1} with $\Delta k_R^D \ell = 4$, in Fig. 9 for DFG at 10 cm^{-1} with $\Delta k_R^D \ell = 8$, and in Fig. 17 for SHG with $\Delta k_R^S \ell = 5.68$. All these curves are, however, slightly asymmetric with a small shoulder on one side. This is because for $\Delta k_a^S \ell < 0$ (or $\Delta k_a^D > 0$), the phase-matching condition $\Delta k_z = 0$ is not satisfied for any of the Fourier components.

There are several minor differences between the SHG and DFG phase matching functions. For $\Delta k_R^S \ell$ (or $\Delta k_R^D \ell$) $\gg 2\pi$, the phase-matching curve

for DFG, as shown in Fig. 4, has a sharp drop around the value of Δk_a^D where significant Fourier components of the far-infrared output begin to be totally reflected at the boundaries. In SHG, however, total reflection is never important and therefore as shown in Fig. 16, no sudden drop of the output power occurs as Δk_a^D increases. Because of the weaker diffraction effect, the phase-matching curve for SHG has, in general, more pronounced fine structure than that for DFG.

V. Conclusion

We have developed here the theory of far-infrared generation by optical mixing in a nonlinear medium, using an extension of a formalism developed earlier for second-harmonic generation by focused laser beams. The theory takes into account the effects of focusing, diffraction, and double refraction of the pumped beams and the effects of diffraction, absorption and reflections at the boundaries of the far-infrared output beam. Numerical calculations showing these effects are presented. Both the total power output and its angular distribution are calculated.

We have found that focusing of the pump beams can greatly enhance the far-infrared output. In a crystal of 1 cm long, the optimum focal spot radius is roughly equal to or smaller than the far-infrared wavelength for output frequencies less than 100 cm^{-1}. The walkoff effect of the pump beams in birefringent crystals does not reduce the output by more than a factor of 2. Far-infrared absorption and boundary reflections are however extremely important. The former is often the factor which limits the output power.

We show that the usual plane-wave model which neglects the effects of far-infrared diffraction and boundary reflections does not give a correct description of the far-infrared output, especially for tightly focused pump beams. A simple model treating the non-linear polarization as a constant 1/e radius Gaussian distribution of radiating dipoles is, however, a good approximation to the real picture. We also compare our results with those of second-harmonic generation and notice a great deal of similarities. Most of the differences can be ascribed to the boundary effects including total reflection which are more important in the case of far-infrared generation.

REFERENCES

1. For a recent review of nonlinear optical processes for generating far-infrared radiation which covers both applicable DFG experiments and basic theory see Y. R. Shen, Prog. Quantum. Electron. 4, 207 (1976).

2. K. H. Yang, J. R. Morris, P. L. Richards, and Y. R. Shen, Appl. Phys. Lett. 23, 669 (1973).

3. D. H. Auston, A. M. Glass, and P. LeFur, Appl. Phys. Lett. 23, 47 (1973).

4. F. Zernike, Bull. Am. Phys. Soc. 12, 687 (1967).

5. T. Y. Chang, N. VanTran, C. K. N. Patel, Appl. Phys. Lett. 13, 357 (1968).

6. N. VanTran and C. K. N. Patel, Phys. Rev. Lett. 22, 463 (1969).

7. C. K. N. Patel and N. VanTran, Appl. Phys. Lett. 15, 189 (1969).

8. T. J. Bridges and T. Y. Chang, Phys. Rev. Lett. 22, 811 (1969).

9. F. Zernike, Phys. Rev. Lett. 22, 931 (1969).

10. N. VanTran, A. R. Strnad, A. M. Jean-Louis, G. Duraffourg, in The Physics of Semimetals and Narrow Gap Semiconductors, D. L. Carter and R. T. Bates, ed. (Pergamon, N. Y., 1971) p.231.

11. V. T. Nguyen and T. J. Bridges, Phys. Rev. Lett. 29, 359 (1972).

12. T. J. Bridges and A. R. Strnad, Appl. Phys. Lett. 20, 382 (1972).

13. G. D. Boyd, T. J. Bridges, C. K. N. Patel, and E. Buelher, Appl. Phys. Lett. 21, 553 (1972).

14. R. L. Aggarwal, B. Lax, and G. Favrot, Appl. Phys. Lett. 22, 329 (1973).

15. B. Lax, R. L. Aggarwal, and G. Favrot, Appl. Phys. Lett. 23, 679 (1973).

16. N. Lee, R. L. Aggarwal, and B. Lax, Opt. Commun. 11, 339 (1974).

17. T. J. Bridges and V. T. Nguyen, Appl. Phys. Lett. 23, 107 (1973).

18. V. T. Nguyen and T. J. Bridges, in Laser Spectroscopy, R. G. Brewer and A. Mooradian, eds., (Plenum, N.Y., 1974) pp. 513-521.

19. T. J. Brignall, R. A. Wood, C. R. Pidgeon, and B. S. Wherrett, Opt. Commun. 12, 17 (1974).

20. V. T. Nguyen and T. J. Bridges, Appl. Phys. Lett. 26, 452 (1975).

21. T. Yajima and K. Inoue, IEEE J. Quantum Electron. 5, 140 (1969).

22. F. deMartini, Phys. Lett. 30A, 547 (1969).

23. F. deMartini, Phys. Lett. B 4, 4556 (1971).

24. D. W. Faries, P. L. Richards, Y. R. Shen, and K. H. Yang, Phys. Rev. A3, 2148 (1971).

25. T. L. Brown and P. A. Wolff, Phys. Rev. Lett. 29, 362 (1972).

26. D. W. Faries, K. A. Gehring, P. L. Richards, and Y. R. Shen, Phys. Rev. 180, 363 (1969).

27. F. Zernike, Jr. and P. R. Berman, Phys. Rev. Lett. 15, 999 (1965).

28. D. W. Faries, Ph.D. Thesis, University of California, Berkeley (1969).

29. J. E. Bjorkholm, Phys. Rev. 142, 126 (1966).

30. D. A. Kleinman, A. Ashkin, and G. D. Boyd, Phys. Rev. 145, 338 (1966).

31. G. D. Boyd and D. A. Kleinman, J. Appl. Phys. 39, 3597 (1968).

32. See, for example, P. C. Clemmow, The Plane Wave Spectrum Representation of Electromagnetic Fields (Pergamon, New York, 1966) and E. Lalor, J. of Math. Phys. 13, 437 (1972) for discussions of this method.

33. Optical Rectification was first reported by M. Bass, P. A. Franken, J. F. Ward, and G. Weinreich, Phys. Rev. Lett. 9, 446 (1962). For a discussion of the theory of optical rectification see M. Bass, P. A. Franken, and J. F. Ward, Phys. Rev. 138A, 534 (1965).

34. N. Bloembergen, Non-linear Optics (Benjamin, New York, 1965) pp. 74-81.

35. M. Berek, Z. Kristallog. 76, 396 (1931). The fields in this work are magnetic fields (in-spite-of notation which suggests they are electric fields) because the Brewster's angle occurs for the "senkrecht" or perpendicular polarization. After these equations are rewritten in-terms-of electric fields, the "one-ray" coefficients are the elements of our $\overleftrightarrow{A}$ and $\overleftrightarrow{B}$ matrices. For an English translation with some typographical errors see G. N. Ramachandran and S. Ramasesham, "Crystal Optics" in Handbuch der Physik, S. Flugge, ed., Vol. XXV/1 (Springer-Verlag, Berlin, 1961) pp. 117-119.

36. K. Miyamoto and E. Wolf, J. Opt. Soc. Am. 52, 615 (1962). Note that their definition of the Fourier transform is smaller than our definition by a factor of $1/2\pi$.

37. For tightly focused $\exp[-w^2k_T^2/4] \cong 1$ when $k_T < \frac{\omega}{c}$, and this factor can be pulled outside the integral in Eq. (35) along with $\langle T(k_T)\rangle_\phi$. Then, the remaining integral is $\int_0^{\omega/c} k_T dk_T C(\Delta k_z)/k_{oz}$ which has the value $\simeq \pi/\ell$ for thick crystals or high far-infrared frequencies and the value $\simeq (\omega/2c)\left[n(\omega)-\sqrt{n^2(\omega)-1}\right]$ for thin crystals or low far-infrared frequencies.

CHAPTER III. FAR-INFRARED GENERATION BY PICOSECOND PULSES IN ELECTRO-OPTIC MATERIALS

The development of high power mode-locked lasers with pulse widths in the picosecond range has made optical rectification a feasible method of generating broadband radiation of high peak power (~ 1 KW), as supported by the recent experimental results.[1] Theoretically, Gustafson et al.[2] have calculated the rectified field for an infinite plane wave in the limit that the optical and far infrared phase velocities differ negligibly. They have also neglected reflection and refraction at the crystal boundaries. This letter reports a more realistic calculation which includes the various effects due to a finite beam cross-section, crystal boundaries, and the significantly different optical and far-infrared phase velocities.

Consider a short laser pulse incident normally on a thin slab of electro-optic material. The slab has a transverse dimension much larger than the beam diameter, and we can assume that the laser pulse propagating in the slab in a single transverse mode is given by[3,4]

$$\underset{\sim}{E}_{\ell} = \sum_j \underset{\sim}{E}_{\ell j}\,(r,t) \text{ with}$$

$$\underset{\sim}{E}_{\ell j}(\underset{\sim}{r},t) = \underset{\sim}{\mathcal{E}}_{\ell j}\left\{\frac{1}{(1+i\xi_j)}\exp\left[-\frac{x^2+y^2}{w_o^2(1+i\xi_j)} - \frac{(n_j z/c-t)^2}{\sigma^2} + \right.\right.$$

$$\left.\left. + i\,\omega_o(n_j z/c - t) + i\phi\right]\right\} \qquad (40)$$

where w_o is the beam radius in the focal plane, σ is the pulse width, $\xi_j = (L + z/n_j)/(\omega_o w_o^2/2c)$, L is the distance between the focal point

and the front surface of the slab, and z is the distance away from the front surface into the slab. The subindex, j, indicates the polarization state of the laser field. The other quantities have their usual physical meaning.

The laser pulse induces in the slab a nonlinear polarization at difference frequencies of the form

$$\underset{\sim}{P}^{NL}(\underset{\sim}{r},t) = \underset{\approx}{\chi}^{NL} : \; E_{\ell} E_{\ell}^{*} \tag{41}$$

if we neglect the dispersion of the nonlinear susceptibility $\underset{\approx}{\chi}^{NL}$. The far infrared radiation field $\underset{\sim}{E}(\underset{\sim}{r},t)$ generated in the slab can then be obtained by solving the wave equation

$$\left[\nabla \times (\nabla \times) + (\underset{\approx}{\varepsilon}/c^2) \frac{\partial^2}{\partial t^2}\right] \underset{\sim}{E}(\underset{\sim}{r},t) = -\frac{4\pi}{c^2} \frac{\partial^2}{\partial t^2} \underset{\sim}{P}^{NL}(\underset{\sim}{r},t) \tag{42}$$

with the proper boundary conditions. Here, we have also neglected the dispersion of $\underset{\approx}{\varepsilon}$.

To solve Eq. (42), we use essentially the scheme of Bjorkholm.[4] From the Fourier transform of $\underset{\sim}{E}(\underset{\sim}{r},t)$ and $\underset{\sim}{P}^{NL}(\underset{\sim}{r},t)$ on x, y and t, we obtain the Fourier components $\underset{\sim}{E}\,(\underset{\sim}{k}_T,\omega,z)$ and $\underset{\sim}{P}^{NL}(\underset{\sim}{k}_T,\omega,z)$ respectively. We then use the Green's function method to find $\underset{\sim}{E}(\underset{\sim}{k}_T,\omega,z)$. Although far-infrared radiation is generated in the slab in all directions, only the part which propagates in forward and backward directions with nearly normal incidence on the plane surfaces of the slab can get out of the slab because of the large refractive index of a crystal in the far infrared. If we are interested only in that part of the far-infrared

radiation, then we can use the Green's function for normal incidence as an approximation in finding $\underset{\sim}{E}(\underset{\sim}{k}_T,\omega,z)$. Multiple reflections at the plane boundaries of the slab are clearly important, so that the solution should be proportional to a Fabry-Perot factor. For far-infrared field in the i polarization state, we find at the back surface of the slab, $z = \ell$,

$$\underset{\sim}{E}_i(\underset{\sim}{k}_T,\omega,\ell) = F_i[\underset{\sim}{E}_i^{(S)}(\underset{\sim}{k}_T,\omega,z=\ell)-R_i E_i^{(S)}(\underset{\sim}{k}_T,\omega,z=0)\exp(i\omega n_i^{(\omega)}\ell/c)] \qquad (43)$$

with[5]

$$\underset{\sim}{E}_i^{(S)} = (2\pi i\omega/cn_i^{(\omega)})\int_o^{\ell} dz'\ \underset{\sim}{P}_i^{NL}(\underset{\sim}{k}_T,\omega,z')\exp(i\omega n_i^{(\omega)}|z-z'|/c)$$

where $F_i \cong (1-R_i)/[1-R_i^2\exp(i2\omega n_i^{(\omega)}\ell/c)]$ is the Fabry-Perot factor, and $R_i = (1-n_i^{(\omega)})/(1+n_i^{(\omega)})$ is the reflection coefficient for the i polarization state.

Experimentally, the far infrared output from the slab is collected by a tapered light pipe leading to a solid-state detector.[6] Since wave propagation in the light pipe has a cutoff angle ϕ_M, the total far infrared power seen by the detector is given by

$$P_i(\omega) = (c/2\pi)\int_o^{|k_T|=(\omega/c)\sin\phi_M} d^2k_T\ |\underset{\sim}{E}_i(\underset{\sim}{k}_T,\omega,\ell)|^2\cos\phi \qquad (44)$$

where $\phi = \sin^{-1}(k_T c/\omega) \leq \phi_m$. To calculate $P_i(\omega)$ from Eq. (44) with the help of Eqs. (40), (41), and (43), we use the following approximations. We assume that the cross-section of the laser beam remains unchanged

in traversing the thin slab. If both ordinary and extraordinary laser beams are present, then we also assume that walkoff of the two beams in the slab is negligible. Both assumptions are clearly good approximations when the slab is not unusually thick (< a few mm.). Since ϕ_m is often small, we also approximate cosϕ by 1 in Eq. (44). Then, if χ^{NL}_{ijk} is the only dominating nonlinear susceptibility in difference-frequency generation, we find, for a slab of thickness ℓ,

$$P_i(\omega) = I_i A |F_i|^2 M_i D S \tag{45}$$

where[7]

$$I_i = (\pi/2c)(\omega\sigma/n_i^{(\omega)})^2 \left|\chi^{NL}_{ijk}\, \mathcal{E}_{\ell j} \mathcal{E}_{\ell k}/(1+\xi^2)\right|^2 \ell^2$$

$$A = \pi w_o^2 (1+\xi^2)/4, \qquad \xi = \xi_j \ (z=0)$$

$$M_i = \left|(M^-_{ijk} + M^-_{ikj}) - R_i\,(M^+_{ijk} + M^+_{ikj})\right|^2$$

$$M^{\pm}_{ijk} = [1 - \exp\,(i\Delta k^{\pm}_{jk}\ell)]/i\Delta k^{\pm}_{jk}\ell$$

$$\Delta k^{\pm}_{jk} = (1/c)[(\omega_o+\omega/2)n_j^{(\omega_o)} - (\omega_o-\omega/2)n_k^{(\omega_o)} \pm \omega n_i^{(\omega)}]$$

$$D = 1 - \exp[-(\omega^2/4c^2)\, w_o^2(1+\xi^2)\, \sin^2\,\phi_m]$$

$$S = \exp\,(-\omega^2\sigma^2/4)\ .$$

The various quantities in the above equation have the following physical meanings. A is the effective cross-section of the beam at the slab. $M^{\pm}_{ijk}$ takes care of the phase mismatch in the difference-frequency generation process, with Δk^{-}_{jk} and Δk^{+}_{jk} being the average momentum mismatches for far-infrared waves propagating in the forward and backward directions respectively. D accounts for the diffraction effect due to the finite beam cross-section. S is the spectral content of the picosecond laser pulse. Finally, $I_i A$ gives the far-infrared power spectrum if all the other factors in Eq. (45) are unity.

We now use Eq. (45) to calculate the spectra of the far-infrared output for two cases. In the first case, a 0.1 cm. $LiNbO_3$ slab is oriented with the c-axis parallel to the plane surfaces of the slab. A 2-psec. laser pulse at 1.06 μ, polarized along the c-axis, is normally incident on the slab, so that χ^{NL}_{33} is the only nonlinear susceptibility responsible for the difference-frequency generation. With $\hat{j} = \hat{k} = \hat{i}$ along $\hat{c}$ and $n_i^{(\omega_o)} \neq n_i^{(\omega)}$ in Eq. (45), phase matching occurs only at $\omega = 0$. The calculated spectrum is shown in Fig. 18. The dashed curve gives the spectrum without the Fabry-Perot boundary condition. The peaks at 5, 8.4, and 11.8 cm^{-1} are the secondary peaks of the phase-matching curve, which would have the major phase-matching peak at $\omega = 0$ if it were not for the low-frequency cutoff. This low-frequency cutoff is mainly due to the ω^2-dependent radiation effects, and gives rise to the first peak at 2 cm^{-1}. The diffraction effect (D) only makes the cutoff even sharper, but does not affect the spectrum significantly beyond the first peak. On the high-frequency side, the spectrum is

limited by the spectral content S of the input pulse. With the Fabry-Perot boundary condition included, the spectrum is then modified by the interference pattern, as shown by the solid curve with spikes in Fig. 18. For an input pulse of 1 - GWatt peak power, the total far-infrared output energy is about 0.1 erg. Our results here agree with those of Gustafson et al.[2] in the limit $n_i^{(\omega)} = n_i^{(\omega_o)}$ and when diffraction and boundary conditions are neglected.

In the second case, the $LiNbO_3$ slab is oriented with the c-axis tilted at 16.8° away from the normal of the slab and the a-axis is in the plane defined by the c-axis and the normal. The normally incident laser pulse is linearly polarized at 45° with respect to the plane such that only χ_{24}^{NL} is responsible for the difference-frequency signal with polarization perpendicular to the plane. We then find from Eq. (45) that the phase-matching conditions $\Delta k_{jk}^{-} = 0$ and $\Delta k_{kj}^{+} = 0$, for far infrared generation in the forward and the backward directions, respectively, can be satisfied at $\omega = 15$ and 7.5 cm^{-1}, respectively. The far-infrared spectrum is then essentially the superposition of the two phase-matching curves modified by $\omega^2 S(\omega)$ and the boundary conditions. If the boundary conditions are neglected ($R_i = 0$), then only the far-infrared generated in the forward direction contributes to the spectrum as represented by the dashed curve in Fig. 19. With the boundary conditions, $R_i \neq 0$, the far-infrared generated in the backward direction now appears in the output. Its spectrum dominates over that of the far-infrared generated in the forward direction because of the high-frequency cutoff due to $S(\omega)$. The total spectrum

is given by the solid curve in Fig. 19, where the spikes are again the result of Fabry-Perot interference. Diffraction has little effect in this case. For a laser pulse with a 1 - GWatt peak power, the total far-infrared energy generated here is 0.0064 erg. Both cases discussed above have been investigated experimentally. Preliminary results show good agreement with our theoretical calculations.[1]

The time dependence of the far-infrared pulse must also be understood, especially the features responsible for the oscillation periods in the spectra of Figs. 18 and 19. These oscillation periods are due to the following three characteristic times: the far-infrared round-trip time, the sum of the optical and far-infrared transit times, and the difference of the optical and far-infrared transit times. The far-infrared round-trip time, $\tau_{rt} = 2n_i(\omega)\ell/c$, is responsible for the prominent Fabry-Perot oscillation period in the solid curves of Figs. 18 and 19. The sum and difference of the far-infrared and optical transit times, $\tau_{\pm} = (n_i(\omega) \pm n_j)\ell/c$, are responsible for the node spacing of the backward and forward phase-matching functions, respectively. Since the characteristic times are independent of the temporal pulse shape, we choose a square pulse to illustrate the significance of $\tau_{\pm}$. We shall also ignore diffraction in the following discussion.

Ignoring diffraction reduces Eq. (42) to a pair of scalar one-dimensional wave equations, one for the far-infrared o-ray and another for the e-ray:

$$\left[-\frac{\partial^2}{\partial z^2}+\frac{n_i^2}{c^2}\frac{\partial^2}{\partial t^2}\right] E_i(z,t) = -\frac{4\pi}{c^2}\frac{\partial^2}{\partial t^2} P_i(z,t) \tag{46}$$

where $P_i = \hat{i}\cdot\vec{P}^{NL}(z,t)/[1-(\hat{i}\cdot\hat{z})^2]$, $\hat{i}$ is the direction of the electric field, and n_i is the far-infrared refractive index for the o- or e-ray. When the nonlinear slab is imbedded in a medium with an identical linear dielectric tensor (reflectionless boundary conditions), the solution of Eq. (46) can be written down immediately from the standard Green's function for an outgoing-wave:[8]

$$E_i(z,t) = -\int_o^{\ell} dz' \int_{-\infty}^{\infty} dt' H(t-t'-\frac{|z-z'|}{c} n_i) \frac{2\pi}{n_i c}\frac{\partial^2}{\partial t'^2} P_i(z',t') \tag{47b}$$

$$E_i(z,t) = -\int_o^{\ell} dz' \frac{2\pi}{n_i c}\frac{\partial}{\partial t'} P_i(z',t-\frac{|z-z'|}{c} n_i) \tag{47b}$$

where H(u) is the unit step function [$H(u) \equiv 0$ for $u < 0$, and $H(u) \equiv 1$ for $u \geq 0$].

The case in which an optical o- or e-ray beats with itself is most easily understood by following a short pulse through the nonlinear slab. First, between its entry at $z = 0$ and its arrival at $z = \ell$ the optical pulse creates the same transmitted and reflected far-infrared pulses as it would if the nonlinear medium filled the entire half-space to the right of the $z = 0$ interface. Since P_i is proportional to the optical intensity and dispersion is ignored, the solution of Eq. (46) for a single interface at $z = 0$ can be written down immediately from the solution for a monochromatic plane wave.[9] Its transmitted

inhomogeneous $[E_i^p(z,t)]$, transmitted homogeneous, and reflected homogeneous far-infrared pulses are given by:

$$E_i^p(z,t) = -\frac{4\pi}{n_i^2-n_j^2} P_i(0,t-zn_j/c) \qquad \text{for} \quad z > 0, \tag{48a}$$

$$E_i^r(z,t) = \frac{n_i-n_j}{2n_i} E_i^p(0,t+zn_i/c) \qquad \text{for} \quad z < 0, \tag{48b}$$

$$E_i^t(z,t) = -\frac{n_i+n_j}{2n_i} E_i^p(0,t-zn_i/c) \qquad \text{for} \quad z > 0 \ . \tag{48c}$$

(E^p, E^r, and E^t are zero in the half-spaces not described in Eq. (48).) At $z = 0$ all three of these pulses have the time-dependence of the optical intensity, except for sign reversals. Next, when the inhomogeneous pulse arrives at the $z = \ell$ interface, it generates another reflected and another transmitted far-infrared pulse. At $z = \ell$ both of these pulses and the optical intensity have identical time-dependence; also, the reflected and transmitted pulses have opposite polarity from the corresponding pulse generated at $z = 0$ because the inhomogeneous pulse propagates toward the $z = \ell$ interface, but away form the $z = 0$ interface. Finally, the homogeneous transmitted pulse from $z = 0$ and the homogeneous reflected pulse from $z = \ell$ arrive at and pass through the opposite surface. Since each of these pulses automatically satisfies the (linearly) reflectionless boundary conditions at the opposite surface, the transmitted (reflected) far-infrared wave is the sum of the transmitted (reflected) homogeneous pulses from $z = 0$ and $z = \ell$.

Figure 20 illustrates this case for a 2 psec square input pulse and the crystal parameters of the calculation shown in Fig. 18. The two opposite polarity single-surface pulses discussed above are clearly present in both the transmitted (lower curve) and reflected (upper curve) far-infrared fields. The first pulse of the transmitted electric field coincides with the optical pulse at $z = \ell$ and the second follows it after a delay of the optical minus the far-infrared transit time. This delay of 9.5 psec causes the prominent 3.51 cm^{-1} oscillation in both curves of Fig. 18. The reflected electric field at $z = 0$ (upper curve) is similar. The first pulse is the reflection off the input ($z = 0$) face of the slab while the second is the reflection off the exit ($z = \ell$) face. The time lag between the two pulses, $\tau_+ = 24.167$ psec, generates a 1.38 cm^{-1} oscillation period in the solid curve in Fig. 18 which, unfortunately, is obscured by the 0.99 cm^{-1} Fabry-Perot oscillation period. However, the 1.38 cm^{-1} period is clearly present in the spectrum of the sum of the forward wave and the first reflection of the backward wave that, for the 2 psec square pulse, is shown in Fig. 21.

Figure 22 illustrates the time-dependence of the electric field generated by the beating of the o-ray and e-ray components of a single 2 psec square optical pulse for reflectionless boundary conditions. The crystal parameters are those used for the calculation shown in Fig. 19. As in Fig. 20, there are two regions of approximately 2 psec duration separated by τ_+ in the backward wave at $z = 0$ (upper curve) or by τ_- in the forward wave at $z = \ell$ (lower curve) which are due to the single surface nonlinear reflections or transmissions. The signal

between the two surface pulses is due to the interference of the radiation generated by the leading and trailing edges of the pulse; its amplitude depends critically on the pulse length and is largest when $\omega_{\pm k}\tau = (2m+1)\pi$ $m = 0,1,\ldots$ (see Appendix D). Both during and between the surface pulses, the time dependence is nearly sinusoidal with a frequency that is given approximately by the corresponding phase-matching condition $\Delta k^{-}_{jk} = 0$ or $\Delta k^{+}_{jk} = 0$.

The nearly sinusoidal time dependence is easily explained: Due to the different o- and e-ray phase velocities, the square pulse creates a standing wave modulation, $\cos[(n_j-n_k)\omega_0 z/c]$, of the nonlinear polarization (plus a propagating second harmonic modulation that doesn't concern us here) within the moving window determined by its duration. If the input beam were continuous wave, this polarization would have no time dependence and could not radiate; however, the motion of the pulse edges creates a time-dependent source. (In the one-dimensional plane wave case, only these edges radiate.) If we consider just the effect of the leading edge of the pulse on the far-infrared wave at $z = \ell$, the radiation arriving at time t was generated at the retarded time $t' = t-(\ell-z')n_i/c$ at the point in space $z' = ct'/n_j$ which the leading edge then occupied; thus, the relationship between the time of observation at $z = \ell$ and the point of emission is $t - \ell n_i/c = z'(n_j-n_i)/c$, and the contribution of the leading edge is sinusoidal at the difference frequency $\omega = \omega_o(n_j-n_k)/(n_i-n_j)$. This is approximately the frequency at which $\Delta k^{-}_{jk} = 0$ when $n_i-n_j \gg n_j-n_k$. Between the two surface pulses the velocity difference between the

leading (c/n_j) and trailing (c/n_k) edges causes a deviation from a truly sinusoidal field that is negligible unless the optical birefringence is large.

We have neglected dispersion and absorption in the above discussion. They can, however, be easily incorporated in the computer spectrum calculations. The effects vary from crystal to crystal. In $LiNbO_3$, the absorption coefficient, α, in the far-infrared is roughly proportional to ω^2. ($\alpha \sim 18$ cm^{-1} at 30 cm^{-1}).[10] The decrease of the far-infrared power due to absorption is less than 20% below 10 cm^{-1}. We have also neglected the effect of possible frequency chirping of a mode-locked pulse.[11] This is not important here since, in the product $E_{\ell j}E^*_{\ell k}$, any phase modulation in $E_{\ell j}$ is almost completely cancelled out by the same phase modulation in $E^*_{\ell k}$. Finally, for a train of N identical mode-locked pulses with a time interval τ between pulses, the far-infrared spectrum of Eq. (45) should be modified by the factor $|[1-\exp(iN\omega\tau)]/[1-\exp(i\omega\tau)]|^2$. The total far-infrared energy is increased by a factor of N.

REFERENCES

1. D. W. Faries, P. L. Richards, J. W. Shelton, Y. R. Shen, and K. H. Yang, International Quantum Electronics Conference, Kyoto, Japan, (1970) Paper 8-6; T. Yajima and N. Takeuchi, ibid., Paper 8-5.

2. T. K. Gustafson, J-P. E. Taran, P. L. Kelley, and R. Y. Chiao, Optics Comm. 2, 17 (1970).

3. D. W. Faries, Ph.D. Thesis, University of California, Berkeley, unpublished (1969).

4. J. E. Bjorkholm, Phys. Rev. 142, 126 (1966).

5. For extraordinary far-infrared ray, the equation should be modified to take into account the fact that $\underset{\sim}{E}$ is not perpendicular to $\underset{\sim}{k}$. See J. A. Armstrong, N. Bloembergen, J. Ducuing, and P. S. Pershan, Phys. Rev. 127, 1918 (1962).

6. See, for example, P. L. Richards in "Far Infrared Properties of Solids", edited by S. S. Mitra and S. Nudelman (Plenum Press, New York, 1970), p. 111.

7. For $j = k$, we should replace I_i by $I_i/4$ if we use the conventional definition for χ^{NL}_{ijj}.

8. See, for example, P. M. Morse and H. Feshbach, Methods of Theoretical Physics, (McGraw-Hill, New York, 1953), p.843.

9. See, for example, N. Bloembergen, Nonlinear Optics, (Benjamin, New York, 1965). pp. 74-81.

10. D. R. Bosomworth, Appl. Phys. Letters 9, 58 (1966); J. G. Berman, A. Ashkin, A. A. Ballman, J. M. Dziedzic, H. J. Levinstein, and R. G. Smith, Appl. Phys. Letters 12, 92 (1968).

11. E. B. Treacy, Appl. Phys. Letters 17, 14 (1970).

CHAPTER IV. PHASE MATCHED FAR-INFRARED GENERATION BY DIFFERENCE-FREQUENCY MIXING OF TWO DYE LASER BEAMS

I. Introduction

The use of non-linear difference-frequency mixing of optical or infrared lasers to generate tuneable far-infrared radiation has been experimentally demonstrated many times.[1-10] Various combinations of lasers and non-linear crystals have been used: temperature-tuned ruby lasers with $LiNbO_e$;[1,3] grating tuned CO_2 lasers with InSb,[2] $ZnGeP_2$,[4] and GaAs;[7-9] a spin-flip Raman laser and a CO_2 laser with InSb;[6] and grating tuned ruby pumped dye lasers with $LiNbO_3$, ZnO, and CdS[10] and with reduced (black) $LiNbO_3$.[5] Only the dye laser system has demonstrated output that can be continuously tuned over the entire 20 to 190 cm^{-1} frequency range with a single laser system.[10] Although the ruby pumped dye laser systems have a low repetition rate, the results obtained with them suggest that a suitably chosen flashlamp pumped dye laser system could be used to generate a greater than 1 Hz repetition rate, continuously tunable, far-infrared source using a $LiNbO_3$ crystal; this source would operate from 20 to 160 cm^{-1} with a peak power of at least a few milli-watts.

This chapter describes the difference frequency generation of continuously tunable far-infrared radiation in the 20 to 190 cm^{-1} frequency range using two distinct ruby-pumped dye laser systems. In the experiments described here, we observed far-infrared radiation in the 20 to 160 cm^{-1} range with various phase-matching schemes in $LiNbO_3$: forward collinear (FCPM), backward collinear (BCPM), and noncollinear

(NCPM). We have also investigated FCPM in ZnO, ZnS, CdS, and CdSe at selected frequencies as high as 190 cm^{-1}. The observed far-infrared power is summarized in Table 1.

II. Synopsis of Plane-wave Theory

A. Plane-wave Theory for Collinear Phase Matching

Because our optical focal spot diameter of 3 mm was much larger than any of the far-infrared wavelengths that we investigated in $LiNbO_3$, the plane wave theory of difference frequency generation (see Eq. (37) of Chapter II) adequately describes our experimental results above 40 cm^{-1}. When, as in our experiments, the optical absorption is negligible and only $\chi^{(2)}_{24}$ contributes to the difference-frequency signal, the far-infrared power can be approximated by

$$P(\omega,\theta) = \frac{1}{4\pi\sigma c} \int_{-2\pi\sigma c}^{2\pi\sigma c} d\varepsilon \, \frac{\pi w^2}{4} \, I(\omega+\varepsilon,\theta) \tag{49a}$$

where

$$I(\omega+\varepsilon,\theta) = \sin^2\theta \left\{ \frac{8\pi^3 T T_1 T_2 (\omega+\varepsilon)^2 n}{c^3 n_1 n_2 [n^2+c^2\alpha^2/4(\omega+\varepsilon)^2]} \, |\chi^{(2)}_{24}|^2 I_1 I_2 \right\} \tag{49b}$$

$$\times \frac{|1-\exp(-\alpha\ell/2)\, \exp\{i[\Delta k(\omega,\theta)-B\varepsilon/c]\ell\}|^2}{[\Delta k(\omega,\theta)-B\varepsilon/c]^2 + \alpha^2/4}$$

is the intensity generated by two monochromatic lasers at their difference frequency $\omega+\varepsilon$; α is the far-infrared absorption coefficient at ω; $\Delta k(\omega,\theta)$ is the phase mismatch for the nominal laser frequency

and the difference frequency ω; B is given by either $B_- = n - n_1$ for FCPM or by $B_+ = n + n_1$ for BCPM; 2σ is the effective bandwidth of our dye lasers; I_1 and I_2 are the pump laser intensities; T, T_1, and T_2 and n, n_1, and n_2 are the far-infrared, high-frequency optical, and low-frequency optical transmission coefficients and refractive indices, respectively; and θ is the angle between the optical beams and the c-axis of the crystal.

B. Backwards Collinear Phase-matching

In crystals that have an optical birefringence sufficient to collinearly phase-match the difference frequency generation of a forward propagating far-infrared wave, there is also a range of frequencies in which the generation of a backward propagating or reflected difference frequency wave can be phasematched. This occurs because in the frequency range below the lowest infrared active TO phonon, the far-infrared refractive index is typically a monotonically increasing function of frequency and is usually greater than the optical refractive indices. This reflected difference frequency wave is similar to the reflected second harmonic wave generated in III-V semiconductors;[11] however, since it is phase-matchable, the coherence length can be a substantial fraction of the crystal thickness rather than just half a second harmonic wavelength.

If the forward, P_F, and the backward, P_B, collinearly phase matched powers are generated by identical pump laser beams in crystals that are identical except for their phase-matching angles, then according to Eq. (49) their ratio is the product of two factors:

1) the ratio of $\sin^2(\theta)$ at their respective phase matching angles, and 2) the ratio of the mean values of their phase-matching functions averaged over the far-infrared linewidth. The ratio of the backward to the forward collinearly phasematched $\sin^2\theta$ factors is $(n+n_1)/(n-n_1)$ when $\omega_1 \gg \omega$ and when dispersion at the pump laser frequencies can be neglected. When the far-infrared generation process is phase matched at line center ($\varepsilon=0$ in Eq. (49)), P_B/P_F, including the above ratio of the $\sin^2(\theta)$ factors, is given by:

$$P_B/P_F \equiv f[(n+n_1)\sigma]/f[(n-n_1)\sigma] \tag{50}$$

where

$$f(u) \equiv \int_{-2\pi u}^{2\pi u} \frac{dv}{4v^2+\alpha^2} \left|1-\exp[-(2iv+\alpha)\ell/2]\right|^2 .$$

Thus, BCPM is more efficient than FCPM for type II collinear generation of a far-infrared o-ray in $LiNbO_3$; in the limit of a large absorption coefficient, α, the power ratio is given by $P_B/P_F \cong (n+n_1)/(n-n_1)$ which can be as large as a factor of two in $LiNbO_3$.

C. Noncollinear Phase Matching

The most general phasematching configuration is non-collinear phasematching; the forward and backward collinear phasematching configurations are, in fact, limiting cases of non-collinear phasematching. The general phasematched three wave interaction is described by the wavevector triangle shown in Fig. 23a. For our difference-frequency case the index 1 and 2 waves are optical beams and the index 3 wave is the far-infrared beam. The special case $\phi = \psi = 0$ is forward collinear

phasematching with $\Delta k_{fc} = k_1 - k_2 - k_3 = 0$ while $\phi = 0$, $\psi = \pi$ is backward collinear phasematching with $\Delta k_{bc} = k_1 - k_2 + k_3 = 0$. By an elementary application of the law of cosines and half-angle formulas, we obtain for the angle between the two optical beams:

$$\sin^2(\frac{\phi}{2}) = - \frac{(k_1-k_2)^2 - k_3^2}{4k_1k_2} \quad , \tag{51}$$

and for the angle between the far-infrared beam and the high-frequency optical beam:

$$\sin^2(\frac{\psi}{2}) = \frac{1}{2} \left\{ 1 - \frac{n_2}{n_3} - \frac{(n_1-n_2)\omega_1}{n_3\omega_3} \right\} \left\{ \frac{n_1+n_2}{2n_1} - \frac{(n_3+n_2)\omega_3}{2n_1\omega_1} \right\} \quad . \tag{52}$$

For far-infrared generation with optical or near-infrared lasers, the angle ϕ is small because k_3 is much smaller than either k_1 or k_2. However, the angle ψ is often large.

Far-infrared generation with non-collinear phase matching is more sensitive to the divergence of the pump lasers than far-infrared generation with collinear phasematching whenever the angle, ϕ, between the pump beams is more than about twice their divergence angles. The far-infrared radiation is generated by the interaction of the various plane-wave components of the pump laser beams. Thus, for phase matched mixing of divergent pump laser beams, Fig. 23a illustrates the phase matched mixing of the axial plane wave components that are at the center of the far-field diffraction patterns of the pump laser beams, and Fig. 23b illustrates the mixing of this component of one

pump beam with a plane wave component at the edge of the main diffraction lobe of the second. The value, $\Delta k'$, of the phase mismatch for the case when $\Delta\vec{k}$ and $\vec{k}_3$ in Fig. 23b are collinear is a measure of the effect of the pump laser divergence angle δ; its magnitude is the value of $|\Delta\vec{k}|$ for the most nearly phase-matched plane-wave component of the far-infrared radiation in Fig. 23b, and it is given by:

$$\Delta k = \frac{u}{k_3 + \sqrt{(k_3^2 + u)}} \sim k_1 \delta \cdot \sin\psi \qquad (53)$$

where $u = 4k_1k_2 \sin(\delta/2) \sin(\phi + \delta/2)$ and the approximation in Eq. (53) is valid when $|\Delta k| \ll k_3$ and $\delta \ll 1$. In the collinear phasematching cases (ϕ=0), the range of the phase mismatch is of the order of δ^2 and thus a few milliradians of beam divergence can often be ignored. In the non-collinear case ($\phi > 2\delta$), the phase mismatch becomes significant more quickly because it grows linearly with δ.

III. Experimental Equipment and Techniques

A. Laser Systems

For many of the collinear and all of the noncollinear phase-matching experiments, a conceptually simple system of two separate dye lasers pumped by a single Q-switched ruby laser was used. The active medium was a solution of 3,3'-diethylthiatricarbocyanine iodide (DTTC iodide) in dimethyl sulfoxide (DMSO) contained in a 1 cm Beckman spectrophotometer cell. Each laser was arranged in Bradley's[12] nearly longitudinally pumped configuration with a 312 mm^{-1} blazed echelle

grating used in a sixth-order Littrow or back reflection geometry and a 70% reflectivity dielectric mirror to complete the laser cavity. The .5 J, 30 ns ruby pump pulse used in each dye laser generated about 24 mJ of dye laser energy that was continuously tunable from about 810 nm to greater than 840 nm.

With this pump pulse, the dye laser output was insensitive to factor-of-two changes in dye concentration from our operating concentration (20% low-level light transmission at 600 nm). Although the low-level light transmission at 6943 Å was less than 1%, the ruby laser saturated the dye absorption band since its energy burned black masking tape after passing through the dye cell. The only precautions taken with the dye solution were to cap the dye cell to keep moisture away from the hygroscopic DMSO solvent and to operate the laser in a darkened room to retard the degradation of the DTTC iodide by ambient light.[13] To obtain a reasonable power output, the incident ruby light was plane polarized parallel to the grating rulings to match the maximum dye laser gain[13] to the maximum reflectivity of our gratings.

Figure 24 describes a more novel dye laser that was used for some collinear phasematching experiments. A 1 J, 30 ns ruby pump pulse provided a large gain for both the orthogonal linear polarizations selected by the intracavity Glan-Thompson prism.[14] This prism makes possible the independent tuning and selection of a frequency for each polarization with two echelle gratings. To obtain good temporal overlap of and high power for the two frequency components, the net gains of the two arms of this dye laser were approximately equalized by

polarizing the ruby pump pulse either circularly or linearly at 45° to the transmitted polarization of the Glan-Thompson prism.[15] The glass microscope intracavity beam splitter provided fine tuning of the relative gains of the two polarizations. Under our operating conditions, the output polarizations for each beam had no more than 10% of their energy in the undesired orthogonal linear polarization.

An amplified Q-switched ruby laser pulse pumped the dye lasers. The oscillator consisted of a right angle prism Q-switch rotated at 400 sec^{-1} with a hysterisis-synchronous motor; a 4 inch long, 5/16 inch diameter ruby rod pumped by two water cooled linear flashlamps in a double ellipse cavity; and a glass resonant reflector with 25% reflectivity.[16] The amplifier was a 4 inch long, 3/8 inch diameter ruby rod pumped by the same configuration of flashlamps as the oscillator rod. Both ruby rods were water cooled from a common tank to equalize their operating temperatures and to decrease the necessary delay between successive shots. The oscillator and the amplifier rods were pumped simultaneously to simplify the trigger-circuit electronics. The oscillator was Q-switched about 400 μs after the peak of the flashlamp pulse which was about 800 μs long.

Since misaligning the amplifier rod increased the laser beam divergence and made its near field intensity asymmetric and non-uniform, the amplifier rod faces were aligned parallel to the oscillator resonant reflector and ruby rod faces; then, the oscillator and amplifier, which were less than four feet apart, operated as a coupled system. With new flashlamps, the oscillator and amplifier flashlamps discharged

550 J from a 360 μfd capacitor bank and 750 J from a 395 μfd capacitor bank, respectively. Amplifier flashlamp discharges of up to 1500 J were possible and up to 1100 J discharges were employed regularly. The oscillator flashlamp discharge energy was set to just below the threshold for multiple-pulses which was about 200 J above the threshold for lasing. Under these operating conditions, the ruby laser system generated about 1 J in a single 30 ns pulse.

B. Far-infrared Optics and Detection

To measure the far-infrared difference frequency signals generated in our experiments, we used an InSb Putley[17] detector between 20 and 95 cm^{-1} and a Ge:Ga[18] photoconductive detector between 95 and 180 cm^{-1}. The InSb detector was operated at 1.4°K in a 14.5 kG magnetic field. Both the low temperature and the magnetic field increased the responsivity and the signal-to-noise ratio of the detector-amplifier system by increasing the resistivity of the InSb sample. The magnetic field was also responsible for the high frequency end of this detector's response by tuning the InSb cyclotron resonance peak[19] to approximately 95 cm^{-1}. The rotary vacuum pump used to maintain the He temperature at 1.4°K was attached to the He dewar through a large reservoir to prevent modulation of the InSb detector's responsivity at the rotation speed of the pump. The Ge:Ga detector was operated at 4.2°K.

In our forward collinear and non-collinear phasematching experiments, the far-infrared radiation was collected by a 1 cm diameter evacuated light pipe beginning approximately .5 cm from the non-linear crystal. The radiation propagated along a straight section of light pipe,

reflected off the flat brass mirror of a 90° bend, and then propagated down another straight section of light pipe to the detector; the Ge:Ga detector had a condensing cone at the bottom of the light pipe to focus the radiation onto the detector surface. Three .25 mm thick sheets of black polyethylene were used to filter out unwanted radiation including that of the dye lasers; one of these sheets also served as the outer-most vacuum seal for the light pipe. No signal was observed when the non-linear crystal was removed and the dye lasers were fired directly into the light pipe.

Both detector systems including their polyethylene filters were calibrated against the flat response of a Golay cell[20] with a diamond window by conventional Fourier transform spectroscopy. A separate interferogram was taken with each of the 3 detector systems; the same mecury arc source, Michelson interferometer, and light pipe system were used for each interferogram. Each interferogram was digitally Fourier transformed and the frequency dependence of the responsivities of the Ge:Ga and InSb detectors were determined as the point-by-point quotient of that detector's spectrum to the spectrum measured by the Golay cell. Differences in the product, $A\Omega$, of the area and collection solid angle of the detectors were assumed not to effect their relative frequency response.

K. H. Yang[21] determined the absolute responsivity of the Ge:Ga detector at 125 cm^{-1}. He measured the response of both the Ge:Ga detector and the Golay cell to the mercury arc source through the Michelson interferometer at zero path difference;[22] the ratio of the

Ge:Ga to the Golay cell signal was 4.8×10^{-3}. From the responsivity curve[18] of the Ge:Ga detector, the amount of 125 cm^{-1} radiation that would generate the same response was calculated to be 2/3 of the radiation incident upon this detector from the mercury arc lamp. By correcting for this and the 3 times larger $A\Omega$ value of the Ge:Ga detector, we concluded that the ratio of the responsivity of the Ge:Ga detector at 125 cm^{-1} to that of the Golay cell was 2.4×10^{-3}. Since (according to its manual[20]) the responsivity of the Golay cell is 8.3×10^{5} V/Watt, the responsivity of the Ge:Ga detector is 2×10^{3} V/Watt.

K. H. Yang[21] also determined the noise equivalent power (NEP) of the Ge:Ga detector. He measured the electrical noise voltage of this detector at the 1.35 V bias voltage used in our experiments with a lock-in amplifier at several chopping frequencies at or above 280 Hz. Under his measuring conditions the contribution of the preamplifier of the lock-in amplifier to the observed noise signal was negligible. The 1.2×10^{-7} $V/\sqrt{Hz}$ noise thus measured gives a NEP of 6×10^{-11} $W/\sqrt{Hz}$ or 4.24×10^{-8} Watts within the 500 kHz bandwidth of the detection system. The noise level of the operational amplifier with the detector replaced by its equivalent room-temperature resistor was .3 mV peak-to-peak compared to the 2 mV noise level of the combined detector-amplifier system. Thus, the detector-amplifier system was detector noise limited and the observed signal-to-noise ratio is relative to this detector NEP.

Based on the above NEP value, the observed signal-to-noise ratio of 66 (relative to the .7 mV rms noise) implies that about 4.9 mW of far-infrared power was generated at 125 cm^{-1} in our FCPM experiment in

$LiNbO_3$. To arrive at this number three corrections had to be made: First, the .75 mm black polyethylene filter used in the experiment, but not in the detector calibration, attenuates the 125 cm^{-1} radiation by a factor of 8.65. Second, a factor of 3 attenuation due to the light pipe was experimentally measured. Finally, since the 30 ns far-infrared pulse generates an impulse response in the detector, the detector averages the pulse energy over its 2 μs response time to record a signal corresponding to 30/2000 or 1/67 times the peak far-infrared power.

C. Sum-Frequency Normalization

Because of the low repetition rate of a ruby laser system, we resorted to sum-frequency normalization to reduce the shot-to-shot fluctuations in our measurements. In the collinear experiments, a fraction of the combined two-frequency laser beam was split off with a glass microscope slide and directed onto a polished (110) surface of a GaAs or InAs crystal. Since both SFG and DFG are second order processes, the effects of power fluctuations and temporal overlap fluctuations are eliminated by this scheme. However, even with identical field distributions, the fluctuations in spatial overlap are not completely eliminated by this scheme as the long wavelength of the difference-frequency signal causes the fields from neighboring hot-spots to interfere due to the large diffraction angle from each hot-spot as was discussed in chapter II. In the collinear experiments using two separate dye lasers, we located the sum and difference frequency crystals equal distances from the sum-frequency beam-splitter.

Since the latter followed all the beam combining and focusing optics in our system, each of the two fields at one crystal was proportional (as nearly as possible) to the corresponding field at the other crystal. Thus, for this group of experiments, spatial overlap fluctuations will be reduced for hot-spots that are large compared to the far-infrared wavelength.

Discrimination of sum-frequency signals against second harmonic signals was achieved with Armstrong's scheme[23] by making use of the $\bar{4}3m$ crystal symmetry in which χ_{ijk} vanishes if i,j,k is not a permutation of 1,2,3. Linearly polarizing one laser parallel to the [001] direction eliminated its second harmonic signal. The second laser was polarized perpendicular to the [001] direction; thus, its second harmonic was plane-polarized along the [001] direction and was eliminated by a linear polarizer between the crystal and the photomultiplier. The [001] direction was made normal to the plane of incidence of the two laser beams to ensure that the above polarization directions were maintained inside as well as outside the crystal.

Since we measured the frequency dependence of the far-infrared power, we needed a sum-frequency normalization that did not vary with the difference frequency, ω, except through the product of the pump laser intensities. The novel use of SFG by reflection from a highly absorbing crystal eliminated one source of variation with ω; the highly damped solution has no Maker fringes to make the sum-frequency signal a rapidly varying function of the input laser frequencies as the large phase mismatch of the reflection geometry is nearly constant

over the fractionally small tuning ranges used in far-infrared DFG experiments. Phase matching could also be used to eliminate the effect of Maker fringes, but it is impractical for our experiments because it requires a tedious adjustment of the orientation of the sum-frequency crystal each time the frequency of either dye laser is changed. Other experimenters have used sum-frequency generation by transmission through a transparent crystal with a ground exit surface[24,25] for this purpose; we could have used this technique with a crystal like KDP, but the collection of the output sum-frequency signal would have been complicated by its poor colimation. Fortunately, the much larger sum-frequency susceptibilities of GaAs and InAs compared to those of readily available transparent crystals compensates for the much shorter coherence length of the reflected wave geometry. Because the 12,000 to 12,200 cm^{-1} frequency range that our dye lasers were tuned through in these experiments is small compared to the separation between the dye laser frequencies and band gap frequencies of GaAs (~10900 cm^{-1}) and InAs (~2130 cm^{-1}), the sum-frequency susceptibility of our normalization crystal was nearly independent of the difference frequency ω; together with the lack of Maker fringes, this made the sum-frequency signal a good normalization against the frequency dependence of the dye laser power.

IV. Forward Collinear Phase-matching Experiments

A. Experimental Measurements and Data Analysis for $LiNbO_3$

Since the experimental data available in the literature on the o-ray absorption coefficient of $LiNbO_3$ between 70 and 1000 cm^{-1} is based on a Kramers-Kronig analysis of far-infrared reflectivity data[26] rather than a direct measurement and since sample-to-sample differences are possible due to impurities or slightly non-stoichiometric composition, we determined it at each frequency by measuring the far-infrared power as a function of wavevector mismatch. DeMartini has used this technique, known as momentum spectroscopy,[24,27] to measure the far-infrared absorption coefficient and the difference-frequency susceptibility of GaP.[24,25] However, we have used the birefringence of $LiNbO_3$ to vary the momentum or phase mismatch while De Martini used the noncollinearity of the pump beams and the various plane wave components of his far-infrared radiation in the optically isotropic GaP crystal.

We used seven $LiNbO_3$ slabs cut from a single Crystal Technology, Inc. boule with angles between the c-axis and the slab normal of 15°, 25°, 35°, 45°, 55°, 65°, and 90° (the a-axis, c-axis, and slab normal were coplanar). This permitted the frequency range 20 to 127 cm^{-1} to be spanned without the complications of angles of incidence over 20°. The surfaces were ground flat on a series of SiC abrasive papers and optically polished with 1 μ diamond abrasive. For our experimental measurements these $LiNbO_3$ slabs were mounted on the axis of a rotating platform with their c-axes, their slab normals, and the laser beam

direction all perpendicular to the axis of rotation. At each frequency, ω, above 40 cm^{-1} we measured the power as a function of the orientation of the crystal, $P(\omega,\theta)$, over a wide enough range of θ to determine its angular width and thus its absorption coefficient, $\alpha(\omega)$.

To obtain the far-infrared absorption coefficient $\alpha(\omega)$ from a set of experimental measurements, $\{(P_i,\theta_i/i=1,2,...,m\}$, we used a nonlinear least-squares fit. To make the computation tractable on a small computer, we neglected the ε-dependence of the term of Eq. (49b) that is enclosed in braces and eliminated the terms that contain $\exp(-\alpha\ell/2)$; since $\alpha\ell \gg 2$ at the frequencies at which we determined α, the latter approximation is valid in our experiments. We also replaced $\Delta k(\omega,\theta)$ with $2\pi[\Delta_o + \Delta(\theta)]$ where $2\pi\Delta(\theta)$ is the phase mismatch at the difference frequency ω and at the nominal laser frequency, θ is the angle between the laser beam axis and the c-axis, and Δ_0 accounts for the experimental uncertainties in the values of the nominal laser frequency and the angles θ_i. With these assumptions $P(\omega,\theta)$ from Eq. (49) is given by

$$P(\omega,\theta,\vec{a}) = \frac{A \sin^2\theta}{2B\sigma\sqrt{\Gamma}} \left\{\tan^{-1}\left(\frac{\Delta_0+\Delta(\theta)+B\sigma}{\sqrt{\Gamma}}\right) - \tan^{-1}\left(\frac{\Delta_0+\Delta(\theta)-B\sigma}{\sqrt{\Gamma}}\right)\right\} \qquad (54)$$

with $\Gamma = \alpha^2/16\pi^2$ and $\vec{a} \equiv (A,\Delta_0,\Gamma)$. We minimized the function $\chi^2(A,\Delta_0,\Gamma) = \sum_{i=1}^{m} [P_i - P(\omega,\theta_i)]^2/(m-3)$ with respect to A, Δ_o, and Γ by the minimization process discussed in Appendix E.

As we can see from Eqs. (49) or (54), determination of α from our data requires that the effective bandwidth, 2σ, of our dye lasers be measured. From Eq. (54) we can also see that, for a long crystal

($\alpha\ell \gg 2$), σ is determined by measuring $P(\omega,\theta)$ at a frequency where α (and hence Γ) is known. For any value of α, the minimum value of σ that can be determined from the angular width of $P(\omega,\theta)$ is proportional to $\alpha/4\pi B$ since Eq. (54) is nearly independent of σ when both $\tan^{-1}$ functions can be approximated by their arguments. For a crystal less than two absorption lengths thick, the finite thickness makes the width of $P(\omega,\theta)$ even less sensitive to σ as can be seen from Fig. 25.

To measure the effective bandwidth or our dye lasers, we used a 1.61 mm thick $LiNbO_3$ sample that was cut from a Hansen Microwave Lab. boule with its slab normal at 16° to the c-axis. At a far-infrared frequency of 21 cm^{-1}, effective dye laser bandwidths smaller than about .8 cm^{-1} could not be measured even with a crystal many absorption lengths thick. However, since our sample was less than two absorption lengths thick (α = 9.5 cm^{-1}),[28] the smallest measurable bandwidth was about 1.5 cm^{-1} as can be seen from Fig. 25; this sensitivity to relatively narrow bandwidths is due primarily to the large difference (4.4) between the optical and far-infrared o-ray refractive indices. The results of our experimental measurement are shown in Fig. 26; they correspond to a 3 cm^{-1} bandwidth for our far-infrared radiation.

B. Results of Forward Collinear Phase-matching Experiments

The results of our measurements of the o-ray absorption coefficient, α_o, in $LiNbO_3$ are summarized in Fig. 27. The solid curve is a composite of Bosomworth's[28] far-infrared transmission measurements for $\omega \leqslant 70$ cm^{-1} and Barker and Laudon's[26] Kramers-Kroenig analysis of their far-infrared reflectivity data for $\omega > 70$ cm^{-1}. Our results agree satisfactorily

with those of Barker and Loudon between 80 and 110 cm^{-1}. Between 40 and 70 cm^{-1} our values of α_o are significantly larger than the values of Bosomworth. The difference is due to a weak, broad absorption peak centered near 65 cm^{-1} that may be due to two phonon absorption.[29] Bosomworth's data also suggests the presense of a peak near 65 cm^{-1}, but his peak is much weaker than ours; perhaps this is just sample variation between his slightly greenish $LiNbO_3$ crystal and our colorless sample.

Figure 28 contains a comparison of our FCPM experimental results for $LiNbO_3$ (the circles) and the plane wave theory of Eq. (49) with the absolute power at 110 cm^{-1} treated as an adjustable parameter. Above 40 cm^{-1} this theory[30] reproduces our experimental results satisfactorily given the multi-mode nature of our dye laser beams. However, the theoretical absolute power at 125 cm^{-1} is 22.5 mW, a factor of 4.6 larger than our measured power. Below 40 cm^{-1} the observed power falls off far more rapidly with decreasing frequency than is predicted by Eq. (49).

The calculations shown in Figs. 29a and 29b strongly suggest that this reduction in the DFG efficiency below 40 cm^{-1} is due to the multi-mode nature of our laser beams and the inherent misalignment of their hot-spots. These calculations used the more complete theory of Chapter II for single mode dye laser beams; for Fig. 29a the two dye laser beams were coaxial (a=0), but for Fig. 29b their axes were 0.5 mm apart. The other parameters roughly approximate our laser beams and our $LiNbO_3$ crystal: 300 kW in each dye laser beam, λ_1 = 833 nm, w = .08 mm, z_o = 50 cm (2 mr divergence half-angle at half intensity and 3.3 mm

$1/e^2$ diameter at the crystal), ℓ = .65 mm, $\chi^{(2)} = 3.18\times10^{-6} \sin\theta_M$ where θ_M is the phase-matching angle, $n_0 = 2.257$, $n_o - n_{em} = .08192$, a cubic spline fit to the absorption coefficients in Table II, a 30° detector collection half-angle, and an axially phase-matched DFG interaction. The far-infrared radiation generated below 20 cm^{-1} is reduced by more than a factor of 10 by the 0.5 mm separation of the laser beam axes.

At a sufficient distance, z_o, from the focal plane, optical pump beams separated by many focal plane radii diffract into each other and form a Gaussian nonlinear polarization centered at the midpoint between the two beam axes. Since geometric optics adequately describes the pump laser beams at such a distance from the focal plane, at the midpoint between the axes the Pointing vectors of the two laser beams, which give the direction of the local wavevectors, lie in the plane of the laser beam axes at equal, but opposite, angles $\pm a/2z_o$ to them. Thus, inside the crystal the difference-frequency radiation is generated preferentially about a direction at an angle $\sin^{-1}(k_1 a/k_3 z_o)$ to the laser beam axes where k_1 and k_3 are the optical and far-infrared wavevectors in the crystal, respectively. For the calculation of Fig. 29b this angle passes through the total reflection angle at 24 cm^{-1}; thus, only above the far-infrared frequency $\omega = ck_1 a/z_o$, is the far-infrared power improved significantly by placing the crystal for enough away from the focal plane that the hot-spots diffract into one another (as in our experiment).

We have also extracted a rough measurement of the frequency dependence of $|\chi^{(2)}_{24}|^2$ from our data. The results are shown in Fig. 30 together with a multiple simple-harmonic-oscillator calculation[31,32] of $|\chi^{(2)}_{24}|^2$ in

which we used the oscillator strengths, TO phonon frequencies, and linewidths of Barker and Loudon[26] and the Raman cross sections of Kaminow and Johnston.[33] The agreement is satisfactory. Furthermore, the monotonically increasing $|\chi_{24}^{(2)}|^2$ without a broad dip between 80 and 90 cm^{-1} indicates that the 152 cm^{-1} E-symmetry mode contribution to the low frequency (say 1 to 10 cm^{-1}) $\chi_{24}^{(2)}$ has the same sign as the sum of the contributions from the electronic and the remaining E-symmetry vibrational modes.

Table I summarizes the far-infrared power generated in 1 mm thick samples of ZnO, ZnS, CdS and CdSe at their maximum phase-matchable frequencies (all samples had their c-axes parallel to the sample surfaces). The ZnO and CdS samples were pre-cut and rough-ground by the manufacturers; the two CdSe slabs were cleaved from bulk samples and rough-ground on successively finer grades of SiC paper. The final optical polishing of all these relatively soft samples was accomplished by hand lapping in a water slurry of 1 μ Al_2O_3 abrasive. The ZnS sample was a long 1 mm wide strip that was optically polished by the manufacturer; this sample was not wide enough to accept all of the dye laser beam output, so the number reported in Table I has been corrected to estimate the output attainable with a crystal wider than the laser beams.

V. Backward Collinear Phase-matching Experiments in $LiNbO_3$

A. Modifications of FCPM Experimental Apparatus for BCPM

We have observed the phasematched difference frequency generation of a reflected far-infrared wave in $LiNbO_3$. In spite of the 54% far-infrared o-ray reflectivity, above 40 cm^{-1} the laser input surface cannot be used as a mirror to reflect the far-infrared wave into a detector behind the crystal because the absorption coefficient is too large. To collect the radiation from the laser input side of the crystal, we added a short piece of brass light pipe and a right angle bend to the far-infrared collection optics used for the forward collinear phasematching experiments. The dye laser beams passed through a 1/8 in diameter hole milled through the flat brass reflector of the right angle bend; the axis of the hole was parallel to the laser beams and at a 45° angle to the normal of the brass plate. This collection technique added about 5 cm of air to the far-infrared propagation path.

B. Results of BCPM Experiment

As is shown in Fig. 28, our BCPM data do not agree with the simple theory of Eq. (49) since the predicted dip near 65 cm^{-1} in Fig. 28 was not observed in our experiment. We believe that this difference is due to the frequency dependent losses through the 1/8 in diameter hole in the brass light pipe. As the far-infrared frequency increases, the far-infrared beam becomes more collimated around its nominal reflected direction; and when phase matching occurs near normal incidence, more far-infrared energy can escape through the hole at high difference

frequencies that at low ones. The added 5 cm of air in the propagation path will also modify the frequency dependence of the far-infrared signal due to water vapor absorption. The net result is extremely difficult to calculate and we will not attempt to do so.

VI. Noncollinear Phase-matching Experiments in $LiNbO_3$

A. Experimental Methods

The experimental set-up is shown in Fig. 31. Two separate dye lasers were used; they were synchronized by pumping them with a single ruby laser pulse. The plane of incidence of the dye lasers on the $LiNbO_3$ sample was horizontal for experimental convenience. To maximize the far-infrared radiation generated, the non-linear polarization vector and far-infrared wavevector were made orthogonal by using vertically polarized dye lasers. The angle between the two dye laser beams was adjusted by rotating the right angle prism PM1 and the intersection of the two beams was positioned at the input surface of the $LiNbO_3$ crystal by moving this prism on a translation stage. The two dye laser beams were separately focused a few cm behind the $LiNbO_3$ crystal. Sum frequency normalization was accomplished as shown in Fig. 31. Since the dye laser field configurations at the sum and difference frequency crystals were not similar, the sum frequency signal compensates for the power and temporal overlap fluctuations of the dye lasers but cannot be guaranteed to compensate for spatial overlap fluctuations even at high difference frequencies.

Figure 32 is a top view of the single 4 mm cube $LiNbO_3$ crystal used in our NCPM experiments. ($LiNbO_3$ was chosen for this experiment

because of its large electro-optic coefficient and its availability.) In the shaded region, the nearly parallel dye laser beams create a difference-frequency polarization that radiates along the direction of the difference of the two optical wavevectors. To permit the far-infrared radiation to leave the crystal with an acceptible reflection loss, we cut off the corner of our $LiNbO_3$ cube at an angle corresponding to $\psi_0 = 68°$ so that the far-infrared radiation would be within 4° of normal incidence inside the crystal over the frequency range 1 to 150 cm^{-1}; at 160 cm^{-1} the angle of incidence was approximately 5°.

We chose our experimental geometry with all three electric fields polarized along the c-axis of our $LiNbO_3$ sample for three reasons: First, χ_{33} and χ_{24} are an order of magnitude larger than the other non-zero difference-frequency susceptibility tensor elements. Second, χ_{24} yields a far-infrared o-ray while χ_{33} yields an e-ray. The latter has a smaller absorption coefficient than the former; thus, the χ_{33} configuration is a more efficient far-infrared source. Finally, as can be seen from Eq. (52) when $n_1 = n_2$ and n_3 is approximately constant, as in the χ_{33} configuration, the angle ψ between the far-infrared and optical wavevectors is nearly independent of ω_3, and a single sample of $LiNbO_3$ with its corner cut off at a nominal value of ψ_o can be used at all frequencies of interest. If ψ varied significantly with ω_3, multiple samples would have to be used to avoid large losses due to total internal reflection.

B. Results of Noncollinear Phase-matching Experiments

To analyze our results, we have made use of the simple approximation of a plane wave far-infrared field that propagates perpendicular to the cut off surface of the cube. Since the 4 mrad divergence of the pump laser beams creates a 140 cm^{-1} range of Δk values, we averaged the plane wave power over this range using a uniform weight at each Δk. We actually used the plane wave formula for collinear phase matching with an effective length, ℓ_{eff}, that is roughly the shortest distance along the far-infrared beam between points at which the phases of the nonlinear polarization are uncorrelated. A value of ℓ_{eff} = .05 cm gave a good fit to our data at 40 and 55 cm^{-1}; at and above 75 cm^{-1} the calculated values are independent of ℓ_{eff} due to the large absorption coefficient. This simple analysis fits our data amazingly well as can be seen in Fig. 28. The justification for treating the pumped region as a thin slab is that the coherence length of ~.05 cm is much shorter than our beam diameter of ~.3 cm so the exact shape of the non-linear polarization region becomes unimportant as the slab like first few coherence lengths dominate. For the case of coherent pump lasers, a more general plane-wave analysis that considers the shape of the pumped region has been given by Lax and Aggarwal[7] in their work using a non-collinear phase matching geometry.

VII. Discussion of Results and Conclusions

A. Comparison with Raman Scattering Results

Our experimentally derived ratios of the nonlinear difference frequency generation susceptibilities of $LiNbO_3$, ZnO, and CdS at their

respective maximum phase matching frequencies are within 20% of independently computed values. The ratios obtained from our far-infrared power measurements are $d_{24}(LiNbO_3):d_{15}(ZnO):d_{15}(CdS) = 1 : 9.1\times10^{-3}:5.2\times10^{-2}$. Based on reported values of optical refractive indices,[34-36] far-infrared reflectivities,[26,37,38] Raman scattering cross sections[33,39,40] of all three crystals and based on the clamped linear electro-optic coefficient r_{42} of $LiNbO_3$,[41] the computed[32] ratios are $1 : 1.0\times10^{-2}$: 6.3×10^{-2}. Such close agreement is remarkable for far-infrared difference frequency generation experiments.

Figure 33 displays the dispersion of the ionic, r_q, and electronic, r_e, contributions to r_{51} for CdS at 80°K based on the Raman scattering data of Ralston et al.[40] and on Loudon's theory.[42] Because the Raman scattering cross sections are proportional to the square of matrix elements while r_e and r_q are linear functions of the same matrix elements, there are four simultaneous solutions for r_e and r_q in-terms-of the LO and TO phonon Raman scattering cross sections; but one pair of these solutions differs from the other pair by only a sign. The magnitude of r_q is determined by the TO phonon Raman cross section; however, there are still two possible magnitudes of r_e which are shown in Fig. 33 for CdS. Our far-infrared measurements require that r_e is given by the upper curve so that, for example, $r_{51} = r_e + r_q = 8.7\times10^{-8}$ esu at 1.064 μ. For ZnO at 5145Å, r_q is 2.04×10^{-8} esu and r_e is $.546\times10^{-8}$ (or 3.35×10^{-8}) esu based on the Raman data of Arguello et al.[39] and the refractive indices of Bond.[35] At 6471Å, r_q is 1.69×10^{-8} esu and r_e is $.97\times10^{-8}$ (or 2.27×10^{-8}) esu based on the Raman data of Callender et al.[43]

Our far-infrared power measurements imply that the smaller value of r_e is appropriate so that $r_{42} = 2.59\times10^{-8}$ esu at 5145Å. Fortunately, for this choice of r_e the linear combination of r_e and r_q that determines the DFG susceptibility changes by only 2% between 5145 and 6471Å; thus, we can use this shorter wavelength data to estimate the DFG susceptibility at our dye laser wavelengths (8100 to 8400Å).

B. Relative Merits of Forward-, Backward-, and Non-Collinear Phase Matching

Since BCPM occurs at a larger angle θ than FCPM, DFG of a far-infrared o-ray in crystals of the point groups 4, $\bar{4}$, 4mm, $\bar{4}$2m, 3m (when $\sin3\phi = 0$), and 6mm has a larger effective nonlinear susceptibility, d_{eff}, for BCPM than for FCPM, as can be seen in Table III. For o-ray generation in 32, $\bar{6}$, and $\bar{6}$m2 crystals and e-ray generation in 3m, $\bar{6}$, and $\bar{6}$m2 crystals d_{eff} is smaller for BCPM than for FCPM. For the other combinations of the optically uniaxial point groups and the generated polarization in Table III, the size of d_{eff} for BCPM relative to d_{eff} for FCPM at the same difference frequency depends on the nonlinear susceptibility tensor elements of the particular crystal and the angle ϕ at which it was cut, or it depends on the difference frequency through the factor $\cos\theta \sin\theta$ (e.g., e-ray generation in 4, $\bar{4}$, 422, $\bar{4}$2m, 6, and 622 crystals). However, collecting the far-infrared radiation is more difficult in a BCPM than in a FCPM configuration; thus, even when it has a larger d_{eff}, BCPM will probably be less useful than FCPM in any far-infrared source based on difference frequency generation.

Noncollinear phase matching offers three practical advantages over collinear phase matching. First, it adds cubic crystals in point groups $\bar{4}3m$ and 32 to the list of phase matchable materials. Second, a single crystal sample can be used to cover a frequency range that would require several separately cut samples for collinear phase matching. And third, in some crystals, such as $LiNbO_3$, it provides a more efficient far-infrared source by eliminating the angular dependence of d_{eff}, using a larger nonlinear susceptibility tensor element than collinear phase matching, or using the far-infrared polarization with the smaller absorption coefficient. Nevertheless, in the final analysis each crystal must be evaluated independently to determine the best phase matching configuration for it.

C. Difference Frequency Generation as a Far-infrared Source

We have also verified that the dual-frequency dye laser system shown in Fig. 24 can be operated with a flashlamp-pumped Rhodamine 6G dye laser, although the laser output was insufficient to generate detectable far-infrared radiation in the difference frequency experiment. However, a flashlamp-pumped dye laser with 100 kW peak power (50 kW at each frequency) and a 1 μsec pulsewidth would generate the same far-infrared signal for each pulse as our Ruby laser-pumped system with its 600 kW peak power and 30 nsec pulsewidth. Because flashlamp-pumped dye lasers with 100 kW peak power can be operated at repetition rates above 1 Hz and beam expanding telescopes can be used to narrow the linewidth, difference frequency generation using the dual-frequency dye laser system of Fig. 24 is an attractive source for far-infrared

spectroscopy. With the same conversion efficiency as in our experiment, the system would generate a few nanoWatts of time-average far-infrared power at a 1 Hz repetition rate.

There are at least two opportunities for significant research in developing difference frequency generation as a far-infrared source: (1) a search for new and better nonlinear crystals with larger linear electro-optic coefficients, lower far-infrared absorption coefficients, and high damage thresholds; (2) an experiment with a less than 1 cm^{-1} linewidth TEM_{oo} mode laser to verify the theory of Chapter II and establish the maximum attainable optical to far-infrared conversion efficiency as a function of input power for each crystal.

Table I. Summary of the mixing experiments on five different crystals.

Crystals	Tunable range	Power (Frequency observed)
$LiNbO_3$	20 to 127 cm^{-1} (FCPM)	See Fig. 28
	20 to 95 cm^{-1} (BCPM)	≈ twice that of FCPM
	40 to 160 cm^{-1} (NCPM)	See Fig. 28
ZnO*	≤ 190 cm^{-1} (FCPM)	14 mW (190 cm^{-1})
CdS*	≤ 180 cm^{-1} (FCPM)	3 mW (180 cm^{-1})
ZnS*	≤ 91 cm^{-1} (FCPM)	0.74 mW (91 cm^{-1})
CdSe*	≤ 150 cm^{-1} (FCPM)	< 0.15 mW† (150 cm^{-1})

*Crystal thickness 1 mm

†Less than the detector noise level

Table II. Absorption Coefficients of $LiNbO_3$ (used for calculations in Chapter IV)

Frequency	o-ray	Source	e-ray	Source
0	0		0	
5	.50	a	.31	a
10	2.1	a	1.25	a
15	5.54	a	2.8	a
20	8.68	a	5.0	a
25	12.5	a	7.5	a
30	17.1		11.	a
35	49.6		13.	a
40	110.	b	18.	a
45	150.		23.	a
50	200.		30.	a
55	230.	b	39.	a
60	300.	b	50.	a
65	425.	b	70.	a
70	460.		100.	a
75	480.	b	130.	a
80	500.		175.	a
85	520.		230.	a
90	530.		260.	
95	545.	b	288.	
100	610.		319.	
105	720.		352.	
110	845.	b	386.	
120			610.	
125	1500.	c		
140			1047.	c
160			1510.	c

a) D. R. Bosomworth, ref. 28
b) our nonlinear measurements
c) Barker and Loudon, ref. 26

Table III. Angular Dependence[a] of Second-Order Nonlinear Susceptibilities for Type II Collinear Phase Matching in Uniaxial Crystals.

(a) Ordinary-Ray Generation

Symmetry group	Effective nonlinear susceptibility[b,c]
4	$d_{15}\sin\theta$
$\bar{4}$	$(d_{14}\sin 2\phi - d_{15}\cos 2\phi)\sin\theta$
422	0
4mm	$d_{15}\sin\theta$
$\bar{4}$2m	$d_{14}\sin 2\phi \sin\theta$
3	$-(d_{11}\cos 3\phi + d_{22}\sin 3\phi)\cos\theta + d_{24}\sin\theta$
32	$-d_{11}\cos 3\phi \cos\theta$
3m	$-d_{22}\sin 3\phi \cos\theta + d_{24}\sin\theta$
6	$d_{24}\sin\theta$
6mm	$d_{24}\sin\theta$
622	0
$\bar{6}$	$-(d_{11}\cos 3\phi + d_{22}\sin 3\phi)\cos\theta$
$\bar{6}$m2	$-d_{22}\sin 3\phi \cos\theta$

Table III. Continued.

(b) Extraordinary-Ray Generation

Symmetry group	Effective nonlinear susceptibility[b,c]
4	$d_{14}\sin\theta\cos\theta$
$\bar{4}$	$[(d_{14}+d_{36})\cos2\phi + (d_{15}+d_{31})\sin2\phi]\sin\theta\cos\theta$
422	$d_{14}\sin\theta\cos\theta$
4mm	0
$\bar{4}$2m	$(d_{14}+d_{36})\cos2\phi\sin\theta\cos\theta$
3	$(d_{11}\sin3\phi - d_{22}\cos3\phi)\cos^2(\theta) + d_{14}\sin\theta\cos\theta$
32	$d_{11}\sin3\phi\cos^2(\theta) + d_{14}\sin\theta\cos\theta$
3m	$-d_{22}\cos3\phi\cos^2(\theta)$
6	$d_{14}\sin\theta\cos\theta$
6mm	0
622	$d_{14}\sin\theta\cos\theta$
$\bar{6}$	$(d_{11}\sin3\phi - d_{22}\cos3\phi)\cos^2(\theta)$
$\bar{6}$m2	$-d_{22}\cos3\phi\cos^2(\theta)$

a) All walk-off angles have been neglected.
b) θ is the angle between the normal, $\hat{n}$, and the axis of symmetry, $\hat{3}$.
c) ϕ is the angle between $\hat{2}$ and $\hat{n}\times\hat{3}$.

REFERENCES

1. D. W. Faries, K. A. Gehring, P. L. Richards, and Y. R. Shen, Phys. Rev. 180, 363 (1969).

2. V. T. Nguyen and C. K. N. Patel, Phys. Rev. Lett. 22, 463 (1969).

3. D. W. Faries, P. L. Richards, Y. R. Shen, and K. H. Yang, Phys. Rev. A 3, 2148 (1971).

4. G. D. Boyd, T. J. Bridges, C. K. N. Patel, and E. Buehler, Appl. Phys. Lett. 21, 553 (1972).

5. D. H. Auston, A. M. Glass, and P. Le Fur, Appl. Phys. Lett. 23, 47 (1973).

6. T. J. Bridges and V. T. Nguyen, Appl. Phys. Lett. 23, 107 (1973); V. T. Nguyen and T. J. Bridges, in International Conference on Submillimeter Waves and their Applications, Atlanta, 1974, Conference Digest, p. 41.

7. B. Lax, R. L. Aggarwal, and G. Favrot, Appl. Phys. Lett. 23, 679 (1973).

8. R. L. Aggarwal, N. Lee, and B. Lax, in International Conference on Submillimeter Waves and their Applications, Atlanta, 1974, Conference Digest, pp. 19-20.

9. D. E. Thompson and P. D. Coleman, in International Conference on Submillimeter Waves and their Applications, Atlanta, 1974, Conference Digest, pp. 24-25.

10. K. H. Yang, J. R. Morris, P. L. Richards, and Y. R. Shen, Bull. Am. Phys. Soc. series 2, 18, 350 (1973); Appl. Phys. Lett. 23, 669 (1973).

11. See, for example, D. Bethume, A. Schmidt, and Y. R. Shen, Phys. Rev. B 11, 3867 (1975).

12. D. J. Bradley, G. M. Gale, M. Moore, and P. D. Smith, Phys. Lett. A 26, 378 (1968).

13. P. P. Sorokin, J. R. Lankard, E. C. Hammond, and V. L. Moruzzi, IBM J. Res. Dev. 11, 130 (1967).

14. H. S. Pillof, Appl. Phys. Lett. 21, 15 (1972) has described a similar, independently developed system.

15. P. P. Sorokin et al. (ref. 2) have reported and we have also observed that longitudinally pumped DTTC iodide lasers lase with a linear polarization parallel to the linear polarization of a ruby pump laser.

16. D. Faries, Ph.D. dissertation, 1969, Phys. Dept. University of California, Berkeley, (unpublished).

17. E. H. Putley and D. H. Martin, in Spectroscopic Techniques, D. H. Martin ed., (North-Holland, Amsterdam, 1967) p. 133.

18. W. J. Moore and H. Shenker, Infrared Physics 5, 99 (1965).

19. M. A. C. S. Brown and M. F. Kimmett, Brit. Comm. Electron. 10, 608 (1963); Infrared Physics 5, 93 (1965).

20. SP. 50 Golay pneumatic cell from Pye Unican, Ltd., England.

21. K. H. Yang, Ph.D. Dissertation, 1974, Physics Dept. University of California, Berkeley (unpublished).

22. During this absolute calibration both detectors were used without black polyethylene filters, the Golay cell was connected to the output light pipe of the Michelson interfereometer with a length

of light pipe to match the experimental collection optics of the Ge:Ga detector (except the focusing cone), and the Ge:Ga detector output was fed directly into a lock-in amplifier instead of through the operational amplifier that we used for our difference-frequency measurements. Both detectors were operating significantly above their respective noise levels.

23. J. A. Armstrong, Appl. Phys. Lett. 9, 72 (1966).

24. F. De Martini, Phys. Lett. A 30, 319 (1969).

25. F. De Martini, Phys. Rev. B 4, 4556 (1971).

26. A. S. Barker, Jr. and R. Loudon, Phys. Rev. 158, 433 (1967).

27. J. P. Coffinet and F. De Martini, Phys. Rev. Lett. 22, 60 (1969).

28. D. R. Bosomworth, Appl. Phys. Lett. 9, 330 (1966).

29. S. Ushioda and J. D. McMullen, Solid State Commun. 11, 299 (1972).

30. To obtain this curve we used the TO phonon oscillator strengths, frequencies, and linewidths of Barker and Loudon (ref. 26) and the Raman cross sections of Kaminow and Johnston (ref. 33) to compute $|\chi_{24}^{(2)}|^2$ (see refs. 31 and 32); the far-infrared refractive indices of Bosomworth (ref. 28) and of Barker and Loudon (ref. 26); and our experimental values of the far-infrared o-ray absorption coefficient.

31. S. Sussman, Microwave Lab. Rept. 1851, Stanford Univ,, 1970.

32. A. S. Barker, Jr. and R. Loudon, Rev. Mod. Phys. 44, 18 (1972).

33. I. P. Kaminow and W. D. Johnston, Jr., Phys. Rev. 160, 519 (1967); 178, 1528(E) (1969).

34. G. D. Boyd, R. C. Miller, K. Nassau, W. L. Bond, and A. Savage, Appl. Phys. Lett. 5, 234 (1964).

35. W. L. Bond, J. Appl. Phys. 36, 1674 (1965).

36. T. M. Bieniewski and S. J. Czyak, J. Opt. Soc. Am. 53, 496 (1963).

37. R. J. Collins and D. A. Kleinman, J. Phys. Chem. Solids 11, 190 (1959).

38. H. W. Verleur and A. S. Barker, Jr., Phys. Rev. 155, 750 (1967).

39. C. A. Arguello, D. L. Rousseau, and S. P. S. Porto, Phys. Rev. 181, 1351 (1969).

40. J. M. Ralston, R. L. Wadsack, and R. K. Chang, Phys. Rev. Lett. 25, 814 (1970).

41. Landolt-Boernstein New Series, K.-H. Hellwege, ed., III/2, (Springer-Verlag, Berlin, 1969) p. 144. Also, A. Yariv, Quantum Electronics, second edition, (Wiley, New York, 1975) p. 333.

42. R. Loudon, Adv. Phys. 13, 423 (1964).

43. R. H. Callender, S. S. Sussman, M. Selders, and R. K. Chang, Phys. Rev. B 7, 3788 (1973).

ACKNOWLEDGEMENTS

I would like to thank my thesis advisor, Professor Y. R. Shen, for his expert guidance of this research and for his encouragement, especially at discouraging moments. I also wish to thank Professor P. L. Richards for sharing his vast knowledge of far-infrared physics and techniques and for the use of his experimental equipment.

I would especially like to thank K. H. Yang for his assistance in the mixing experiments with two dye lasers and for many fruitful discussions, especially about his picosecond pulse experiments and the calibration of the far-infrared detectors for our dye laser experiment. Patrick's knowledge of far-infrared measurement techniques was a key to the successful completion of our dye laser experiments. I would also like to thank the graduate and post-doctoral students -- especially A. J. Schmidt, M. Loy, and G. Wong -- in Professor Shen's group for many educational discussions about nonlinear optics.

I also wish to thank the following individuals and organizations at Lawrence Livermore Laboratory: T. Wainwright, my division head, and J. A. Fleck, Jr., my supervisor, for their patience with the time it has taken me to complete this thesis; R. L. Pexton for providing a complex error function and a double integration subroutine; M. D. Feit for his comments on Chapter III; and T Division for providing computer time.

And last, but certainly not least, I wish to thank my wife, Louise, for her love, understanding, and encouragement during this long project.

This work was performed under the auspices of the U.S. Energy Research and Development Administration.

APPENDIX A

The extraordinary ray assumed in Sec. IIA of Chapter II actually has the form

$$\vec{E}_2(\vec{r},t) = \frac{\mathscr{E}_2\hat{e}_2\sqrt{1+\xi_\Delta^2}}{\sqrt{(1+i\xi_{2x})(1+i\xi_{2y})}} \exp\left[-\frac{(x-\zeta_2 z)^2}{w_2^2(1+i\xi_{2x})} - \frac{y^2}{w_2^2(1+i\xi_{2y})}\right]$$

$$\exp[i(k_2 z - \omega_2 t)] \qquad \text{(A1)}$$

where

$$\xi_\Delta = (z_{0,2x}-z_{0,2y})n_2^4/\{k_2 w_2^2 n_{em,2}^2 (n_2^2+n_{o,2}^2)\}$$

$$\xi_{ex} = 2(z-z_{0,2x})\ [n_2^4/\{k_2 w_2^2 n_{em,2}^2 n_{o,2}^2\}]$$

$$\xi_{ey} = 2(z-z_{0,2y})[n_2^2/\{k_2 w_2^2 n_{em,2}^2]$$

$\hat{e}_2$ = unit vector parallel to the electric field of the e-ray for a normally incident laser beam

and the remaining parameters are as defined for Eq. (1). This expression with $z_{0,2x} = z_{0,2y}$ is essentially the same as the one given in Appendix I of Ref. 31, but there the factors in the square brackets in the definition of ξ_{2x} and ξ_{2y} were approximated by 1.

The nonlinear polarization $\vec{P}^{(2)}(\vec{r},\omega)$ is obtained from Eq. (2) using the expressions of $\vec{E}_1$ in Eq. (1) and $\vec{E}_2$ in Eq. (A1). The transverse Fourier transform of $\vec{P}^{(2)}(\vec{r},\omega)$ gives $\vec{P}^{(2)}(\vec{k}_T,z)$. To obtain

the expression of $\vec{P}^{(2)}(\vec{k}_T, z)$ in Eq. (3), we made the following simplifying assumptions. First, we assumed $w_1 = w_2 = w$. Second, we assumed a common focus for the two beams, $z_{0,1} = z_{0,2x} = z_{0,2y} = z_0$. Finally, we assumed $\xi_1 - \xi_{2x} \simeq \xi_1 - \xi_{2y} = 0$. This last assumption is reasonable as long as $3|\xi_1 - \xi_{2x}|$, $3|\xi_1 - \xi_{2y}| \ll \pi/2$. In our calculations, the largest value of $3|\xi_1 - \xi_{2x}|$ or $3|\xi_1 - \xi_{2y}|$ is 1 for the case of $\omega = 10\ cm^{-1}$, $w = 25\ \mu m$ and $\zeta = -0.02$. For all the other cases, $3|\xi_1 - \xi_{2x}|$ or $3|\xi_1 - \xi_{2y}|$ is much smaller than 1.

APPENDIX B

To derive Eq. (6), we first Fourier transform Eq. (4) and obtain

$$[\vec{k}\,\vec{k} - k^2\overleftrightarrow{1} + \omega^2 \overleftrightarrow{\varepsilon}/c^2] \cdot \vec{E}(\vec{k}) = -4\pi(\omega^2/c^2)\vec{P}^{(2)}(\vec{k})$$

$$\vec{k} \cdot \overleftrightarrow{\varepsilon} \cdot \vec{E}(\vec{k}) = -4\pi \vec{k} \cdot \vec{P}^{(2)}(\vec{k}) \tag{B1}$$

The particular solution of Eq. (B1) can be written in the form

$$\vec{E}^{p}(\vec{k}) = \overleftrightarrow{S}(k) \cdot \vec{P}^{(2)}(\vec{k}) \ .$$

From the inverse transform on k_z, we then have

$$\vec{E}^{p}(\vec{k}_T, z) = \frac{1}{2\pi} \int_{-\infty}^{\infty} dk_z \int_{-\infty}^{\infty} dz' e^{ik_z(z-z')} \overleftrightarrow{S}(\vec{k}) \cdot \vec{P}^{(2)}(\vec{k}_T, z') \tag{B2}$$

A straightforward, but tedious, application of the residue theorem finally leads to Eq. (6).

We also notice that Eqs. (6) and (7) are not the results of slowly varying envelope approximation. This is in fact generally true for the solution of optical mixing in the parametric approximation. For example, consider the simple case where the nonlinear process can be described by the wave equation

$$(\partial^2/\partial z^2 + k_o^2)\ E(z) = 4\pi(\omega^2/c^2)P^{NL}(z) \tag{B3}$$

where $P^{NL}(z) \neq 0$ only if $0 \leqslant z \leqslant \ell$. Then, in the region $0 \leqslant z \leqslant \ell$, the solution of the equation is

$$E(z) = \frac{2\pi\,\omega^2}{ik_o c^2}\left[\int_0^z P^{NL}(z')e^{ik_o(z-z')}\,dz' + \int_0^{\ell} P^{NL}(z')\,e^{-ik_o(z-z')}\,dz'\right] \qquad \text{(B4)}$$

No slowly varying envelope approximation was made in the derivation. In fact, one can easily show that, with the complete expression of $E(z)$ in Eq. (B4), the terms $\partial^2|E(z)|/\partial z^2$ and $2k_o\,\partial|E(z)|/\partial z$ are generally comparable in magnitude. The usual slowly varying envelope approximation is actually equivalent to neglecting waves propagating in the opposite direction.

APPENDIX C

Computation Methods for Chapter II

The results presented in section III of chapter II were obtained by numerically integrating Eq. (32) after substituting for $|\vec{E}_{T+}|^2$ the quantity $\{(\overleftrightarrow{T}_+\overleftrightarrow{F}_+)^+(\overleftrightarrow{T}_+\overleftrightarrow{F}_+)\}_{1,1}\ |E^p_{o+}|^2$ where the term in braces is the upper left matrix element of Eq. (30) evaluated for the special case $\hat{c} = \hat{x}$ and E^p_{o+} is obtained from Eq. (22) for the special case $\hat{o}_1 = \hat{y}$, $\hat{e}_2 = \hat{x}$, $\overleftrightarrow{\chi}^{(2)}:\hat{y}\hat{x} = \hat{y}\chi^{(2)}_{eff}$:

$$E^p_{o+}(\vec{k}_T,\ell) = \frac{2\pi i\omega^2}{k_{oz}c^2}\,\hat{o}_+\cdot\hat{y}\;\chi^{(2)}_{eff}\;\mathcal{E}_1\mathcal{E}_2^*\;\frac{w^2}{4}\exp(-\delta)\;Q(\gamma,\rho,\ell) \tag{C1}$$

where

$$\gamma \equiv [(k_x-\zeta k_1)^2 + k_y^2]/2k_1^2w^2$$

$$\rho \equiv (2\gamma)^{-1}[-k_T^2z_o/k_1^2w^2 + a_1(k_x-\zeta k_1)/k_1w^2$$

$$+\frac{1}{2}\,i\zeta k_x(1-2iz_0/k_1w^2) - i(k_1-k_2^*-k_{oz})]$$

$$\delta \equiv a_1^2/2w^2 + \frac{1}{8}\,w^2k_T^2\,(1 + 4z_o^2/k_1^2w^4)$$

$$+\frac{1}{2}\,ik_xa_1(1+2iz_0/k_1w^2) + 2\mathrm{Im}(k_{oz})$$

and

$$Q(\gamma,\rho,\ell) \equiv \exp(\gamma\rho^2)\int_o^\ell dz\,\exp[-\gamma(\rho+z)^2] \tag{C2}$$

$$Q(\gamma,\rho,\ell) \equiv \frac{1}{2}\sqrt{\pi/\gamma}\ [W\{i\gamma^{1/2}\rho\} - \exp\{-\gamma\ell(2\rho+\ell)\}\ W\{i\gamma^{1/2}(\rho+\ell)\} \qquad \text{(C3)}$$

with $W(\xi) \equiv \frac{2}{\sqrt{\pi}} \exp(-\xi^2) \int_{-i\xi}^{\infty} \exp(-u^2)du$. [See W. Gautschi, SIAM J. Numer. Anal. 7, 187 (1970).]

Except for the factor $|Q(\gamma,\rho,\ell)|^2$, all of the quantities in the integrand are simple to evaluate numerically. The function $Q(\gamma,\rho,\ell)$, however, has some mathematical properties that must be circumvented to successfully integrate Eq. (32) on a digital computer. The first of these properties is that although $W(Z)$ is bounded and analytic in the upper half of the complex plane, it diverges in the lower half-plane as $\mathrm{Im}(Z) \to -\infty$. Such Z values can occur when $Q(\gamma,\rho,\ell)$ is evaluated for laser beams that are focused behind the exit face of the nonlinear slab; fortunately, for such problems $Q(\gamma,\rho,\ell)$ can be re-expressed as

$$Q(\gamma,\rho,\ell) = \exp\{\gamma\ell(2\rho+\ell)\}\ [Q\{\gamma^*,-(\rho^*+\ell),\ell\}]^* .$$

In this form the signs of the imaginary parts of the arguments of $W(Z)$ are changed; by choosing this alternate form when $\mathrm{Re}(\gamma^{1/2}\rho)$ and $\mathrm{Re}[\gamma^{1/2}(\rho+\ell)]$ are both negative, the magnitude of the largest negative imaginary part of an argument of $W(Z)$ is reduced and often both of the $W(Z)$ arguments are moved into the upper half-plane. The derivation of the above symmetry relation is straight-forward:

$$Q(\gamma,\rho,\ell) = \exp(\ell\rho^2) \int_0^{\ell} \exp[-\gamma(\rho+\ell)^2]dz$$

$$= \exp[-\gamma(2\rho+\ell)+\gamma(\rho+\ell)^2] \int_0^{\ell} \exp\{-\gamma[z'-(\rho+\ell)]^2\}dz'$$

$$= \exp[-\gamma\ell(2\rho+\ell)]\ Q[\gamma,-(\rho+\ell),\ell]$$

$$= \exp[-\gamma\ell(2\rho+\ell)]\ \{Q[\gamma^*,-(\rho^*+\ell),\ell]\}^*$$

There are two other parameter regions in which $Q(\gamma,\rho,\ell)$ is difficult to evaluate on a digital computer. The first of these is the region in which both $|\gamma^{1/2}\rho|$ and $|\gamma^{1/2}(\rho+\ell)|$ are very small. Because $W(0) = 1$ and $Q(\gamma,\rho,\ell)$ involves the difference between two values of $W(Z)$, Eq. (C.3) cannot be used to evaluate $Q(\gamma,\rho,\ell)$ in this region on a digital computer with finite precision (14 significant digits on a CDC 7600). However, in the region defined by $|\mathrm{Re}(\gamma^{1/2}\rho)| + |\mathrm{Im}(\gamma^{1/2}\rho)| + |\mathrm{Re}[\gamma^{1/2}(\rho+\ell)]| + |\mathrm{Im}[\gamma^{1/2}(\rho+\ell)]| < .001$ the series expansion $Q(\gamma,\rho,\ell) \cong \ell[1 - \frac{1}{3}\gamma\ell(\ell+3\rho)]$ is accurate to better than 1 part in 10^6. (This region is simply one of many choices which keep the loss of significance [round-off error] and the inevitable difference between the series and the results of Eq. (C.3) [truncation error] at the boundary of the region to less than $10^{-6}|Q(\gamma,\rho,\ell)|$.) The final parameter region in which $Q(\gamma,\rho,\ell)$ is difficult to evaluate is the region where $\gamma^{1/2}\ell \ll 1$ but $\gamma^{1/2}|\rho|$ is large. Again round-off error is the source of the problem and a series expansion is the solution. When $\gamma\ell^2 \ll 1$, the exponential function in the integrand of Eq. (C.2) can be written $\exp[-\gamma(\rho+z)^2] \cong \exp(-\gamma\rho^2)\exp(-2\gamma\rho z)(1-\gamma z^2+\ldots)$.

When $\gamma \frac{1}{2} \ell < .001$, we evaluate $Q(\gamma,\rho,\ell)$ via the first term a the asymptotic expansion that is obtained from a term-by-term integration of Eq. (C.2) with $\exp[-\gamma(\rho+z)^2]$ replaced by this series expansion:

$$Q(\gamma,\rho,\ell) \cong \frac{\exp(-2\gamma\rho\ell) - 1}{-2\gamma\rho}$$

The double integral in Eq. (32) was re-expressed as an iterated integral with constant limits via the change of variables for the inner (k_y) integral: $v = k_y[(\omega/c)^2-k_x^2]^{-1/2}$. Both the inner and outer integrals were evaluated with an adaptive three point Gaussian quadrature algorithm. For each k_x, the inner(v) integral was adaptively refined until at least three levels of subdivision occurred and two successive estimates of its value differed by less than

$$.001\cdot[(\omega/c)^2-k_x^2]^{-1/2} \int_{-\omega/c}^{\omega/c} dk_x' \frac{c}{2\pi} \left(\frac{ck_z}{\omega}\right) |\vec{E}_{T+}(k_x',0)|^2 ,$$

which was estimated with a trapezoidal rule on 100 intervals. The outer k_x integral was adaptively refined until two successive estimates differed by less than .1% of its initial estimate. The existance of a phase matched or Cerenkov cone whose angular width was in some cases much smaller than its operning angle at large far-infrared frequencies (like 100 cm^{-1} for a 1 cm long crystal) made this careful check necessary to be sure the peak of this hollow cone was sampled.

A listing of the computer program follows:

```
      PROGRAM INFRA(IRIN,FOUT,GFILE,TAPE2=IRIN,TAPE3=FOUT,TAPE6=GFILE,   INFR  20
     1               TAPE100)                                            INFR  30
      COMPLEX H3,H4,H5,H6,H11,SMONE,H5S                                   INFR  40
      COMPLEX EO,EE,ECCZ,EOCX,ECS,EOEEI,EEI,EECZ,EECX,AN2,WAC             INFR  50
      LOGICAL P                                                           INFR  60
      COMMON  WORK(11),XCC,YOC,ZOO,WIDE,XTLL,DFREQ,FRQL,P1,P2,DKO,WOPO,   INFR  70
     1        XXI,PNLS(3),XNOL(2),XNEL(2),XONO(39,4),NT,XONE(39,4),NT1,   INFR  80
     2        CUT,XO,YO,XLCC,BW,XLN,DFRQ,DK,WCP,XCN,XCA,XEON,XEDA,        INFR  90
     3        CLOW,DHIGH,NR,STEP,ANAME,ISTAR,H1,H2,H2P,H2PP,H2PPP,        INFR 100
     4        H3,H4,H5,H5P,H6,H7,H8,H9,H10,H11,H12,H13,H14,XORS,XORC,     INFR 110
     5        AKXC                                                        INFR 120
      COMMON /BC/ AKV,AKVI,FRQS,EL,ECCZ,EOCX,ECS,ECEEI,EEI,EECZ,EECX,    INFR 130
     1            AN2,WAC                                                 INFR 140
      COMMON /CONST/ C,PI,SMONE,COMPR(13)                                 INFR 150
      COMMON /ARGA62/ C62,D62,ER,MM,NN,A1,B1,EP,MP,N,WT                   INFR 160
      COMMON /PASS/ FIELD3,A62G,POWER1,AKX,AKY,DIRK,P                     INFR 170
      COMMON /GRPH/ HORIZ(1000),VERT(1000),VERT1(1000)                    INFR 180
      DIMENSION PH3(2),PH4(2),PH5(2),PH6(2),PH11(2),PH5S(2),PSMONE(2)     INFR 190
      EQUIVALENCE (PH3,H3),(PH4,H4),(PH5,H5),(PH6,H6),(PH11,H11),         INFR 200
     1 (PH5S,H5S),(PSMONE,SMONE)                                          INFR 210
      DATA  C,PI,COMPR /2.997925E+10,3.1415927,5HPARAM,5HNTBLO,5HNTBLE,   INFR 220
     1  5HPHASE, 4HFREQ,5HWIDTH,5HABSRB,5HANGUL,5HTHICK,5HXDSPL,5HYDSPL,   INFR 230
     2     4HFLOC,3HEND/                                                  INFR 240
      DATA PSMONE/0.,1./                                                  INFR 250
      DATA  ISW /0B/                                                      INFR 260
      DATA FIELD3 /0.0/                                                   INFR 270
      DIMENSION IBETA(2)                                                  INFR 280
      H1,H2, ... CONTAIN PRECOMPUTED VALUES TO BE USED BY ROUTINE FIELD   INFR 290
                 THESE VALUES DO NOT DEPEND ON AKX OR AKY AND THUS        INFR 300
                 REMAIN FIXED DURING THE INTEGRATION TO FIND THE          INFR 310
                 POWER GENERATED                                          INFR 320
      DIRK IS STORAGE FOR THE DIRECTION COSINE OF K FOR THE TRANSMITTED   INFR 330
                 RAY ON THE FAR SIDE OF THE CRYSTAL                       INFR 340
      CALL DEVICE(6HCREATE,4HFOUT,50000)                                  INFR 350
      CALL DEVICE(6HCREATE,5HGFILE,50000,IERR,MWD)                        INFR 360
      NR = LOC(AKXC)-LOC(WORK(1))+1                                       INFR 370
      DO 10 I=1,NR                                                        INFR 380
   10 WORK(I)  = 0.0                                                      INFR 390
      CONDR = PI/180.                                                     INFR 400
      CONIW = 2.*PI*C                                                     INFR 410
      WRITE(3,2001) NR,I,COMPR                                            INFR 420
      CALL DD80ID(10HBOX T44 JM,1)                                        INFR 430
      CALL KEEP80(1)                                                      INFR 440
   20 ASSIGN 25 TO M1                                                     INFR 450
      ASSIGN 31 TO M                                                      INFR 460
   21 READ(2,1000) ANAME,ISTAR,NR,(WORK(I),I=1,9)                         INFR 470
      GO TO M1                                                            INFR 480
   25 DO 30 I=1,13                                                        INFR 490
      IF(ANAME-COMPR(I)) 30,35,30                                         INFR 500
   30 CONTINUE                                                            INFR 510
      ASSIGN 20 TO M                                                      INFR 520
      WRITE(3,1001)                                                       INFR 530
   35 WRITE(3,1002) ANAME,ISTAR,NR,(WORK(J),J=1,9)                        INFR 540
      GO TO M                                                             INFR 550
   31 IF(I-2) 40,130,32                                                   INFR 560
   32 IF(I-3) 120,230,50                                                  INFR 570
   40 FRQL = 2.*PI/WORK(1)*(1.0E+8)*C                                     INFR 580
      DFREQ =   CONIW*WORK(2)                                             INFR 590
      WIDE = WORK(3)                                                      INFR 600
      P1 = WORK(4)                                                        INFR 610
      P2 = WORK(5)                                                        INFR 620
```

```
      XOO = WORK(6)                                                    INFR 630
      YOO = WORK(7)                                                    INFR 640
      ZOO       = WORK(8)                                              INFR 650
      XTLL       = WORK(9)                                             INFR 660
      ISW = ISW.OR.(1B)                                                INFR 670
      IF(NR-2) 20,46,20                                                INFR 680
   46 ASSIGN 35 TO M1                                                  INFR 690
      ASSIGN 47 TO M                                                   INFR 700
      GO TO 21                                                         INFR 710
   47 XNCL(1) = WORK(1)                                                INFR 720
      XNCL(2) = WORK(2)*.5                                             INFR 730
      XNFL(1) = WORK(1) - WORK(3)                                      INFR 740
      WOPO = WORK(3)                                                   INFR 750
      DKO = WORK(9)                                                    INFR 760
      XNFL(2) = WORK(2)*.5                                             INFR 770
      XXI       = WORK(4)*1.E-6                                        INFR 780
      PNLS(3) =  SQRT(WORK(5)**2+WORK(6)**2+WORK(7)**2)                INFR 790
      PNLS(1) = WORK(5)/PNLS(3)                                        INFR 800
      PNLS(2) = WORK(6)/PNLS(3)                                        INFR 810
      PNLS(3) = WORK(7)/PNLS(3)                                        INFR 820
      CUT = WORK(8)                                                    INFR 830
      ISW = ISW.OR.(2B)                                                INFR 840
      GO TO 20                                                         INFR 850
  130 K = 3                                                            INFR 860
      J1 = 3*NR                                                        INFR 870
      ISW = ISW.OR.(4B)                                                INFR 880
      ASSIGN 35 TO M1                                                  INFR 890
      ASSIGN 131 TO M                                                  INFR 900
  131 DO 132 I=1,3                                                     INFR 910
      L = K+I-3                                                        INFR 920
      IF(WORK(3*I-2)) 135,136,135                                      INFR 930
  135 XDNO(L,1) = WORK(3*I-2)*CONIW                                    INFR 940
      XDNO(L,2) = WORK(3*I-1)                                          INFR 950
  132 XDNO(L,3) = WORK(3*I)*.5                                         INFR 960
      NT = J1                                                          INFR 970
      K = K+3                                                          INFR 980
      IF(K-J1) 21,21,137                                               INFR 990
  136 NT = L-1                                                         INFR1000
  137 WRITE(6) COMPR(2),NT,(HORIZ(I),I=1,19)                           INFR1010
      CALL SPLICE(NT,XDNO(1,1),XDNO(1,3),XDNO(1,4))                    INFR1020
      WRITE(6) ((XDNO(I,J),I=1,NT),J=1,4)                              INFR1030
      P = .FALSE.                                                      INFR1040
      KK = 0                                                           INFR1050
      DO 138 I=2,NT                                                    INFR1060
      DO 138 J=1,5                                                     INFR1070
      KK = KK+1                                                        INFR1080
      U3 = XDNO(1,1)-XDNO(I-1,1)                                       INFR1090
      U1 = .2*U3*FLOAT(J)                                              INFR1100
      U2 = .2*U3*FLOAT(5-J)                                            INFR1110
      HORIZ(KK) = (XDNO(I-1,1)+U1)/CONIW                               INFR1120
  138 VERT(KK)  = 2.*(XDNO(I,3)*U1+XDNO(I-1,3)*U2  -                   INFR1130
     1              U1*U2*(XDNO(I-1,4)*(U3+U2)+XDNO(I,4)*(U3+U1))/6.)/U3 INFR1140
      CALL GRAPH(KK,9HALPHA-ORD ,16HFREQUENCY (CM-1) ,                 INFR1150
     1  28HO-RAY ABSORPTION COEF (CM-1)     )                          INFR1160
      GO TO 20                                                         INFR1170
  230 K = 3                                                            INFR1180
      J1 = 3*NR                                                        INFR1190
      ISW = ISW.OR.(10B)                                               INFR1200
      ASSIGN 35 TO M1                                                  INFR1210
      ASSIGN 231 TO M                                                  INFR1220
  231 DO 232 I=1,3                                                     INFR1230
      L = K+I-3                                                        INFR1240
```

```
      IF(WORK(3*I-2)) 235,236,235                                          INFR1250
  235 XONE(L,1) = WORK(3*I-2)*CONIW                                        INFR1260
      XONE(L,2) = WORK(3*I-1)                                              INFR1270
  232 XONE(L,3) = WORK(3*I)*.5                                             INFR1280
      NT1 = J1                                                             INFR1290
      K = K+3                                                              INFR1300
      IF(K-J1) 21,21,237                                                   INFR1310
  236 NT1 = L-1                                                            INFR1320
  237 WRITE(6) COMPR(3),NT1,(HORIZ(I),I=1,19)                              INFR1330
      CALL SPLICE(NT1,XONE(1,1),XONE(1,3),XONE(1,4))                       INFR1340
      WRITE(6) ((XONE(I,J),I=1,NT1),J=1,4)                                 INFR1350
      P = .FALSE.                                                          INFR1360
      KK = 0                                                               INFR1370
      DO 238 I=2,NT1                                                       INFR1380
      DO 238 J=1,5                                                         INFR1390
      KK = KK+1                                                            INFR1400
      U3 = XONE(I,1)-XONE(I-1,1)                                           INFR1410
      U1 = .2*U3*FLOAT(J)                                                  INFR1420
      U2 = .2*U3*FLOAT(5-J)                                                INFR1430
      HORIZ(KK) = (XONE(I-1,1)+U1)/CONIW                                   INFR1440
  238 VERT(KK)  = 2.*(XONE(I,3)*U1+XONE(I-1,3)*U2  -                       INFR1450
     1              U1*U2*(XONE(I-1,4)*(U3+U2)+XONE(I,4)*(U3+U1))/6.)/U3  INFR1460
      CALL GRAPH(KK,9HALPHA-EXT,16HFREQUENCY (CM-1) ,                      INFR1470
     1  28HE-RAY ABSORPTION COEF (CM-1)     )                             INFR1480
      GO TO 20                                                             INFR1490
   50 IF(ISW-(17B))120,52,120                                              INFR1500
   52 NR = WORK(3)                                                         INFR1510
      P = .TRUE.                                                           INFR1520
      DLOW = WORK(1)                                                       INFR1530
      DHIGH = WORK(2)                                                      INFR1540
      XO = XOO                                                             INFR1550
      YO = YOO                                                             INFR1560
      XLOC = ZOO                                                           INFR1570
      Co2 = 0.                                                             INFR1580
      IF(YO.NE.0.) Co2 = -1.                                               INFR1590
      DFRQ = DFREQ                                                         INFR1600
      BW = WIDE                                                            INFR1610
      XLN = XTLL                                                           INFR1620
      WOP = WOPO                                                           INFR1630
      DK = DKO                                                             INFR1640
      STEP = (DHIGH-DLOW)/WORK(3)                                          INFR1650
      NR = NR+1                                                            INFR1660
      WRITE(3,1004) STEP,COMPR(I)                                          INFR1670
      CALL SETEPS                                                          INFR1680
      CALL ORIENT                                                          INFR1690
      IDPLT = I                                                            INFR1700
      GO TO (120,120,120,60,70,80,90,100,110,140,150,160,120),I            INFR1710
C  60 CALL PHASE                                                           INFR1720
   60 CONTINUE                                                             INFR1730
      DK = DLOW                                                            INFR1740
      DO 61 I=1,NR                                                         INFR1750
      HORIZ(I) = DK                                                        INFR1760
      CALL ORIENT                                                          INFR1770
      CALL SETCON(I)                                                       INFR1780
   62 VERT(I) = POWER(P)                                                   INFR1790
      VERT1(I) = POWER1                                                    INFR1800
   61 DK = DK+STEP                                                         INFR1810
      ASSIGN 69 TO M                                                       INFR1820
      GO TO 168                                                            INFR1830
   69 CONTINUE                                                             INFR1840
      CALL GRAPH(NR,10HP.M. CURVE    ,                                     INFR1850
     122HPHASE MISMATCH (1./CM),23HPOWER GENERATED (WATTS)                 INFR1860
```

```
      GO TO 20                                                          INFR1870
C  70 CALL FREQ                                                        INFR1880
C     NON-PHASE MATCHABLE FREQUENCIES HAVE THE TOTAL RADIATED POWER     INFR1890
C     COMPUTED FOR THE OPTIC AXIS PARALLEL TO THE LASER BEAMS           INFR1900
   70 CONTINUE                                                         INFR1910
      DO 72 I=1,NR                                                     INFR1920
      DFRQ = DLOW*CONIW                                                INFR1930
      HORIZ(I) = DLOW                                                  INFR1940
      CALL SETEPS                                                      INFR1950
      CALL CKIENT                                                      INFR1960
      CALL SETCON(I)                                                   INFR1970
      VERT(I) = POWER(P)                                               INFR1980
      VERT1(I) = POWER1                                                INFR1990
   72 DLOW = DLOW+STEP                                                 INFR2000
      ASSIGN 79 TO M                                                   INFR2010
      GO TO 168                                                        INFR2020
   79 CONTINUE                                                         INFR2030
      CALL GRAPH(NR,10HP.M. FREQ.  ,                                   INFR2040
     1 17HFREQUENCY  (1/CM),23HPOWER GENERATED (WATTS)                 INFR2050
      GO TO 20                                                         INFR2060
C  80 CALL WIDTH                                                       INFR2070
   80 CONTINUE                                                         INFR2080
      BW = DLOW                                                        INFR2090
      DO 81 I=1,NR                                                     INFR2100
      HORIZ(I) = BW                                                    INFR2110
      CALL SETCON(I)                                                   INFR2120
      VERT(I) = POWER(P)                                               INFR2130
      VERT1(I) = POWER1                                                INFR2140
   81 BW = BW+STEP                                                     INFR2150
      ASSIGN 89 TO M                                                   INFR2160
      GO TO 168                                                        INFR2170
   89 CONTINUE                                                         INFR2180
      CALL GRAPH(NR,10HSPOT SIZE   ,                                   INFR2190
     1 35HLASER BEAM WIDTH (E**-2 POINT) (CM)   ,                      INFR2200
     2 23HPOWER GENERATED (WATTS)    )                                 INFR2210
      GO TO 20                                                         INFR2220
C  90 CALL ABSRB                                                       INFR2230
   90 CONTINUE                                                         INFR2240
      DO 91 I=1,NR                                                     INFR2250
      HORIZ(I) = DLOW                                                  INFR2260
      XDA = .5*DLOW                                                    INFR2270
      CALL SETCON(I)                                                   INFR2280
      VERT(I) = POWER(P)                                               INFR2290
      VERT1(I) = POWER1                                                INFR2300
   91 DLOW = DLOW+STEP                                                 INFR2310
      ASSIGN 99 TO M                                                   INFR2320
      GO TO 168                                                        INFR2330
   99 CONTINUE                                                         INFR2340
      CALL GRAPH(NR,10HABSORPTION    ,                                 INFR2350
     1 23HABSORPTION COEF. (1/CM) ,23HPOWER GENERATED (WATTS)   )      INFR2360
      GO TO 20                                                         INFR2370
C 100 CALL ANGUL                                                       INFR2380
  100 CONTINUE                                                         INFR2390
      P = .FALSE.                                                      INFR2400
      CALL SETCON(1)                                                   INFR2410
      AI = ABS(DFRQ/C)                                                 INFR2420
      AKY = 0.                                                         INFR2430
      DLOW1 = DLOW                                                     INFR2440
      DO 101 I=1,NR                                                    INFR2450
      AKX = AI*SIN(DLOW1*CONDR)                                        INFR2460
C     AVOID SINGULARITY IN TERMS CALCULATED BY FIELD.                  INFR2470
      IF(ABS(AKX).LT.1.0E-40) AKX=1.0E-40                              INFR2480
```

```
      HORIZ(I) = DLOW1                                                  INFR2490
      VERT(I) = FIELD(P)*H1                                             INFR2500
      VERT(I) = VERT(I)*(DFRQ)**2/CONIW*DIRK                            INFR2510
  101 DLOW1 = DLOW1+STEP                                                INFR2520
      ASSIGN 106 TO M                                                   INFR2530
      GO TO 168                                                         INFR2540
  106 CONTINUE                                                          INFR2550
      CALL GRAPH(NR,10HPWR DIST.  ,                                     INFR2560
     132HANGLE IN PLANE OF INC. (DEGREES)      ,20HPOWER PER STERADIAN )INFR2570
      AKX = 1.E-40                                                      INFR2580
      DO 105 I=1,NR                                                     INFR2590
      AKY = AI*SIN(DLOW*CONDR)                                          INFR2600
C     AVOID SINGULARITY IN TERMS CALCULATED BY FIELD.                   INFR2610
      IF(ABS(AKY).LT.1.0E-40) AKY=1.0E-40                               INFR2620
      HORIZ(I) = DLOW                                                   INFR2630
      VERT(I) = FIELD(P)*H1                                             INFR2640
      VERT(I) = VERT(I)*(DFRQ)**2/CONIW*DIRK                            INFR2650
  105 DLOW = DLOW+STEP                                                  INFR2660
      ASSIGN 109 TO M                                                   INFR2670
      GO TO 168                                                         INFR2680
  109 CONTINUE                                                          INFR2690
      CALL GRAPH(NR,10HPWR DIST.  ,                                     INFR2700
     135HANGLE PERP. TO PLANE OF INC. (DEG.)   ,20HPOWER PER STERADIAN )INFR2710
      GO TO 20                                                          INFR2720
C 110 CALL THICK                                                        INFR2730
  110 CONTINUE                                                          INFR2740
      FRACT = WORK(4)                                                   INFR2750
      XLN = DLOW                                                        INFR2760
      DO 111 I=1,NR                                                     INFR2770
      IF(ISTAR.EQ.1H*) XLOC = -XLN*FRACT                                INFR2780
      CALL SETCON(I)                                                    INFR2790
      HORIZ(I) = XLN                                                    INFR2800
      VERT(I) = POWER(P)                                                INFR2810
      VERT1(I) = POWER1                                                 INFR2820
  111 XLN = XLN+STEP                                                    INFR2830
      ASSIGN 119 TO M                                                   INFR2840
      GO TO 168                                                         INFR2850
  119 CONTINUE                                                          INFR2860
      CALL GRAPH(NR,10HLENGTH     ,                                     INFR2870
     1 11HLENGTH (CM)  ,23HPOWER GENERATED (WATTS)                      INFR2880
      GO TO 20                                                          INFR2890
C     X DISPLACEMENT                                                    INFR2900
  140 CONTINUE                                                          INFR2910
      XO = DLOW                                                         INFR2920
      DO 145 I=1,NR                                                     INFR2930
      CALL SETCON(I)                                                    INFR2940
      VERT(I) = POWER(P)                                                INFR2950
      VERT1(I) = POWER1                                                 INFR2960
      HORIZ(I) = XO                                                     INFR2970
  145 XO = XO + STEP                                                    INFR2980
      ASSIGN 146 TO M                                                   INFR2990
      GO TO 168                                                         INFR3000
  146 CALL GRAPH(NR,10HX-DISPLACE,22HBEAM CENTER SHIFT (CM),            INFR3010
     1  23HPOWER GENERATED (WATTS)   )                                 INFR3020
      GO TO 20                                                          INFR3030
C     Y DISPLACEMENT                                                    INFR3040
  150 CONTINUE                                                          INFR3050
      CO2 = -1.                                                         INFR3060
      YO = DLOW                                                         INFR3070
      DO 155 I=1,NR                                                     INFR3080
      CALL SETCON(I)                                                    INFR3090
      VERT(I) = POWER(P)                                                INFR3100
```

```
      VERT1(I) = POWER1                                                  INFR3110
      HORIZ(I) = YO                                                      INFR3120
  155 YO = YO + STEP                                                     INFR3130
      ASSIGN 156 TO M                                                    INFR3140
      GO TO 168                                                          INFR3150
  156 CALL GRAPH(NR,10HY-DISPLACE,22HBEAM CENTER SHIFT (CM),             INFR3160
     1  23HPOWER GENERATED (WATTS)   )                                   INFR3170
      GO TO 20                                                           INFR3180
  160 CONTINUE                                                           INFR3190
      XLOC = DLOW                                                        INFR3200
      DO 161 I=1,NR                                                      INFR3210
      HORIZ(I) = XLOC                                                    INFR3220
      CALL SETCON(I)                                                     INFR3230
      VERT(I) = POWER(P)                                                 INFR3240
      VERT1(I) = POWER1                                                  INFR3250
  161 XLOC = XLOC + STEP                                                 INFR3260
      ASSIGN 162 TO M                                                    INFR3270
      GO TO 168                                                          INFR3280
  162 CALL GRAPH(NR,10HFOCUS LOC.,23HFOCAL PT. LOCATION (CM),            INFR3290
     1  23HPOWER GENERATED (WATTS)  )                                    INFR3300
      GO TO 20                                                           INFR3310
  120 WRITE(3,1003) I,ISW                                                INFR3320
      END FILE 6                                                         INFR3330
      CALL PNIO(IBETA)                                                   INFR3340
C     GET FIELD LENGTH                                                   INFR3350
C     LOCATE BLOCK FOR IOD#S ETC. AS AN INDEX FOR ARRAY IBETA            INFR3360
      IBETA = IBETA+MWD-LOC(IBETA(0))-200B                               INFR3370
C      LOCATE THE WORD CONTAINING THE FILE LENGTH                        INFR3380
      IBETA = (IBETA(IBETA).AND.777777B)-LOC(IBETA(0))                   INFR3390
C     GET FILE LENGTH                                                    INFR3400
      IBETA(2) = ISR(IBETA(IBETA),36).AND.777777778                      INFR3410
C     ROUND LENGTH TO THE NEAREST .GE. 512 WORDS                         INFR3420
      IBETA(2) = ISL(ISR((IBETA(2)+777B),9),9)                           INFR3430
C     SET-UP THE FILE NAME IN BETA WORDS FOR A GOB CALL                  INFR3440
C     THE LEADING BLANKS ARE NECESSARY - R FORMAT DOES NOT SUPPLY THEM   INFR3450
      IBETA(1) = 10H      GFILE                                          INFR3460
C      SWITCH THE FILE NAME FROM CHIP DISPLAY CODE TO ASCII              INFR3470
      CALL SWITCH(3HDTA,IBETA,1)                                         INFR3480
      CALL GOB(1200B,IERR,0,IBETA)                                       INFR3490
      CALL DEVICE(6HCLOSER,5HGFILE)                                      INFR3500
      CALL PLOTE                                                         INFR3510
      CALL EXIT                                                          INFR3520
C     ROUTINE TO PRINT THE CALCULATED CURVE PRIOR TO CRT PLOTTING        INFR3530
  168 WRITE(3,1007)                                                      INFR3540
      DO 169 I=1,NR,8                                                    INFR3550
      K = I+7                                                            INFR3560
      IF(K.GT.NR) K=NR                                                   INFR3570
      WRITE(3,1005)  HORIZ(I),(VERT(J),J=I,K)                            INFR3580
  169 CONTINUE                                                           INFR3590
      WRITE(3,1007)                                                      INFR3600
      WRITE(6) COMPR(IDPLT),NR,HORIZ(1),STEP,XO,YO,XLOC,BW,P1,P2,        INFR3610
     1          FRQL,XXI,PNLS,XNUL,XNEL,XLN,DFRQ,WCP,DK,                INFR3620
     2           XDN,XDA,XEDN,XEDA                                       INFR3630
      WRITE(6) (VERT(I),I=1,NR)                                          INFR3640
      IF(.NOT.P) GO TO M                                                 INFR3650
      DO 170 I=1,NR,8                                                    INFR3660
      K = I+7                                                            INFR3670
      IF(K.GT.NR) K=NR                                                   INFR3680
      WRITE(3,1005) HORIZ(I),(VERT1(J),J=I,K)                            INFR3690
  170 CONTINUE                                                           INFR3700
      WRITE(3,1007)                                                      INFR3710
      WRITE(6) (VERT1(I),I=1,NR)                                         INFR3720
```

```
      GO TO M                                                                  INFR3730
 1000 FORMAT(A5,A1,I2,9E8.1)                                                   INFR3740
 1001 FORMAT (17H CARD REJECTED -  )                                           INFR3750
 1002 FORMAT (1H ,A5,A1,1X,I2,9E12.4 /)                                        INFR3760
 1003 FORMAT (//// 11H END-OF-JOB ,2I5/1H1)                                    INFR3770
 1004 FORMAT(//15H STEP SIZE IS  ,E11.4,17H  PROCEDURE IS     ,A5/)            INFR3780
 1005 FORMAT( E12.4,8E13.4)                                                    INFR3790
 1007 FORMAT(/)                                                                INFR3800
 2001 FORMAT(2I20,9(2X,A5)/40X,4(2X,A5))                                       INFR3810
      END                                                                      INFR3820
*     FORTRAN            POWER                                               INFR3830
      FUNCTION POWER(QQQ)                                                      INFR3840
      COMPLEX H3,H4,H5,H6,H11,SMONE,H5S                                        INFR3850
      COMPLEX EO,EE,EOCZ,EOCX,EOS,EOEEI,EEI,EECZ,EECX,AN2,WAC                  INFR3860
      LOGICAL P                                                                INFR3870
      COMMON  WORK(11),XOO,YOO,ZOO,WIDE,XTLL,DFREQ,FRQL,P1,P2,DKO,WOPO,        INFR3880
     1        XXI,PNLS(3),XNOL(2),XNEL(2),XDNO(39,4),NT,XDNE(39,4),NT1,        INFR3890
     2        CUT,XO,YO,XLOC,BW,XLN,DFRQ,DK,WCP,XDN,XDA,XEDN,XEDA,             INFR3900
     3        DLOW,DHIGH,NR,STEP,ANAME,ISTAR,H1,H2,H2P,H2PP,H2PPP,             INFR3910
     4        H3,H4,H5,H5P,H6,H7,H8,H9,H10,H11,H12,H13,H14,XORS,XORC,          INFR3920
     5        AKXC                                                             INFR3930
      COMMON /BC/ AKV,AKVI,FRQS,EO,EOCZ,EOCX,EOS,EOEEI,EEI,EECZ,EECX,         INFR3940
     1            AN2,WAC                                                      INFR3950
      COMMON /CONST/ C,PI,SMONE,COMPR(13)                                      INFR3960
      COMMON /ARGA62/ C62,D62,ER,MM,NN,A1,B1,EP,MP,N,HT                        INFR3970
      COMMON /PASS/ FIELD3,A62G,POWER1,AKX,AKY,DIRK,P                          INFR3980
      COMMON /GRPH/ HORIZ(1000),VERT(1000),VERT1(1000)                         INFR3990
      DATA C62,D62,ER,MM,NN,EP,MP,N /0.,1.,1.E-3,0,20,1.E-3,0,20/              INFR4000
      DATA ERS,NEST2 /.001,48/                                                 INFR4010
      B1   = ABS(DFRQ/C*CUT)                                                   INFR4020
      A1 = -B1                                                                 INFR4030
      MPREV = MM                                                               INFR4040
      MM = 0                                                                   INFR4050
      NEST1 = 2*NEST2                                                          INFR4060
      NEST = NEST1+1                                                           INFR4070
      AKY = 0.                                                                 INFR4080
      AKX = A1                                                                 INFR4090
      DKX = (B1-A1)/FLOAT(NEST)                                                INFR4100
      UEST = .5*FIELD(P)                                                       INFR4110
      DO 100 I=1,NEST1                                                         INFR4120
      AKX = AKX+DKX                                                            INFR4130
  100 UEST = UEST + FIELD(P)                                                   INFR4140
      AKX = B1                                                                 INFR4150
      UEST = .5*(UEST + .5*FIELD(P))                                           INFR4160
      ER = ERS*UEST                                                            INFR4170
    5 CON = C/(PI*(D62-C62))*H1                                                INFR4180
      POWER = CON*AGI(QQQ)                                                     INFR4190
      IF(MPREV.NE.MM) WRITE(3,1000) MM                                         INFR4200
 1000 FORMAT(2X,I7,22H FUNCTION EVALUATIONS                                    INFR4210
      RETURN                                                                   INFR4220
      END                                                                      INFR4230
      FUNCTION FUN(A,B)                                                        INFR4240
      COMPLEX H3,H4,H5,H6,H11,SMONE,H5S                                        INFR4250
      COMPLEX EO,EE,EOCZ,EOCX,EOS,EOEEI,EEI,EECZ,EECX,AN2,WAC                  INFR4260
      LOGICAL P                                                                INFR4270
      COMMON  WORK(11),XOO,YOO,ZOO,WIDE,XTLL,DFREQ,FRQL,P1,P2,DKO,WOPO,        INFR4280
     1        XXI,PNLS(3),XNOL(2),XNEL(2),XDNO(39,4),NT,XDNE(39,4),NT1,        INFR4290
     2        CUT,XO,YO,XLOC,BW,XLN,DFRQ,DK,WCP,XDN,XDA,XEDN,XEDA,             INFR4300
     3        DLOW,DHIGH,NR,STEP,ANAME,ISTAR,H1,H2,H2P,H2PP,H2PPP,             INFR4310
     4        H3,H4,H5,H5P,H6,H7,H8,H9,H10,H11,H12,H13,H14,XORS,XORC,          INFR4320
     5        AKXC                                                             INFR4330
      COMMON /BC/ AKV,AKVI,FRQS,EO,EOCZ,EOCX,EOS,EOEEI,EEI,EECZ,EECX,         INFR4340
```

```
     1            AN2,WAC                                                    INFR4350
          COMMON /CONST/ C,PI,SMONE,COMPR(13)                               INFR4360
          COMMON /ARGA62/ C62,D62,ER,MM,NN,A1,B1,EP,MP,N,WT                 INFR4370
          COMMON /PASS/ FIELD3,A62G,PCWER1,AKX,AKY,CIRK,P                   INFR4380
          COMMON /GRPH/ HORIZ(1000),VERT(1000),VERT1(1000)                  INFR4390
          AKX = B                                                           INFR4400
          IF(ABS(AKX).LT.1.E-40) AKX = 1.E-40                               INFR4410
          AKY = WT*A                                                        INFR4420
          FUN = FIELD(P)                                                    INFR4430
          RETURN                                                            INFR4440
          END                                                               INFR4450
          FUNCTION AGI(QQ)                                                  INFR4460
          COMMON /ARGA62/ C2,D2,EPS2,M2,NMAX2,AA,BB,EPS,M,NMAX,WT           INFR4470
          DIMENSION SA12(20),SB12(20),SU12(20),SW12(20),SV12(20),           INFR4480
         CFV2(20),B12(20),SFV2(20),SFU2(20),SFW2(20),SAG12(20)              INFR4490
          DATA (TEM=0.77459666924148)                                       INFR4500
          DATA (TEM1=0.2254033075852)                                       INFR4510
          DATA (C01=0.55555555555556)                                       INFR4520
          DATA (C02=0.88888888883889)                                       INFR4530
          AGI=0.    $N=-1    $A=AA    $B=BB    $BMA=B-A    $BPA=B+A         INFR4540
          VO=0.5*BPA     $UO=0.5*TEM*BMA      $WO=CO+VO     $UO=VO-UO      INFR4550
          FUO=AGI2(UO)                                                      INFR4560
          FVO=AGI2(VO)     $FWO=AGI2(WO)     $M=3                           INFR4570
          AGS=(C02*FVO+C01*(FUO+FWO))*0.5*BMA                               INFR4580
          EPSR = EPS*AGS                                                    INFR4590
     70 N=N+2    $IF(N.LE.NMAX) 71,72                                       INFR4600
     72 WRITE (3,99) N,A,B                                                  INFR4610
     99 FORMAT (17H N AND INTERVAL  ,I10,5X,2E16.7,7H  OUTER)               INFR4620
          N=N-2                                                             INFR4630
          GO TO 73                                                          INFR4640
     71 N1=N+1      $SA12(N1)=A1=A+TEM1*BMA    $W1=A+0.2*BMA    $U1=A+A1-W1  INFR4650
          SB12(N1)=B1=BPA-A1    $SU12(N1)=U2=W1+W1-UO                       INFR4660
          SW12(N1)=W2=B1-U2+A1      $SW12(N)=W3=B1+W1-A                     INFR4670
          SU12(N)=U3=B1+U1-A      $SV12(N1)=VO     $SV12(N)=WO              INFR4680
          SFV2(N1)=FVO      $SFV2(N)=FWO      $SB12(N)=B                    INFR4690
          SA12(N)=B1                                                        INFR4700
          FU1=AGI2(U1)     $FW1=AGI2(W1)     $FU2=SFU2(N1)=AGI2(U2)         INFR4710
          FU3=SFU2(N)=AGI2(U3)     $FW2=SFW2(N1)=AGI2(W2)                   INFR4720
          FW3=SFW2(N)=AGI2(W3)          $M=M+6                              INFR4730
          AG11=(C02*FUO+C01*(FU1+FW1))*0.5*(A1-A)                           INFR4740
          AG12=SAG12(N1)=(C02*FVO+C01*(FU2+FW2))*0.5*(B1-A1)                INFR4750
          AG13=SAG12(N)= (C02*FWO+C01*(FU3+FW3))*0.5*(B-B1)                 INFR4760
          AGI=AG11+AG12+AG13                                                INFR4770
          WRITE (3,34) A1,B1,AGI,AGS                                        INFR4780
     34 FORMAT (2X,10HINTERVAL   ,2E16.7,13H  ESTIMATES  ,2E16.7)           INFR4790
C         ABSOLUTE ACCURACY                                                 INFR4800
          IF(ABSF(ABSF(AGI)-ABSF(AGS)).LE.EPSR) 73,74                       INFR4810
C         RELATIVE ACCURACY                                                 INFR4820
C         IF(ABSF((ABSF(AGI)-ABSF(AGS))/AGI).LE.EPS) 73,74                  INFR4830
     74 AGS=AG11    $B=A1   $VO=CO    $UO=U1    $WO=W1    $FVO=FUO          INFR4840
          FUO=FU1     $FWO=FW1     $BMA=B-A      $BPA=B+A    $GO TO 70      INFR4850
     73 N=N-1       $IF(N.LE.0) 75,76                                       INFR4860
     76 AGI=AGI+AGI      $AGS=SAG12(N)     $B=SB12(N)    $A=SA12(N)         INFR4870
          BMA=B-A      $BPA=B+A      $VO=SV12(N)     $UO=SU12(N)            INFR4880
          WO=SW12(N)      $FVO=SFV2(N)     $FUO=SFU2(N)     $FWO=SFW2(N)    INFR4890
          GO TO 71                                                          INFR4900
     75 AGI=AGI+AGI       $RETURN                                           INFR4910
          END                                                               INFR4920
          FUNCTION AGI2(P)                                                  INFR4930
          COMMON /ARGA62/ AA,BB,EPS,M2,NMAX,RAD2,RAD,EQ,MQ,NQ,WT           INFR4940
          DIMENSION SA12(20),SB12(20),SU12(20),SW12(20),SV12(20),           INFR4950
         CFV2(20),B12(20),SFV2(20),SFU2(20),SFW2(20),SAG12(20)              INFR4960
```

```
      DATA (TEM=0.774596669241483)                                          INFR4970
      DATA (TEM1=0.225403330758517)                                         INFR4980
      DATA (C01=0.555555555555556)                                          INFR4990
      DATA (C02=0.888888888888889)                                          INFR5000
      WT = SQRT(RAD*RAD - P*P)    $ISW=0                                    INFR5010
      AGIT=0.    $N=-1    $A=AA    $B=BB    $BMA=B-A    $BPA=B+A           INFR5020
      V0=0.5*BPA     $U0=0.5*TEM*BMA      $W0=U0+V0     $U0=V0-U0          INFR5030
      FU0=FUN(U0,P)    $FV0=FUN(V0,P)     $FW0=FUN(W0,P)      $M2=3+M2      INFR5040
      AGS=(C02*FV0+C01*(FU0+FW0))*0.5*BMA                                   INFR5050
   70 N=N+2    $IF(N.LE.NMAX) 71,72                                         INFR5060
   72 WRITE (3,99) N,A,B                                                    INFR5070
   99 FORMAT (17H N AND INTERVAL ,I10,5X,2E16.7,7H  INNER)                  INFR5080
      N=N-2                                                                 INFR5090
      GO TO 73                                                              INFR5100
   71 N1=N+1      $SA12(N1)=A1=A+TEM1*BMA    $W1=A+0.2*BMA    $U1=A+A1-W1   INFR5110
      SB12(N1)=B1=BPA-A1    $SU12(N1)=U2=W1+W1-U0                           INFR5120
      SW12(N1)=W2=B1-U2+A1      $SW12(N)=W3=B1+W1-A                         INFR5130
      SU12(N)=U3=B1+U1-A      $SV12(N1)=V0     $SV12(N)=W0                  INFR5140
      SFV2(N1)=FV0      $SFV2(N)=FW0      $SB12(N)=B                        INFR5150
      SA12(N)=B1                                                            INFR5160
      FU1=FUN(U1,P)     $FW1=FUN(W1,P)     $FU2=SFU2(N1)=FUN(U2,P)          INFR5170
      FU3=SFU2(N)=FUN(U3,P)     $FW2=SFW2(N1)=FUN(W2,P)                     INFR5180
      FW3=SFW2(N)=FUN(W3,P)       $M2=M2+6                                  INFR5190
      AG11=(C02*FU0+C01*(FU1+FW1))*0.5*(A1-A)                               INFR5200
      AG12=SAG12(N1)=(C02*FV0+C01*(FU2+FW2))*0.5*(B1-A1)                    INFR5210
      AG13=SAG12(N)= (C02*FW0+C01*(FU3+FW3))*0.5*(B-B1)                     INFR5220
      AGI=AG11+AG12+AG13                                                    INFR5230
C     WRITE (3,34) A1,B1,AGI,AGS                                            INFR5240
C  34 FORMAT (2X,10HINTERVAL    ,2E16.7,13H  ESTIMATES  ,2E16.7             INFR5250
C    1 ,7H  INNER  )                                                       INFR5260
C     ABSOLUTE ACCURACY                                                     INFR5270
      IF(((ABSF(ABSF(AGI)-ABSF(AGS))*WT).LE.EPS).AND.(ISW.NE.0)) 73,74      INFR5280
C     RELATIVE ACCURACY                                                     INFR5290
C     IF(((ABSF((ABSF(AGI)-ABSF(AGS))/AGI).LE.EPS).AND.(ISW.NE.0)) 73,74    INFR5300
   74 AGS=AG11    $B=A1   $V0=U0    $U0=U1    $W0=W1    $FV0=FU0            INFR5310
      ISW=1                                                                 INFR5320
      FU0=FU1     $FW0=FW1     $BMA=B-A      $BPA=B+A    $GO TO 70          INFR5330
   73 N=N-1       $IF(N.LE.0) 75,76                                         INFR5340
   76 AGIT=AGIT+AGI      $AGS=SAG12(N)     $B=SB12(N)    $A=SA12(N)        INFR5350
      BMA=B-A      $BPA=B+A      $V0=SV12(N)     $U0=SU12(N)                INFR5360
      W0=SW12(N)      $FV0=SFV2(N)     $FU0=SFU2(N)     $FW0=SFW2(N)       INFR5370
      GO TO 71                                                              INFR5380
   75 AGI2=(AGIT+AGI)*WT       $RETURN                                      INFR5390
      END                                                                   INFR5400
      SUBROUTINE GRAPH(NG,RG,RX,RY)                                         INFR5410
      COMPLEX H3,H4,H5,H0,H11,SMONE,H5S                                     INFR5420
      COMPLEX EO,EE,ECCZ,EOCX,EOS,EOEEI,EEI,EECZ,EECX,AN2,WAC               INFR5430
      LOGICAL P                                                             INFR5440
      COMMON  WORK(11),XC0,Y00,Z00,WIDE,XTLL,DFREQ,FRQL,P1,P2,DK0,WOP0,     INFR5450
     1        XXI,PNLS(3),XNGL(2),XNEL(2),XDNO(39,4),NT,XDNE(39,4),NT1,     INFR5460
     2        CUT,X0,Y0,XLOC,BW,XLN,DFRQ,DK,WCP,XDN,XDA,XEDN,XEDA,          INFR5470
     3        DLOW,DHIGH,NR,STEP,ANAME,ISTAR,H1,H2,H2P,H2PP,H2PPP,          INFR5480
     4        H3,H4,H5,H5P,H6,H7,H8,H9,H10,H11,H12,H13,H14,XORS,XORC,       INFR5490
     5        AKXC                                                          INFR5500
      COMMON /BC/ AKV,AKVI,FRQS,EC,EOCZ,EOCX,ECS,ECEEI,EEI,EECZ,EECX,       INFR5510
     1            AN2,WAC                                                   INFR5520
      COMMON /CONST/ C,PI,SMONE,COMPR(13)                                   INFR5530
      COMMON /ARGA62/ C62,D62,EK,MM,NN,A1,B1,EP,MP,N,WT                     INFR5540
      COMMON /PASS/ FIELD3,A62G,POWER1,AKX,AKY,DIRK,P                       INFR5550
      COMMON /GRPH/ HORIZ(1000),VERT(1000),VERT1(1000)                      INFR5560
      DIMENSION PH3(2),PH4(2),PH5(2),PH6(2),PH11(2),PH5S(2),PSMONE(2)       INFR5570
      EQUIVALENCE (PH3,H3),(PH4,H4),(PH5,H5),(PH6,H6),(PH11,H11),           INFR5580
```

```
     1 (PH5S,H5S),(PSMLNE,SMLNE)                                        INFR5590
      YMAX = 0.                                                         INFR5600
      DO 10 I=1,NG                                                      INFR5610
      YMAX = AMAX1(YMAX,VERT(I))                                        INFR5620
      IF(P) YMAX = AMAX1(YMAX,VERT1(I))                                 INFR5630
   10 CONTINUE                                                          INFR5640
      CALL MAPS(HORIZ(1),HORIZ(NG),0.,YMAX)                             INFR5650
      CALL SETCH(1.,1.,1,0,3,0,0)                                       INFR5660
      CALL CRTBCD(RG)                                                   INFR5670
      CALL SETCH(32.,1.,0,C,2,0,0)                                      INFR5680
      CALL CRTBCD(RX)                                                   INFR5690
      CALL SETCH(1.,32.,0,0,2,1,0)                                      INFR5700
      CALL CRTBCD(RY)                                                   INFR5710
      CALL TRACE(HORIZ,VERT,NG)                                         INFR5720
      IF(P) CALL TRACE(HORIZ,VERT1,NG)                                  INFR5730
      CALL SETCH(65.,33.,1,C,1,0,0)                                     INFR5740
      FRQD = DFRQ/(2.*PI*C)                                             INFR5750
      FRQLL = FRQL/(2.*PI*C)                                            INFR5760
      WRITE (1C0,1000) P1,P2,BW,X0,Y0,XLOC,XLN,WOP,DK,XNOL,             INFR5770
     1       XNEL,XDN,XDA,XEDN,XEDA,XXI,FRQD,FRQLL                      INFR5780
 1000 FORMAT(6HP1    =,E11.3/6HP2    =,E11.3/6HBW    =,E11.3           INFR5790
     1 /6HX0    =,E11.3/6HY0    =,E11.3/6HXLOC =,E11.3                 INFR5800
     2 /6HXLN   =,E11.3/6HWOP   =,E11.3/6HDK    =,E11.3                INFR5810
     3 /6HNOL   =,E11.3/6HAOL   =,E11.3/6HNEL   =,E11.3                INFR5820
     4 /6HAEL   =,E11.3/6HNOD   =,E11.3/6HAOD   =,E11.3                INFR5830
     5 /6HNED   =,E11.3/6HAED   =,E11.3/6HXXI   =,E11.3                INFR5840
     6 /6HDFRQ  =,E11.3/6HFRQL  =,E11.3)                               INFR5850
      CALL FRAME                                                        INFR5860
      RETURN                                                            INFR5870
      END                                                               INFR5880
         SUBROUTINE SPLICE(NP,XT,YT,SP)                                 INFR5890
C                                                                       INFR5900
C     GENERATION OF THE SPLINE INTERPOLATION COEFFICIENTS               INFR5910
C                                                                       INFR5920
C     NP IS THE NUMBER OF (XT,YT) PAIRS                                 INFR5930
C     XT IS THE FWA OF TABULATED INDEPENDENT VARIABLE ARRAY             INFR5940
C     YT IS THE FWA OF TABULATED DEPENDENT VARIABLE ARRAY               INFR5950
C     SP IS THE ARRAY OF SPLINE COEFFICIENTS                            INFR5960
C                                                                       INFR5970
C     PARAMETER N1 SHOULD BE SET TO MAXIMUM NP TO BE USED               INFR5980
C     BLOCK SSSS WILL THEN BE DIMENSIONED FOR 2N1(N1+2) WORDS           INFR5990
C                                                                       INFR6000
      DIMENSION XT(2),YT(2),SP(2)                                       INFR6010
      COMMON/SSSS/W(40,40),B(40,40),Y(40),S(40),T(40),V(40)             INFR6020
C                                                                       INFR6030
      NT = NP                                                           INFR6040
      W(1,1) = 1./3.                                                    INFR6050
      W(1,2) = 1./6.                                                    INFR6060
      Y(1) = (YT(2)-YT(1))/(XT(2)-XT(1))**2                             INFR6070
      W(NT,NT-2) = -1./(XT(NT-1)-XT(NT-2))                              INFR6080
      W(NT,NT-1) = 1./(XT(NT-1)-XT(NT-2))+1./(XT(NT)-XT(NT-1))          INFR6090
      W(NT,NT) = -1./(XT(NT)-XT(NT-1))                                  INFR6100
      Y(NT) = 0.                                                        INFR6110
      NTP=NT-1                                                          INFR6120
      DO 30 K=2,NTP                                                     INFR6130
      W(K,K-1) = (XT(K)-XT(K-1))/6.                                     INFR6140
      W(K,K) = (XT(K+1)-XT(K-1))/3.                                     INFR6150
      W(K,K+1) = (XT(K+1)-XT(K))/6.                                     INFR6160
   30  Y(K) = (YT(K+1)-YT(K))/(XT(K+1)-XT(K))-(YT(K)-YT(K-1))/(XT(K)-   INFR6170
     1 XT(K-1))                                                         INFR6180
      CALL MLR(40,NT,NT,W,Y,SP,B,S,T,V)                                 INFR6190
      RETURN                                                            INFR6200
```

```
      END                                                                INFR6210
      SUBROUTINE SETEPS                                                  INFR6220
      COMPLEX H3,H4,H5,H6,H11,SMONE,H5S                                  INFR6230
      COMPLEX EO,EE,EOCZ,EOCX,EOS,EOEEI,EEI,EECZ,EECX,AN2,WAC            INFR6240
      LOGICAL P                                                          INFR6250
      COMMON  WORK(11),XCO,YOC,ZOO,WIDE,XTLL,DFREQ,FRQL,P1,P2,DKO,WOPO,  INFR6260
     1        XXI,PNLS(3),XNOL(2),XNEL(2),XDNO(39,4),NT,XDNE(39,4),NT1,   INFR6270
     2        CUT,XO,YO,XLOC,BW,XLN,DFRQ,DK,WOP,XDN,XDA,XEDN,XEDA,        INFR6280
     3        DLOW,DHIGH,NR,STEP,ANAME,ISTAR,H1,H2,H2P,H2PP,H2PPP,        INFR6290
     4        H3,H4,H5,H5P,H6,H7,H8,H9,H10,H11,H12,H13,H14,XORS,XORC,     INFR6300
     5        AKXC                                                       INFR6310
      COMMON /BC/ AKV,AKVI,FRQS,EO,EOCZ,EOCX,EOS,EOEEI,EEI,EECZ,EECX,    INFR6320
     1            AN2,WAC                                                INFR6330
      COMMON /CONST/ C,PI,SMONE,COMPR(13)                                INFR6340
      COMMON /ARGA62/ C62,D62,ER,MM,NN,A1,B1,EP,MP,N,WT                  INFR6350
      COMMON /PASS/ FIELD3,A62G,POWER1,AKX,AKY,DIRK,P                    INFR6360
      COMMON /GRPH/ HORIZ(1000),VERT(1000),VERT1(1000)                   INFR6370
      DIMENSION PH3(2),PH4(2),PH5(2),PH6(2),PH11(2),PH5S(2),PSMONE(2)    INFR6380
      EQUIVALENCE (PH3,H3),(PH4,H4),(PH5,H5),(PH6,H6),(PH11,H11),        INFR6390
     1 (PH5S,H5S),(PSMONE,SMONE)                                         INFR6400
   50 DO 53 J=2,NT                                                       INFR6410
      U2 = XDNO(J,1)-ABS(DFRQ)                                           INFR6420
      IF(U2) 53,54,54                                                    INFR6430
   53 CONTINUE                                                           INFR6440
      J = NT                                                             INFR6450
   54 U1 = ABS(DFRQ)-XDNO(J-1,1)                                         INFR6460
      U3 = XDNO(J,1)-XDNO(J-1,1)                                         INFR6470
      XDN = XDNO(J,2) + U2/U3*(XDNO(J-1,2)-XDNO(J,2))                    INFR6480
      XDA    = (XDNO(J,3)*U1+XDNO(J-1,3)*U2-                             INFR6490
     1          U1*U2*(XDNO(J-1,4)*(U3+U2)+XDNO(J,4)*(U3+U1))/6.)/U3     INFR6500
      DO 153 J=2,NT1                                                     INFR6510
      U2 = XDNE(J,1)-ABS(DFRQ)                                           INFR6520
      IF(U2) 153,154,154                                                 INFR6530
  153 CONTINUE                                                           INFR6540
      J = NT1                                                            INFR6550
  154 U1 = ABS(DFRQ)-XDNE(J-1,1)                                         INFR6560
      U3 = XDNE(J,1)-XDNE(J-1,1)                                         INFR6570
      XEDN =XDNE(J,2) + U2/U3*(XDNE(J-1,2)-XDNE(J,2))                    INFR6580
      XEDA   = (XDNE(J,3)*U1+XDNE(J-1,3)*U2-                             INFR6590
     1          U1*U2*(XDNE(J-1,4)*(U3+U2)+XDNE(J,4)*(U3+U1))/6.)/U3     INFR6600
      RETURN                                                             INFR6610
      END                                                                INFR6620
      SUBROUTINE ORIENT                                                  INFR6630
      COMPLEX H3,H4,H5,H6,H11,SMONE,H5S                                  INFR6640
      COMPLEX EO,EE,EOCZ,EOCX,EOS,EOEEI,EEI,EECZ,EECX,AN2,WAC            INFR6650
      LOGICAL P                                                          INFR6660
      COMMON  WORK(11),XCO,YOC,ZOO,WIDE,XTLL,DFREQ,FRQL,P1,P2,DKO,WOPO,  INFR6670
     1        XXI,PNLS(3),XNOL(2),XNEL(2),XDNO(39,4),NT,XDNE(39,4),NT1,   INFR6680
     2        CUT,XO,YO,XLOC,BW,XLN,DFRQ,DK,WOP,XDN,XDA,XEDN,XEDA,        INFR6690
     3        DLOW,DHIGH,NR,STEP,ANAME,ISTAR,H1,H2,H2P,H2PP,H2PPP,        INFR6700
     4        H3,H4,H5,H5P,H6,H7,H8,H9,H10,H11,H12,H13,H14,XORS,XORC,     INFR6710
     5        AKXC                                                       INFR6720
      COMMON /BC/ AKV,AKVI,FRQS,EO,EOCZ,EOCX,EOS,EOEEI,EEI,EECZ,EECX,    INFR6730
     1            AN2,WAC                                                INFR6740
      COMMON /CONST/ C,PI,SMONE,COMPR(13)                                INFR6750
      COMMON /ARGA62/ C62,D62,ER,MM,NN,A1,B1,EP,MP,N,WT                  INFR6760
      COMMON /PASS/ FIELD3,A62G,POWER1,AKX,AKY,DIRK,P                    INFR6770
      COMMON /GRPH/ HORIZ(1000),VERT(1000),VERT1(1000)                   INFR6780
      DIMENSION PH3(2),PH4(2),PH5(2),PH6(2),PH11(2),PH5S(2),PSMONE(2)    INFR6790
      EQUIVALENCE (PH3,H3),(PH4,H4),(PH5,H5),(PH6,H6),(PH11,H11),        INFR6800
     1 (PH5S,H5S),(PSMONE,SMONE)                                         INFR6810
      G = ((FRQL - (XDN*DFRQ + DK*C)/XNOL(1))/(FRQL - DFRQ))**2 - 1.     INFR6820
```

```
      IF (ABS(G).LT.1.E-10) GO TO 59                                    INFR6830
C     FUDGE CRYSTAL ORIENTATION TO ELIMINATE POLARIZATION               INFR6840
C     DEPENDANT EFFECTS FOR NON-ZERO WALK-OFF ANGLES.  FOR LARGE        INFR6850
C     WALK-OFF ANGLES THE E-RAY IS NEARLY PHASE-MATCHED AT LOW          INFR6860
C     FREQUENCIES IN WHICH CASE THIS IS A BETTER APPROXIMATION          INFR6870
C     THAN USING JUST THE O-RAY DFG AT THE CORRECT ORIENTATION.         INFR6880
C     FOR LARGE FREQUENCIES WHERE THE ORIENTATION ANGLE IS LARGE        INFR6890
C     THE EFFECT OF THIS CHANGE SHOULD BE SMALL.                        INFR6900
      XORS = 1.                                                         INFR6910
      XORC = 0.                                                         INFR6920
      XNEL(1) = XNOL(1)*SQRT(G+1.)                                      INFR6930
      GO TO 60                                                          INFR6940
   59 XORS = 1.                                                         INFR6950
      XORC = 0.                                                         INFR6960
      XNEL(1) = XNOL(1)                                                 INFR6970
   60 WRITE (3,1007) XNEL(1),G,XORS                                     INFR6980
 1007 FORMAT (31H OPTICAL E-RAY INDEX OF REF. = ,E12.5,5H G = ,         INFR6990
     1   E13.5,9H X(.)C = ,E13.5)                                       INFR7000
      RETURN                                                            INFR7010
      END                                                               INFR7020
      SUBROUTINE SETCON(KKK)                                            INFR7030
      COMPLEX H3,H4,H5,H6,H11,SMONE,H5S                                 INFR7040
      COMPLEX EO,EE,ECCZ,EOCX,EOS,ECEEI,EEI,EECZ,EECX,AN2,WAC           INFR7050
      LOGICAL P                                                         INFR7060
      COMMON  WORK(11),XCO,YOC,ZOO,WIDE,XTLL,DFREQ,FRQL,P1,P2,DKO,WOPO, INFR7070
     1        XXI,PNLS(3),XNOL(2),XNEL(2),XDNO(39,4),NT,XDNE(39,4),NT1,  INFR7080
     2        CUT,XO,YO,XLOC,EW,XLN,DFRQ,DK,WOP,XDN,XDA,XEDN,XEDA,       INFR7090
     3        DLOW,DHIGH,NR,STEP,ANAME,ISTAR,H1,H2,H2P,H2PP,H2PPP,       INFR7100
     4        H3,H4,H5,H5P,H6,H7,H8,H9,H10,H11,H12,H13,H14,XORS,XORC,    INFR7110
     5        AKXC                                                       INFR7120
      COMMON /BC/ AKV,AKVI,FRQS,EC,ECCZ,EOCX,EOS,ECEEI,EEI,EECZ,EECX,   INFR7130
     1            AN2,WAC                                               INFR7140
      COMMON /CONST/ C,PI,SMONE,CCMPR(13)                               INFR7150
      COMMON /ARGA62/ C62,D62,ER,MM,NN,A1,B1,EP,MP,N,WT                 INFR7160
      COMMON /PASS/ FIELD3,A620,POWER1,AKX,AKY,DIRK,P                   INFR7170
      COMMON /GRPH/ HORIZ(1000),VERT(1000),VERT1(1000)                  INFR7180
      DIMENSION PH3(2),PH4(2),PH5(2),PH6(2),PH11(2),PH5S(2),PSMONE(2)   INFR7190
      EQUIVALENCE (PH3,H3),(PH4,H4),(PH5,H5),(PH6,H6),(PH11,H11),       INFR7200
     1 (PH5S,H5S),(PSMONE,SMONE)                                        INFR7210
      AKV = DFRQ/C                                                      INFR7220
      AKVI = 1./AKV                                                     INFR7230
      FRQS = AKV*AKV                                                    INFR7240
      H1 = (PI*XXI*(DFRQ/C)**2*4./C)**2*P1*P2*1.E+19                    INFR7250
      H2 =  -.25*(BW**2*4.*(XLOC*C/(BW*FRQL))**2)                       INFR7260
      T7 = C/(FRQL*BW**2)                                               INFR7270
      H2P = -(XO*XO+YO*YO)/(BW*BW)                                      INFR7280
      H2PP = -2.*T7*XO*XLOC                                             INFR7290
      H2PPP = -2.*T7*YO*XLOC                                            INFR7300
      H5P = YO*T7/XNOL(1)                                               INFR7310
      H7 = XLOC*T7*C/(XNOL(1) *FRQL)                                    INFR7320
      H9 = T7*.5*C/(FRQL*XNOL(1)**2)                                    INFR7330
      AR = XDN*DFRQ/C                                                   INFR7340
      H11 = CMPLX(AR,XDA)                                               INFR7350
      H12 = H11*CMPLX(REAL(H11),-AIMAG(H11))                            INFR7360
      H4 = H11*C/ABS(DFRQ)                                              INFR7370
      H3 = H11*H11                                                      INFR7380
      H14 = (C/DFRQ)**2                                                 INFR7390
      EE = CMPLX(XEDN,XEDA*C/ABS(DFRQ))                                 INFR7400
      EE = EE*EE                                                        INFR7410
      EO = H3*H14                                                       INFR7420
      EEI = 1./EE                                                       INFR7430
      EOS = EO*EO                                                       INFR7440
```

```
      AR = WOP                                                          INFR7450
      AN2 = 1./(XORS**2/EE+XORC**2/EO)                                  INFR7460
      EOEEI = AN2*AN2*EEI/EC                                            INFR7470
      WAC = (EEI-1./EC)*XORS*XORC*AN2                                   INFR7480
      EOCX = EC*XORS                                                    INFR7490
      EOCZ = EC*XORC                                                    INFR7500
      EECX = EE*XORS                                                    INFR7510
      EECZ = EE*XORC                                                    INFR7520
      AKXC = T7*XLOC/H2*AMAX1(ABS(XO), ABS(XO+AR*XLN), ABS(YO))         INFR7530
      H8 = AR*T7/XNOL(1)                                                INFR7540
      H10 = .5*(AR/BW)**2                                               INFR7550
      H5S= AR*(.5*SMONE  -T7*XLOC)                                      INFR7560
      H5 = H5S -XO*T7/XNOL(1)                                           INFR7570
C     TNEL = THE EXTRA-ORDINARY INDEX OF REFRACTION FOR A WAVE          INFR7580
C              PROPAGATING AT AN ANGLE ARCSIN(XORC) FROM THE OPTIC AXIS INFR7590
C              FOR THE CASE OF NEGLEGIBLE ABSORPTION.                   INFR7600
      TNEL = SQRT(1./((XORS/XNEL(1))**2+(XORC/XNOL(1))**2))             INFR7610
      R = DK * REAL(H11)                                                INFR7620
      AI = XNOL(2)*XNEL(2) + XO*AR/(BW*BW)                              INFR7630
      H6 = CMPLX(R,AI)                                                  INFR7640
      H13 = (-PNLS(1)*XORC+PNLS(3)*XORS)                                INFR7650
      H1 = H1*(4./((XNOL(1)+1.)*(TNEL+1.)))**2                          INFR7660
      IF(KKK.NE.1) RETURN                                               INFR7670
      WRITE (3,2002) H1,H2,PH3,PH4,PH5,PH6,H7,H8,H9,H10,PH11,H12,H13,   INFR7680
     1     H14,T7,AR,(WORK(J),J=1,4),DFREQ,BW,XORS,XORC,                INFR7690
     2     XLN,XDN,XDA,H2P,H2PP,H2PPP,PH5S,H5P                          INFR7700
 2002 FORMAT(26H DUMP OF PRESET VALUES -  /(1X,8E14.4))                 INFR7710
      RETURN                                                            INFR7720
      END                                                               INFR7730
      FUNCTION FIELD(P)                                                 FLA   10
      COMPLEX H3,H4,H5,H6,H11,SMONE,H5S                                 FLA   20
      COMPLEX EO,EE,EOCZ,EOCX,EOS,EOEEI,EEI,EECZ,EECX,AN2,WAC           FLA   30
      LOGICAL P                                                         FLA   40
      COMMON  WORK(11),XCO,YOC,ZOO,WIDE,XTLL,DFREQ,FRCL,P1,P2,DKO,WOPO, FLA   50
     1        XXI,PNLS(3),XNOL(2),XNEL(2),XDNO(39,4),NT,XDNE(39,4),NT1, FLA   60
     2        CUT,XO,YO,XLOC,BW,XLN,DFRQ,DK,WOP,XDN,XDA,XEDN,XEDA,      FLA   70
     3        DLCW,CHIGH,NR,STEP,ANAME,ISTAR,H1,H2,H2P,H2PP,H2PPP,      FLA   80
     4        H3,H4,H5,H5P,H6,H7,H8,H9,H10,H11,H12,H13,H14,XORS,XORC,   FLA   90
     5        AKXC                                                      FLA  100
      COMMON /BC/ AKV,AKVI,FRCS,EC,ELCZ,ECCX,EOS,ECEEI,EEI,EECZ,EECX,   FLA  110
     1            AN2,WAC                                               FLA  120
      COMMON /CONST/ C,PI,SMONE,CCMPR(13)                               FLA  130
      COMMON /PASS/ FIELD3,A62G,POWER1,AKX,AKY,DIRK,QQ                  FLA  140
      COMMON /GRPH/ HORIZ(1000),VERT(1000),VERT1(1000)                  FLA  150
      DIMENSION PH3(2),PH4(2),PH5(2),PH6(2),PH11(2),PH5S(2),PSMONE(2)   FLA  160
      EQUIVALENCE (PH3,H3),(PH4,H4),(PH5,H5),(PH6,H6),(PH11,H11),       FLA  170
     1 (PH5S,H5S),(PSMONE,SMONE)                                        FLA  180
      COMPLEX CRP,CRM,AP,AM,BP,BM,RP,RM,PP,PM,TMT,QMT,FMT,AMMT,DP,DM,DF FLA  190
      COMPLEX DP,DM,EP,EM,AKZDP,AKZEP,AKZDM,AKZEM,EPT1,EPT2,EPT3,       FLA  200
     1        FMT1,FMT2,FMT3,CPL,CML,EPL,EML,GRPI,GRMI,AKZE1,AKZE2,     FLA  210
     2        GEM,GEP,Q,T2,T1                                           FLA  220
      DIMENSION  DP(3),DM(3),EP(3),EM(3),AKTV(2)                        FLA  230
      DIMENSION GRP(4),GRM(4),AP(4),AM(4),BP(4),BM(4),RP(4),RM(4),PP(2),FLA  240
     1          PM(2),TMT(4),QMT(4),FMT(4),AMMT(4)                      FLA  250
      LOGICAL DEBUG,QQ                                                  FLA  260
      DATA ICNT/0/                                                      FLA  270
      DIMENSION PT1(2),PT2(2),PT20(2)                                   FLA  280
      EQUIVALENCE (AKZOP,T1,PT1),(T2,PT2),(PT20,T20),(PT20,T21),        FLA  290
     1         (PT20(2),T22)                                            FLA  300
      COMPLEX T1,T2,T3,T4,T6,T20                                        FLA  310
      DIMENSION TT4(2),TT3(2)                                           FLA  320
      EQUIVALENCE  (T4,TT4,R1),(TT4(2),S1),(T3,TT3,R2),(TT3(2),S2)      FLA  330
```

```
      EQUIVALENCE (PT2,R3),(PT2(2),S3)                                      FLA  340
      DIMENSION PAKZEP(2),PAKZEM(2)                                         FLA  350
      EQUIVALENCE (PT1,R4),(PT1(2),S4)                                      FLA  360
      EQUIVALENCE (PAKZEP,R5,AKZEP),(PAKZEP(2),S5)                          FLA  370
      EQUIVALENCE (PAKZEM,R6,AKZEM),(PAKZEM(2),S6),(PT2,R3),(PT2(2),S3)     FLA  380
      COMPLEX WOFZ                                                          FLA  390
      ICNT = ICNT+1                                                         FLA  400
      DEBUG = (ICNT.LE.51)                                                  FLA  410
      U = AKY**2                                                            FLA  420
      AKXS = AKX*AKX                                                        FLA  430
      V = U+AKXS                                                            FLA  440
      DIRK = SQRT(1.-V*H14)                                                 FLA  450
C     T1 = THE Z COMPONENT OF K IN THE CRYSTAL                              FLA  460
      AKZOP = CSQRT(H3-V)                                                   FLA  470
C     T2 = 2.*GAMMA*ETA                                                     FLA  480
      T2 = SMONE  *(T1-H6) + H7*V - H5*AKX  +H5P*AKY                        FLA  490
      IF(DEBUG) WRITE(3,2301) U,V,PT1,PT2                                   FLA  500
C     T5 = GAMMA                                                            FLA  510
      T5 = H8*AKX +H9*V + H10                                               FLA  520
C     T3 = GAMMA**.5                                                        FLA  530
      T3 = SQRT(T5)                                                         FLA  540
C     T4 = GAMMA**.5*ETA                                                    FLA  550
      T4 = T2/(2.*T3)                                                       FLA  560
      T10 = H2P+H2PP*AKX+H2PPP*AKY-2.*AIMAG(AKZOP)*XLN                      FLA  570
C      FIELD = THE SQUARE OF THE MODULUS OF THE FIELD GENERATED             FLA  580
C              AT THE FAR END OF THE CRYSTAL W/O BOUNDARY CONDITIONS        FLA  590
C              (MATCHING LINEAR MEDIA) AND W/O THE EXP ABSORPTION TERM      FLA  600
      IF(DEBUG) WRITE(3,2304) T3,T4,T10                                     FLA  610
      DEL = XLN*T3                                                          FLA  620
      IF(ABS(DEL).LT.(.001)) GO TO 200                                      FLA  630
      FIELD =                PI/(4.*(REAL(T3)**2+AIMAG(T3)**2))             FLA  640
      T3  = DEL + T4                                                        FLA  650
      IF(SHIFT((R1.AND.R2.AND.4000000000C0C0CC0000B),1).EQ.1) 300,400       FLA  660
  200 T6 = (1.-EXP(-R3*XLN)*CMPLX(COS(S3*XLN),-SIN(S3*XLN)))/(T1*T2)        FLA  670
      IF ((ABS(S1)+ABS(S2)+ABS(R1)+ABS(R2)).LT.1.E-3)                       FLA  680
     1 T6 = XLN*(1.-DEL*(T4 + .33333333333333*DEL))/T1                      FLA  690
      FIELD = EXP(H2*V+T10)*(REAL(T6)**2+AIMAG(T6)**2)                      FLA  700
      GO TO 210                                                             FLA  710
  300 T10 = T10 - 2.*DEL*(DEL+2.*REAL(T4))                                  FLA  720
      T6 = -CONJG(T3)                                                       FLA  730
      T3 = -CONJG(T4)                                                       FLA  740
      T4 = T6                                                               FLA  750
  400 FIELD = FIELD*EXP(H2*V+T10)                                           FLA  760
      T20 = (T4-T3)*(T3+T4)                                                 FLA  770
      T6 = (WOFZ(-S1,R1)-EXP(T21)*CMPLX(COS(T22),SIN(T22))                  FLA  780
     1     *WOFZ(-S2,R2))/T1                                                FLA  790
      IF ((ABS(S1)+ABS(S2)+ABS(R1)+ABS(R2)).LT.1.E-3)                       FLA  800
     1 T6 = DEL*(1.-DEL*(T4 + .33333333333333*DEL))*1.12837916709551/T1    FLA  810
      FIELD = FIELD*(REAL(T6)**2+AIMAG(T6)**2)                              FLA  820
  210 IF(DEBUG) WRITE(3,2304) R2,S2,R1,S1,T6                                FLA  830
      IF(DEBUG) WRITE(3,2307) T3,T4,FIELD                                   FLA  840
      TOP1 = XORS*AKY                                                       FLA  850
      TOP2 = -XORC*AKY                                                      FLA  860
      TOP3 = XORC*AKX                                                       FLA  870
      OP(2) = TOP3     - XORS*AKZOP                                         FLA  880
      OPL = 1./CSQRT(OP(2)*OP(2)+U)                                         FLA  890
      OP(1) = OPL*TOP2                                                      FLA  900
      OP(2) = OP(2)*OPL                                                     FLA  910
      OP(3) = OPL*TOP1                                                      FLA  920
      AKZVP = AKV*DIRK                                                      FLA  930
      AKT = SQRT(V)                                                         FLA  940
      AKTV(1) = AKX/AKT                                                     FLA  950
```

```
      AKTV(2) = AKY/AKT                                                      FLA  960
      AP(1) = -OP(1)*AKTV(2)+OP(2)*AKTV(1)                                   FLA  970
      AP(2) =(AKZOP*(AKTV(1)*OP(1)+AKTV(2)*OP(2)) - AKT*CP(3))*AKVI          FLA  980
      ORP(1)= (AKZVP-AKZOP)/(AKZVP+AKZCP)                                    FLA  990
      ORP(2)= (-AKZCP+AKZVP*EC)/(AKZCP+AKZVP*EC)                             FLA 1000
      CAA = EXP(-XLN*S4)                                                     FLA 1010
      TPER = ((1.-REAL(ORP(1)))**2+AIMAG(CRP(1))**2)                         FLA 1020
     1         /(1.-(CAA*(REAL(ORP(1))**2+AIMAG(CRP(1))**2))**2)            FLA 1030
     2         *(REAL(AP(1))**2+AIMAG(AP(1))**2)                            FLA 1040
      TPL = ((1.-REAL(ORP(2)))**2+AIMAG(CRP(2))**2)                          FLA 1050
     1         /(1.-(CAA*(REAL(ORP(2))**2+AIMAG(ORP(2))**2))**2)            FLA 1060
     2         *(REAL(AP(2))**2+AIMAG(AP(2))**2)                            FLA 1070
      Q= PNLS(1)*OP(1)+PNLS(2)*OP(2)+PNLS(3)*OP(3)                           FLA 1080
      FIELD = FIELD*(REAL(Q)**2+AIMAG(Q)**2)                                 FLA 1090
      FIELD3 = FIELD*REAL(AKZCP)*AKVI                                        FLA 1100
     1               *(REAL(OP(1))**2 + AIMAG(CP(1))**2                      FLA 1110
     2               + REAL(OP(2))**2 + AIMAG(CP(2))**2                      FLA 1120
     3               + REAL(CP(3))**2 + AIMAG(CP(3))**2)                     FLA 1130
      FIELD = FIELD*(TPER + TPL)*DIRK                                        FLA 1140
      IF(.NOT.DEBUG) RETURN                                                  FLA 1150
      WRITE (3,1003) AKX,AKY ,AKXS,V,AKZCP,TCP1,TCP2,TCP3,OP,OPL,            FLA 1160
     X       AKTV,AKT                                                        FLA 1170
      WRITE (3,1001) CRP,AP,FIELD,FIELD3,CAA,TPER,TPL                        FLA 1180
      RETURN                                                                 FLA 1190
 1001 FORMAT(16H DATA AND VALUES / 9H   CRP = ,8E13.5/                       FLA 1200
     1 9H     AP = ,8E13.5/9H FIELD = ,8E13.5)                              FLA 1210
 1003 FORMAT( 6H AKX =,E13.5,6H AKY = ,E13.5,3X,E13.5,3X,E13.5/             FLA 1220
     1 9H AKZOP = ,5E13.5/9H    OP = ,8E13.5/                               FLA 1230
     4 9H  AKTV = ,3E13.5///)                                               FLA 1240
 2301 FORMAT(20H FIELD DEBUG PRINT  ,10X,6E15.4)                            FLA 1250
 2302 FORMAT(1H  ,E14.4,2E15.4)                                             FLA 1260
 2304 FORMAT(6E15.4)                                                        FLA 1270
 2307 FORMAT(5E15.4)                                                        FLA 1280
      END                                                                   FLA 1290
*     FORTRAN            COMPLEX ERROR FUNCTION                           FLA 1300
      COMPLEX FUNCTION WOFZ(U,V)                                            FLA 1310
C     COMPLEX ERROR FUNCTION      W.GAUTSCHI    ALGORITHM 363               FLA 1320
C     COMM. ACM  VOL 12  NO 11  NOV  1969  PAGE 635                        FLA 1330
C     EFFICIENT COMPUTATION OF THE COMPLEX ERROR FUNCTION                   FLA 1340
C     WALTER GAUTSCHI  SIAM JR. NUMERICAL ANALYSIS VOL 7 NO 1               FLA 1350
C     MARCH 1970  PAGE 187  THEORY  NUMERICAL DEVELOPMENT RESULTS           FLA 1360
      REAL IM,LAMBDA                                                        FLA 1370
      INTEGER CAPN,B                                                        FLA 1380
C     W(Z)=EXP(-Z*Z)ERFC(-IZ)      Z=X+IY    X>0.  Y>0.  ACCURACY 10 DECFLA 1390
      DIMENSION DDC(2)                                                      FLA 1400
      EQUIVALENCE (DDC,WOFZ,RE),(DDC(2),IM)                                 FLA 1410
      X = ABS(U)                                                            FLA 1420
      Y = ABS(V)                                                            FLA 1430
      IF((Y.LT.4.29).AND.(X.LT.5.33))55,1                                   FLA 1440
   55 S=(1.-Y/4.29)*SQRTF(1.-X*X/28.41)                                     FLA 1450
           H=1.6*S  $H2=H+H  $CAPN=6+23*S  $NU=9+21*S  $GO TO 2             FLA 1460
    1 H=0.  $CAPN=0  $NU=8                                                  FLA 1470
    2 IF(H.GT.0.)  LAMBDA=H2**CAPN                                          FLA 1480
      IF((H.EQ.0.).OR.(LAMBDA.EQ.0.))54,3                                   FLA 1490
   54 B=1  $GO TO 4                                                         FLA 1500
    3 B=0                                                                   FLA 1510
    4 R1=R2=S1=S2=0.    $NU1=NU+1   $DO 5 NKL=1,NU1  $N=NU1-NKL $NP1=N+1FLA 1520
      T1=Y+H+NP1*R1   $T2=X-NP1*R2  $C=.5/(T1*T1+T2*T2)  $R1=C*T1           FLA 1530
      R2=C*T2   $IF((H.GT.0.).AND.(N.LE.CAPN))53,5                          FLA 1540
   53 T1=LAMBDA+S1                                                          FLA 1550
      S1=R1*T1-R2*S2   $S2=R2*T1+R1*S2  $LAMBDA=LAMBDA/H2                  FLA 1560
    5 CONTINUE          $IF(B) 52,8                                         FLA 1570
```

```
52 TEMP=R1     $TEMM=R2     $GO TO 99                                    FLA 1580
 8 TEMP=S1   $TEMM=S2                                                   FLA 1590
99 IF(Y.EQ.0.) 59,9                                                     FLA 1600
59 RE=EXPF(-X*X)           $GO TO 6                                     FLA 1610
 9 RE=1.1283791670955l*TEMP                                             FLA 1620
 6 IM=1.1283791670955l*TEMM                                             FLA 1630
   IF(Y.LT.0.) WOFZ = -CONJG(WOFZ) + 2.*EXP(Y*Y-X*X)*                   FLA 1640
  1       CMPLX(COS(2.*X*Y),SIN(2.*X*Y))                               FLA 1650
   IM = IM*SIGN(1.,Y)                                                   FLA 1660
   RETURN                                                               FLA 1670
   END                                                                  FLA 1680
```

APPENDIX D

The plane wave square pulse laser fields are given by $\vec{E}_\ell(z,t) = \sum_p \vec{E}_{\ell p}(z,t)$ with

$$\vec{E}_{\ell p}(z,t) = \vec{\mathcal{E}}_{\ell p}\, 2\cos[\omega_0(t-zn_p/c)] \quad 0 < t-zn_p/c < \tau \qquad \text{(D1)}$$
$$= 0 \qquad \text{otherwise.}$$

If we make the simplifying assumptions that only the beating of optical polarizations j and k to generate far-infrared polarization i has non-zero tensor elements and that the optical pulses still overlap at $z = \ell$, then the solution to Eq. (42) is

$$\vec{E}_i(t,\ell) = (1-R_i)\sum_{m=0}^{\infty}[\vec{E}_i^{(s)}(t_m, z=\ell) - R_i \vec{E}_i^{(s)}(t_m - n_i\ell/c, z=0)] \qquad \text{(D2)}$$

with $t_m \equiv t-m(2n_i\ell/c)$,

$$\vec{E}_i^{(s)}(t,z=\ell) =$$

$$\begin{cases} 0 & t_r < t_j \\ -\vec{E}_i\,(n_i-n_j)^{-1}\cos(\omega_{-j}t_r) & t_j < t_r < \min(t_i, t_k+\tau) \\ 0 & t_i < t_r < t_k+\tau \\ -\vec{E}_i \begin{cases} (n_i-n_j)^{-1}\cos(\omega_{-j}t_r) \\ -(n_i-n_k)^{-1}\cos[\omega_{-k}(t_r-\tau)] \end{cases} & t_k+\tau < t_r < t_i \\ \vec{E}_i(n_i-n_k)^{-1}\cos[\omega_{-k}(t_r-\tau)] & \max(t_i, t_k+\tau) < t_r < t_i+\tau \\ 0 & t_i+\tau < t_r \quad , \end{cases}$$

and

$$E_i^{(s)}(t,z=0) =$$

$$\begin{cases} 0 & t < 0 \\ -\vec{E}_i\,(n_i+n_j)^{-1}\cos(\omega_{+j}t) & 0 < t < \min(\tau, t_i+t_j) \\ 0 & t_i+t_j < t < \tau \\ -\vec{E}_i \begin{cases} (n_i+n_j)^{-1}\cos(\omega_{+j}t) \\ -(n_i+n_k)^{-1}\cos[\omega_{+k}(t-\tau)] \end{cases} & \tau < t < t_i+t_j \\ \vec{E}_i(n_i+n_k)^{-1}\cos[\omega_{+k}(t-\tau)] & \max(\tau, t_i+t_j) < t < t_i+t_k+\tau \\ 0 & t_i+t_k+\tau < t \end{cases}$$

where

$$E_i \equiv \frac{8\pi}{n_i}\,\overleftrightarrow{\chi}^{NL}:\vec{E}_{\ell j}\vec{E}_{\ell k}(1-\delta_{jk}/2)$$

$$\omega_{\pm p} \equiv \omega_o\,\frac{(n_j-n_k)}{n_i \pm n_p} \quad (p=j \text{ or } k)$$

$$t_r \equiv t - n_i\ell/c$$

$$t_q \equiv n_q\ell/c \quad (q = i, j, \text{ or } k)$$

$$n_1 \equiv n_i(\omega); \quad n_j \equiv n_j(\omega_o); \quad n_k \equiv n_k(\omega_o)$$

and $n_i > n_j \geq n_k$ has been assumed.

APPENDIX E

Determination of the Least Squares Fitting Parameters $\vec{a}$ and Their Covariance Matrix

The minimization of χ^2 was based on a local linearization of $P(\omega,\theta,\vec{a})$ on the three components of $\vec{a}$: $P(\omega,\theta,\vec{a}_{n+1}) \cong P(\omega,\theta,\vec{a}_n) + \nabla_{\vec{a}} P(\omega,\theta,\vec{a}_n)\cdot(\vec{a}_{n+1}-\vec{a}_n)$. When $\vec{a}_n$ was sufficiently close to the solution $\vec{a}^*$, the standard linear solution of the resulting equations was used. Whenever this procedure gave a step, $\vec{a}_{n+1}-\vec{a}_n$, at an angle greater than $\cos^{-1}(.01) = 89.4°$ to the gradient (after scaling the components of $\vec{a}$) $\nabla_{\vec{a}} P(\omega,\theta,\vec{a}_n)$, a step along the above gradient was taken instead of the normal calculated step. After the solution, $\vec{a}^*$, was found by iterating the above procedure, the variance of the absorption coefficient was obtained by the standard linear Least squares fitting method (see B. W. Lindgren, Statistical Theory, (MacMillan, N.Y., 1962), p.386f) from the local linearization of $P(\omega,\theta,\vec{a})$ about $\vec{a}^*$ using the assumption that the variances of all our power measurements P_i at a given far-infrared frequency were equal to $\sigma_p^2(\omega)$, a value measured near the peak of each phase matching function.

Let $M_y \equiv \langle Y\ \tilde{Y} \rangle$

$$Y = \begin{pmatrix} P_1 - P(\omega, \theta_1, \vec{a}^*) \\ P_2 - P(\omega, \theta_2, \vec{a}^*) \\ \vdots \\ P_m - P(\omega, \theta_m, \vec{a}^*) \end{pmatrix}$$

$$\begin{pmatrix} \frac{\partial P}{\partial A}(\omega, \theta_1, a^*), & \frac{\partial P}{\partial \Delta_0}(\omega, \theta_1, \vec{a}^*), & \frac{\partial P}{\partial \Gamma}(\omega, \theta_1, \vec{a}^*) \\ \vdots & \vdots & \vdots \\ \frac{\partial P}{\partial A}(\omega, \theta_m, \vec{a}^*), & \cdots & \end{pmatrix}$$

Then following Lindgren:

$$M_{\vec{a}} = [(\tilde{X}X)^{-1}\tilde{X}]M_y[X(\tilde{X}X)^{-1}]$$

or if $M_y = \sigma_p^2(\omega)\ I$, then

$$M_{\vec{a}} = \sigma_p^2(\omega)\ (\tilde{X}X)^{-1}$$

where $\tilde{X}$ and $\tilde{Y}$ are the transposes of X and Y, respectively. The matrix $\tilde{X}X$ is adequately approximated by the matrix inverted at the last step of the iterative solution since $\nabla_{\vec{a}}\chi^2(\vec{a}) = 2\tilde{X}X \cdot (\vec{a} - \vec{a}^*)$.

FIGURE CAPTIONS

Fig. 1. Wavevector diagram for reflection of a plane wave incident from the vacuum side on the plane interface between vacuum and uniaxial crystal half-spaces: (a) crystal fills the right half-space; (b) crystal fills the left half space and (c) an equivalent diagram with the crystal on the right (Therefore, Fig. 1(b) is equivalent to Fig. 2(c) below.).

Fig. 2. Wavevector diagrams showing (a) boundary transmission and reflection of ordinary and extraordinary waves and its decomposition into (b) and (c) which describe two simpler cases of linear transmission and reflection of waves at an interface.

Fig. 3. Angular distribution of far-infrared power output at $\omega = 100\ cm^{-1}$ with the axial phase mismatch at its optimum value $\Delta k_a = -5.1\ cm^{-1}$, a near optimum focal spot radius $w = 25\ \mu m$, a zero walk-off angle $\zeta = 0$, and a crystal length $\ell = 1$ cm.

Fig. 4. Far-infrared power output at $\omega = 100\ cm^{-1}$ as a function of $\Delta k_a \ell$, assuming $\alpha = 0$, $\zeta = 0$, $w = 25\ \mu m$ and $\ell = 1$ cm.

Fig. 5. Far-infrared power output at $\omega = 100\ cm^{-1}$ as a function of $\Delta k_a \ell$ assuming $\alpha = 0$, $\zeta = 0$, $w = 0.2$ mm, and $\ell = 1$ cm.

Fig. 6. Far-infrared power output at $\omega = 100\ cm^{-1}$ as a function of the focal spot radius w for various walk-off angles ζ, $\alpha = 0$, and $\ell = 1$ cm. The calculation was done by always adjusting the axial phase mismatch Δk_a to its optimum value for maximum power output.

Fig. 7. Angular distribution of far-infrared power output at $\omega = 10\ cm^{-1}$ for $\Delta k_a = -4.0\ cm^{-1}$, $w = 25\ \mu m$, $\zeta = 0$, $\alpha = 0$, and $\ell = 1$ cm. The azimuth ϕ is defined by $\phi = \tan^{-1}(y/x)$.

Fig. 8. Far-infrared power output at $\omega = 10\ cm^{-1}$ as a function of $\Delta k_a \ell$ assuming $\alpha = 0$, $\zeta = 0$, $w = 25\ \mu m$, and $\ell = 1$ cm.

Fig. 9. Far-infrared power output at $\omega = 10\ cm^{-1}$ as a function of the focal spot radius w for various walk-off angles ζ, $\alpha = 0$, and $\ell = 1$ cm. The axial phase mismatch was always adjusted to its optimum value in the calculation.

Fig. 10. Angular distribution of the far-infrared power output at $\omega = 10\ cm^{-1}$ for various walk-off angles ζ assuming $w = 25\ \mu m$, $\alpha = 0$, $\ell = 1$ cm, and the optimum value of $\Delta k_a(\zeta)$. All curves were computed in the $\phi = 0$ plane.

Fig. 11. $P(\alpha)/P(\alpha = 0)$ versus α showing the reduction of output power due to far-infrared absorption. For each point on the curves for $\omega = 10\ cm^{-1}$ and $\omega = 100\ cm^{-1}$, $w = 25\ \mu m$, an optimum value of Δk_a, and an optimum location of the focal plane were used in the calculation. A corresponding curve calculated from the plane wave model is also shown for comparison.

Fig. 12. Optimum values of $\Delta k_a \ell$ versus the absorption coefficient α for the case of Fig. 11 with $\omega = 100\ cm^{-1}$ where Δk_a is the axial phase mismatch.

Fig. 13. Comparison of the results of the Gaussian distribution model, the plane wave model, and our present calculation for $\omega = 100\ cm^{-1}$, $\alpha = 0$, $\zeta = 0$, and $\ell = 1$ cm.

Fig. 14. Comparison of the results of the Gaussian distribution model and our present calculation for $\omega = 10\ cm^{-1}$, $\alpha = 0$, $\ell = 0$, and $\ell = 1$ cm.

Fig. 15. Phase-matched wavevector diagrams for (a) second harmonic generation and (b) difference frequency generation.

Fig. 16. Second harmonic power output as a function of $\Delta k_a \ell$ when $\Delta k_R^S \ell = 100$. [After Boyd and Kleinman, Jour. Appl. Phys. 39, 3597 (1968)].

Fig. 17. Second harmonic power output as a function of $\Delta k_a \ell$ when $\Delta k_R^S \ell = 5.68$. [After Boyd and Kleinman op.cit.]

Fig. 18. The far-infrared spectrum computed from Eq. (6) for a 2 psec. (full width at half-maximum) Nd laser pulse normally incident on a 1-mm $LiNbO_3$ slab. The crystal is oriented with the c-axis parallel to the plane surfaces of the slab and the laser pulse is polarized along the c-axis ($\chi_{33} = 1.57\times10^{-6}$ esu). The other parameters used in the calculation are $w_o = 0.017$ cm. (corresponding to a 4-mrad. divergence of the laser beam), L = 135 cm., $n_i^{(\omega)} = 5.05$ and $n_i^{(\omega_o)} = 2.2$. The solid and the dashed curves are computed with and without boundary conditions respectively.

Fig. 19. The far-infrared spectrum computed from Eq. (6) with the same laser parameters as in Fig. 1. Here, the 1-mm slab is oriented with the c-axis tilted at 16.8° away from the normal of the slab, and the a-axis is in the plane defined by the c-axis and the normal. The laser is polarized at 45° to the

plane, so that only $\chi_{24}^{NL} = 1.54 \times 10^{-6}$ esu is responsible for the difference-frequency signal with polarization perpendicular to the plane. With $\hat{i} = \hat{j}$ (along the b-axis) and $\hat{k}$ being the directions of polarizations of the ordinary and the extra-ordinary light propagating along $\hat{z}$ respectively, we have $n_i^{(\omega)} = 6.6$, $n_i^{(\omega_o)} = 2.2$, and $n_k^{(\omega_o)} = 2.193$.

Fig. 20. The electric field for the optical rectification case (as in Fig. 18). The optical input is a 2 psec square pulse and linear boundary reflections are ignored. Upper curve: field that travels back toward the laser ($z < 0$). Lower curve: field that propagates in the direction of the laser beam ($z > \ell$).

Fig. 21. The spectrum of the sum of the lower and first reflection of the upper curves in Fig. 20 illustrating the interference of these two fields.

Fig. 22. The backward ($z < 0$; upper curve) and forward ($z > \ell$; lower curve) wave electric fields for the o-ray, e-ray mixing case (as in Fig. 19). The optical input pulse is a 2 psec square pulse and linear boundary reflections are ignored.

Fig. 23. Wavevectors in non-collinear phase matching: (a) the phase matched case - $k_i = n_i\omega_i/c$; $\omega_3 = \omega_1 - \omega_2 \equiv \omega$ for difference frequency generation. (b) The unmatched case.

Fig. 24. Dual-frequency dye laser system. The Ruby laser beam was circularly polarized with a quarter-wave plate. The two output frequencies could be independently tuned from 8100 to 8400Å.

Fig. 25. Far-infrared bandwidth versus angular width of the phase matching function for 1.61 mm (solid line) and 1 cm (dashed line) thick $LiNbO_3$ samples used to generate o-ray far-infrared radiation in a type II collinear phase matching configuration at a 21 cm^{-1} difference frequency.

Fig. 26. Experimental measurement of the phase matching function for our 1.61 mm thick $LiNbO_3$ sample at 21 cm^{-1}. The solid curve is the theoretical phase matching function for a 3 cm^{-1} far-infrared bandwidth.

Fig. 27. O-ray absorption coefficient of $LiNbO_3$. The solid curve is a composite of Bosomworth's (below 70 cm^{-1}) and of Barker and Loudon's (above 70 cm^{-1}) o-ray absorption coefficients.

Fig. 28. Far-infrared peak power generated in $LiNbO_3$ versus difference frequency for three phase matching methods. The solid curves are the plane wave theory including the calculated dispersion of χ_{24} (collinear) or χ_{33} (non-collinear).

Fig. 29. Calculated far-infrared power vs. frequency for FCPM in $LiNbO_3$ with monochromatic lasers neglecting the dispersion of χ_{24}. The lower curve includes the exact boundary conditions discussed in chapter II; the upper curve is the power in the absence of all reflections. (a) Coaxial pump laser beams; (b) Laser beam axes .5 mm apart.

Fig. 30. Dispersion of $|\chi_{24}^{(2)}|^2$ in $LiNbO_3$. The circles are our experimental measurements. The solid curve is a multiple simple-harmonic-oscillator calculation based on the Raman cross sections of Kaminow and Johnston and the TO phonon oscillator strengths, frequencies, and linewidths of Barker and Loudon.

Fig. 31. Dye laser system used for non-collinear phase matching experiments in $LiNbO_3$.

Fig. 32. Schematic of the $LiNbO_3$ cube used for our non-collinear phase matching experiments.

Fig. 33. Dispersion of the electronic, r_e, and ionic, r_q, contributions to the linear electro-optic coefficient r_{42} of CdS from the Raman scattering data of Ralston et al.

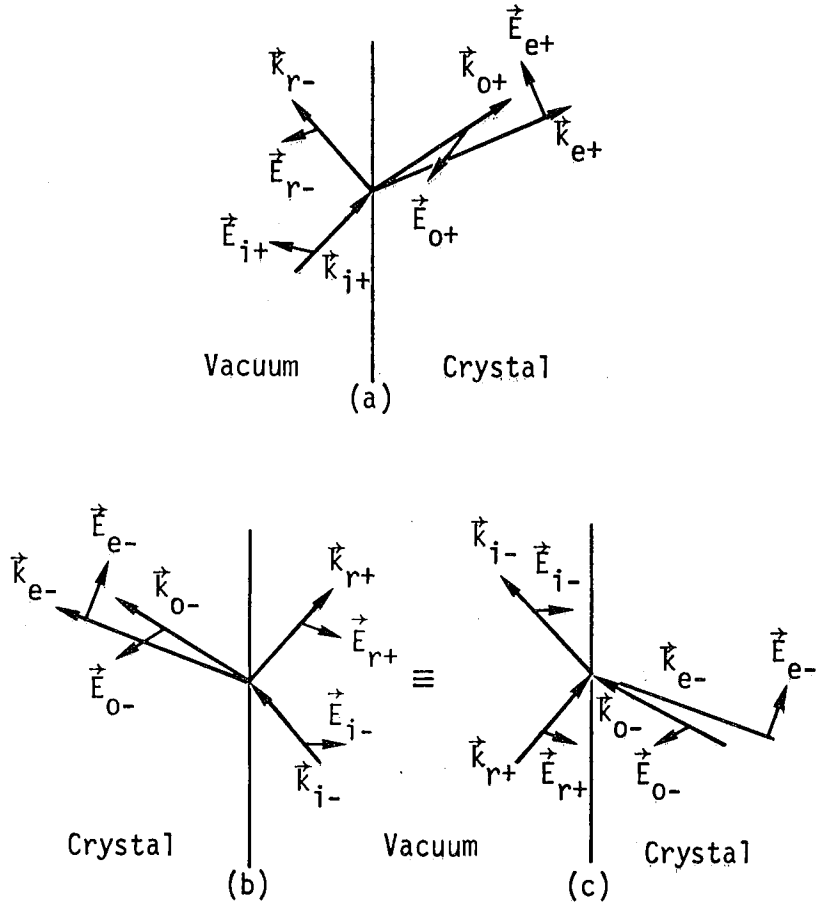
$\vec{k}_{r-}$
$\vec{E}_{r-}$
$\vec{E}_{i+}$
$\vec{k}_{i+}$
$\vec{E}_{e+}$
$\vec{k}_{o+}$
$\vec{k}_{e+}$
$\vec{E}_{o+}$
Vacuum
Crystal
(a)
$\vec{E}_{e-}$
$\vec{k}_{e-}$
$\vec{k}_{o-}$
$\vec{E}_{o-}$
$\vec{k}_{r+}$
$\vec{E}_{r+}$
$\vec{E}_{i-}$
$\vec{k}_{i-}$
Crystal
(b)
≡
$\vec{k}_{i-}$
$\vec{E}_{i-}$
$\vec{k}_{e-}$
$\vec{E}_{e-}$
$\vec{k}_{o-}$
$\vec{k}_{r+}$
$\vec{E}_{r+}$
$\vec{E}_{o-}$
Vacuum
Crystal
(c)

Fig. 1.

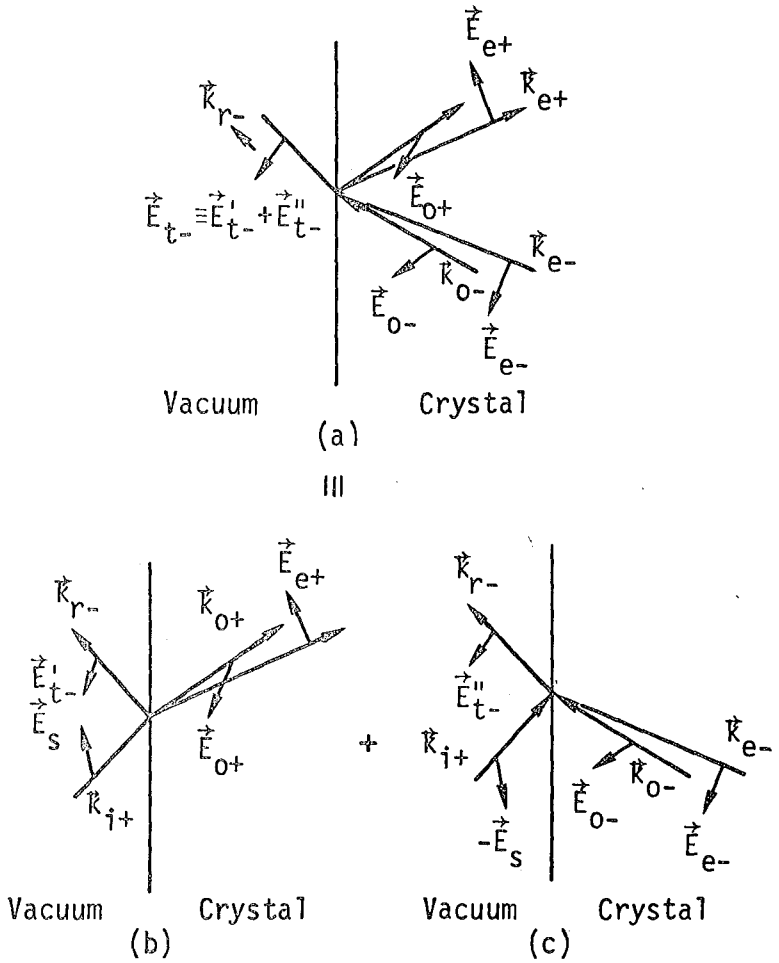

Fig. 2.

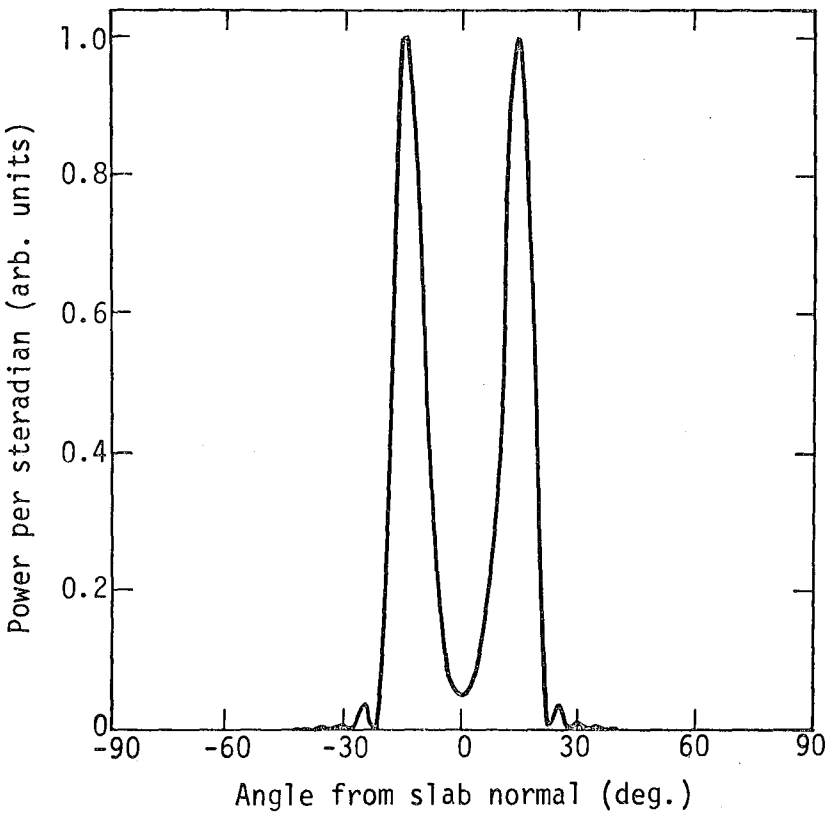
1.0
0.8
0.6
0.4
0.2
0
Power per steradian (arb. units)
-90
-60
-30
0
30
60
90
Angle from slab normal (deg.)

Fig. 3.

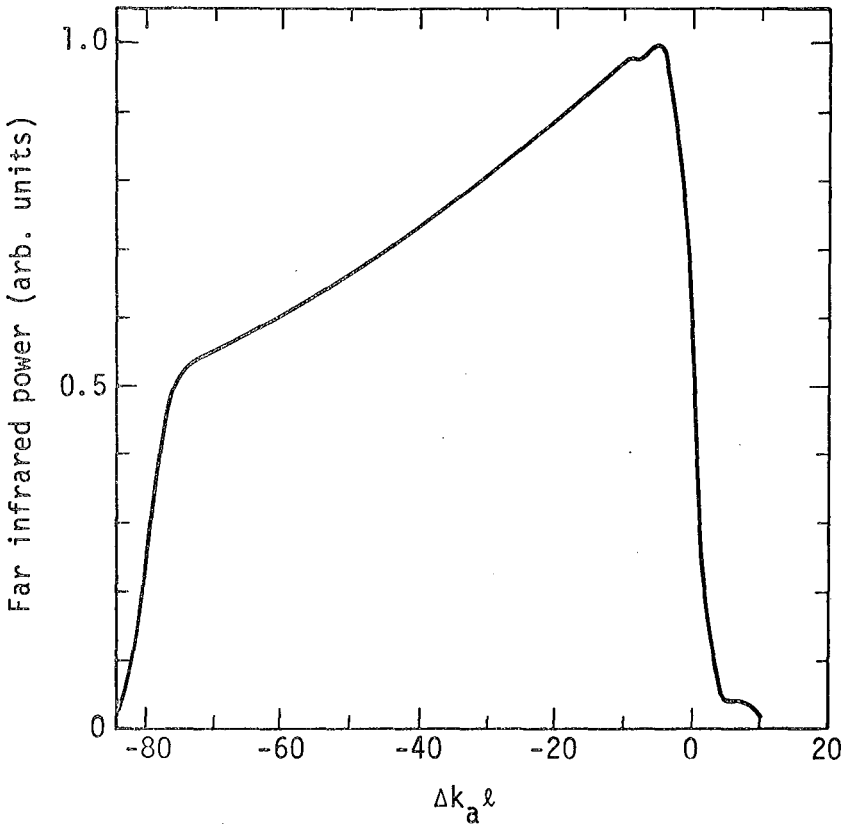

Fig. 4.

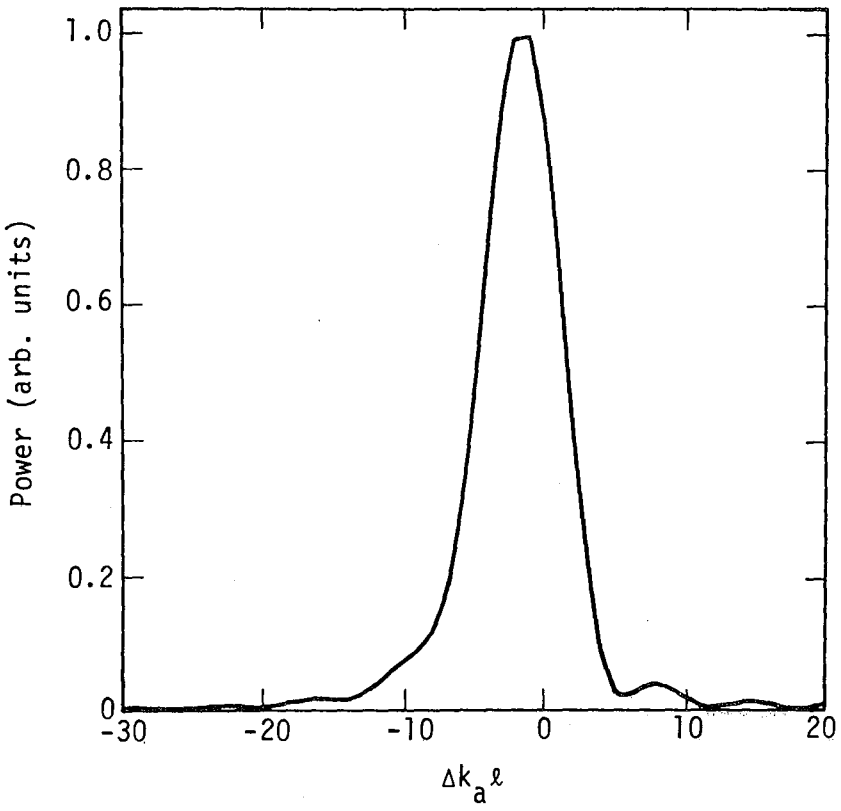

Fig. 5.

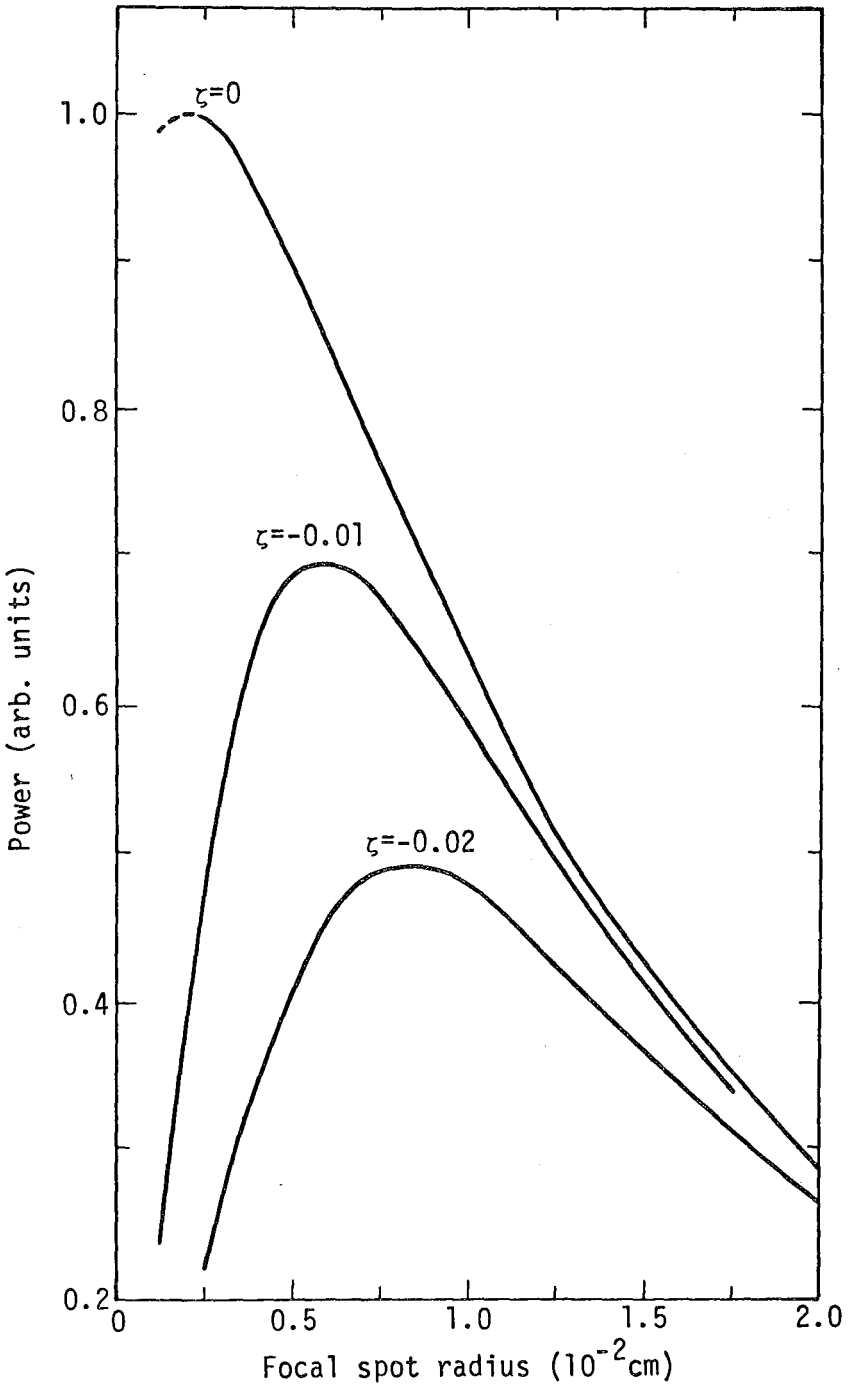

Fig. 6.

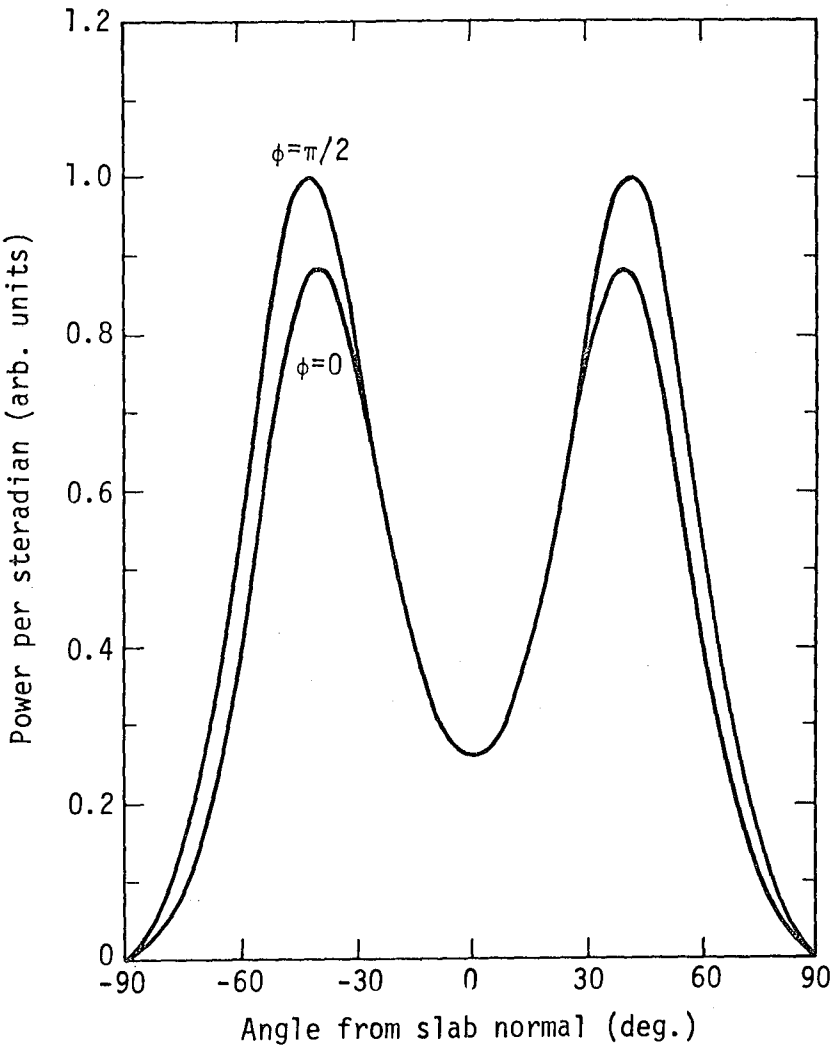
1.2
1.0
0.8
0.6
0.4
0.2
0
Power per steradian (arb. units)
φ=π/2
φ=0
-90
-60
-30
0
30
60
90
Angle from slab normal (deg.)

Fig. 7.

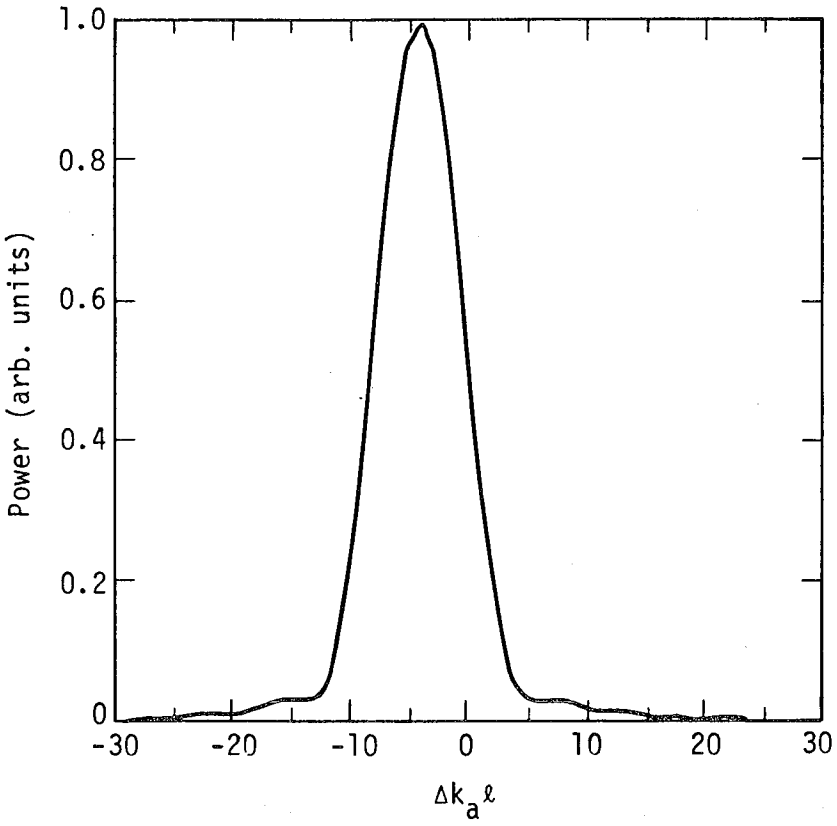

Fig. 8.

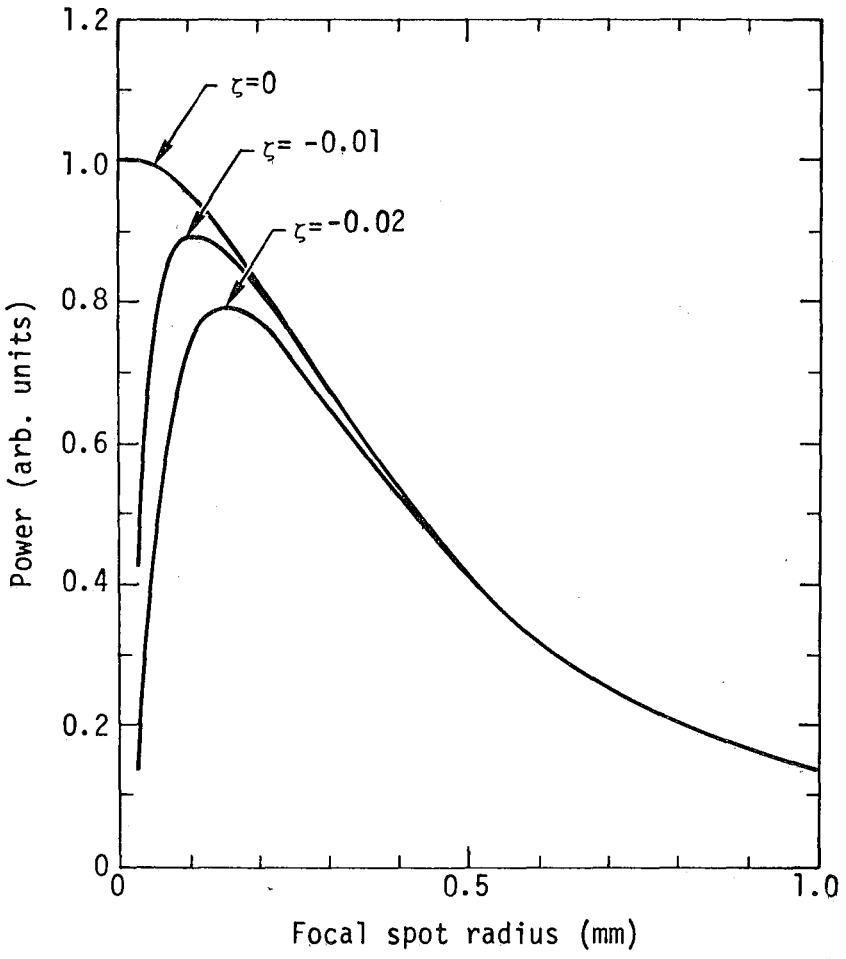
1.2
1.0
0.8
0.6
0.4
0.2
0
0
0.5
1.0
Power (arb. units)
Focal spot radius (mm)
ζ=0
ζ= -0.01
ζ=-0.02

Fig. 9.

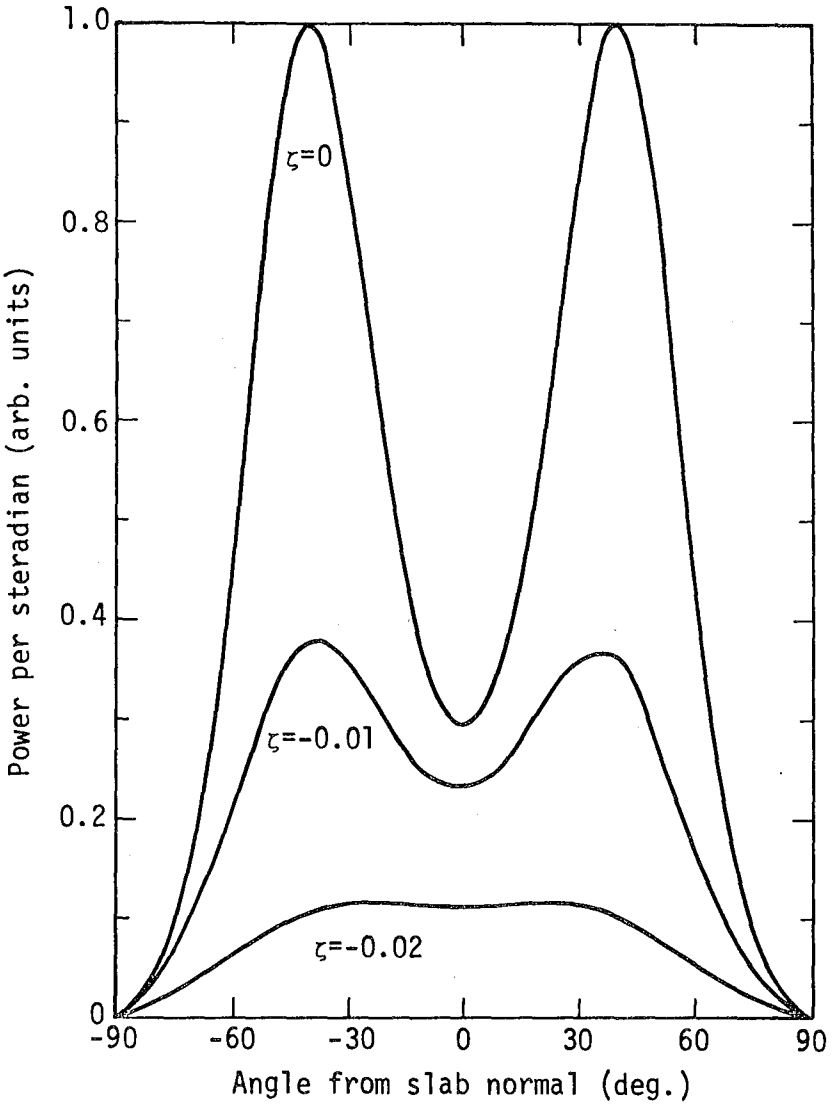

Fig. 10.

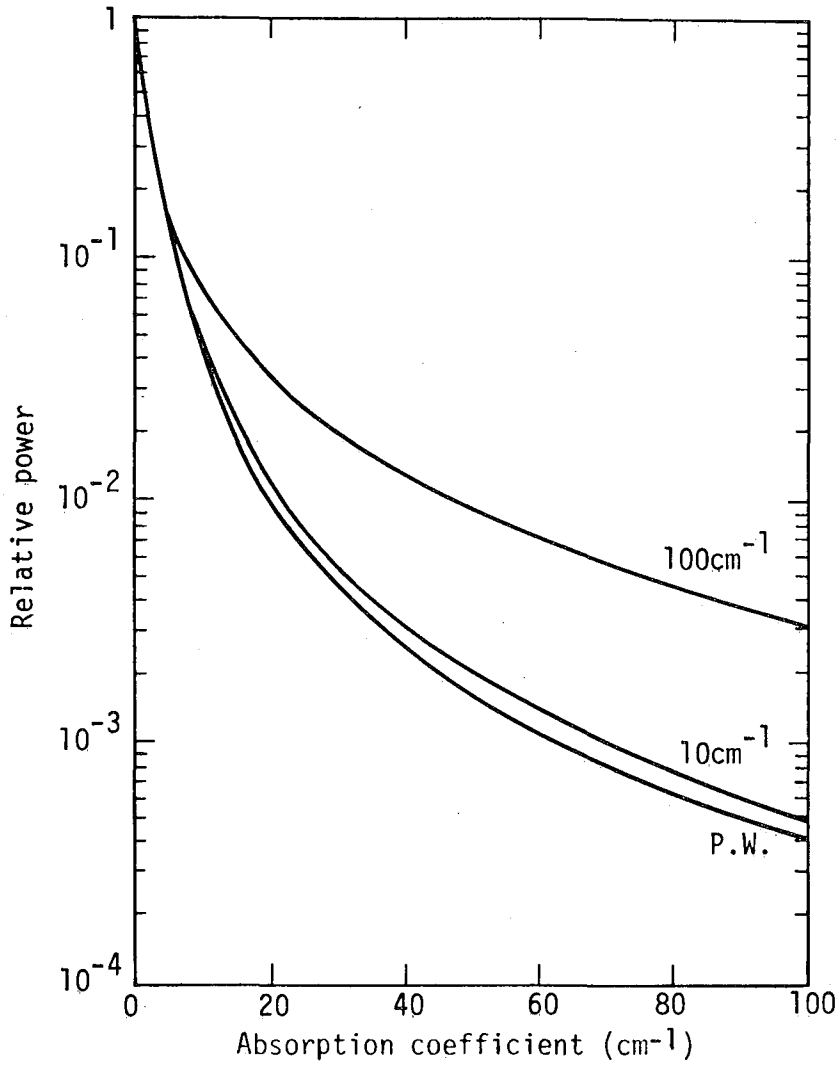
1
10^{-1}
10^{-2}
10^{-3}
10^{-4}
Relative power
100cm^{-1}
10cm^{-1}
P.W.
0
20
40
60
80
100
Absorption coefficient (cm^{-1})

Fig. 11.

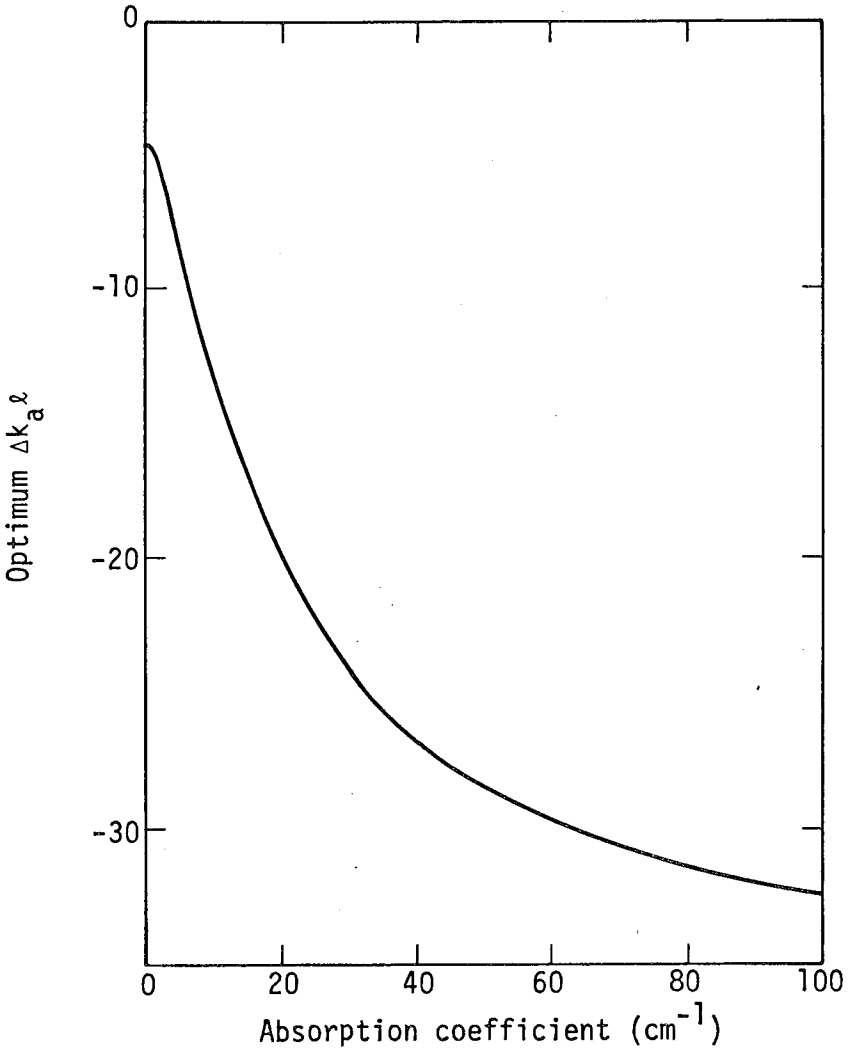

Fig. 12.

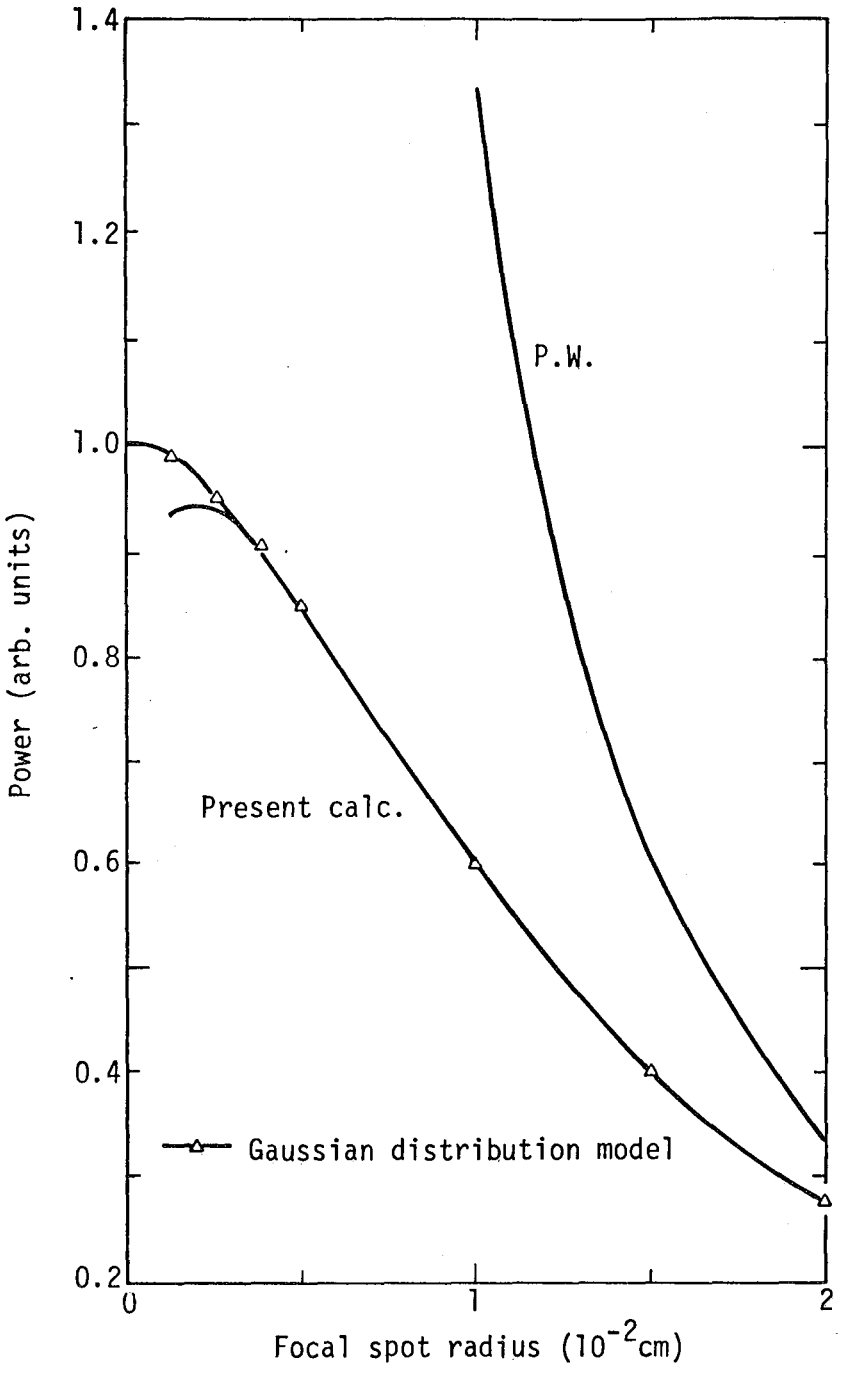
1.4
1.2
1.0
0.8
0.6
0.4
0.2
0
1
2
Power (arb. units)
Focal spot radius (10^{-2}cm)
P.W.
Present calc.
Gaussian distribution model

Fig. 13.

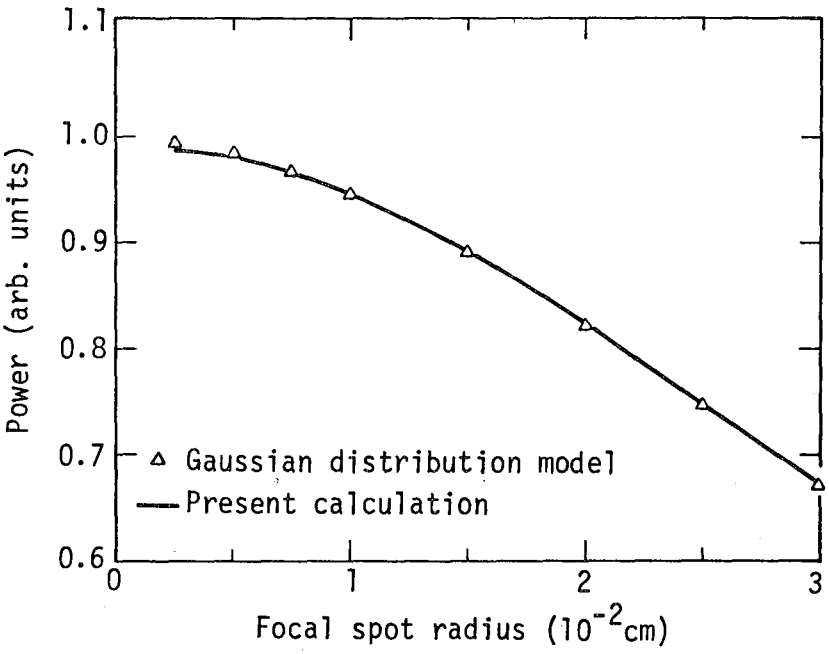

Fig. 14.

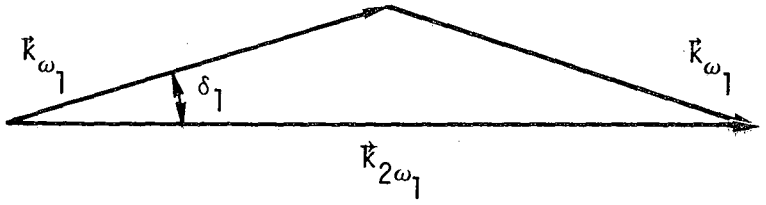
$\vec{k}_{\omega_1}$
δ_1
$\vec{k}_{\omega_1}$
$\vec{k}_{2\omega_1}$

(a)

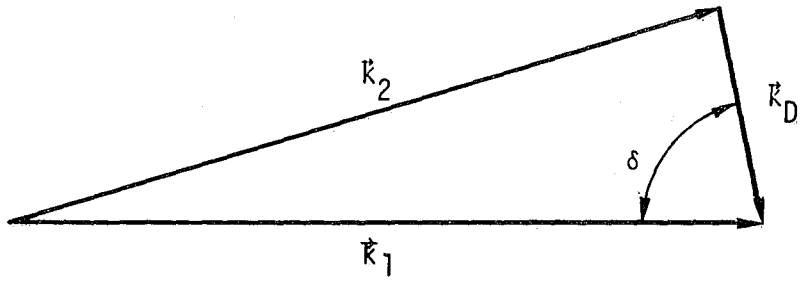
$\vec{k}_2$
$\vec{k}_D$
δ
$\vec{k}_1$

(b)

Fig. 15.

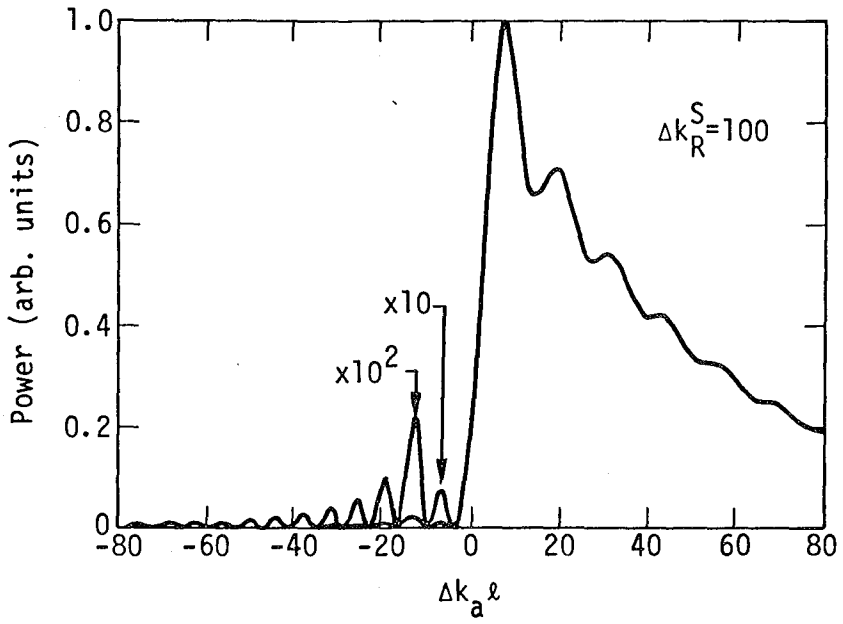

Fig. 16.

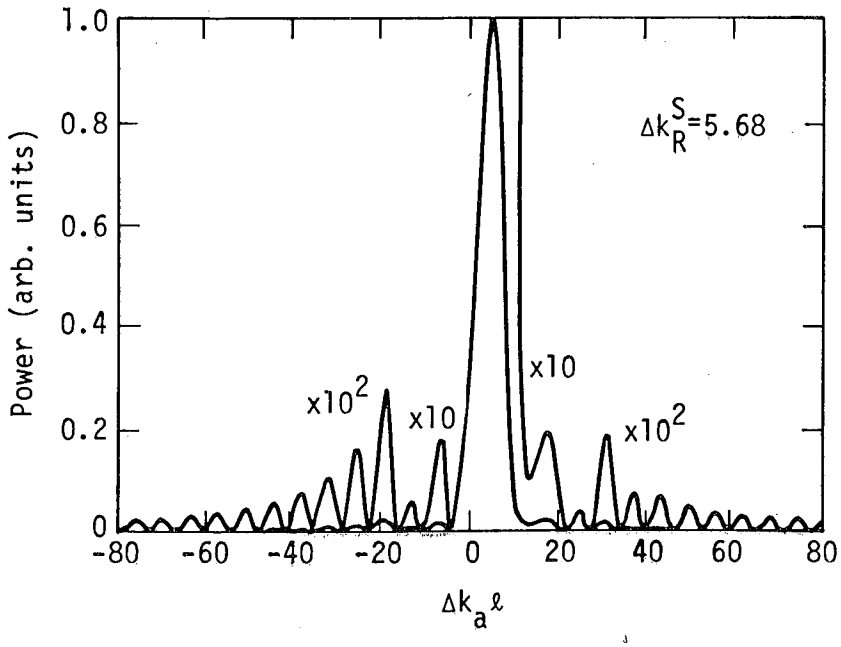
1.0
0.8
0.6
0.4
0.2
0
Power (arb. units)
Δk_R^S=5.68
x10^2
x10
x10
x10^2
-80
-60
-40
-20
0
20
40
60
80
$\Delta k_a \ell$

Fig. 17.

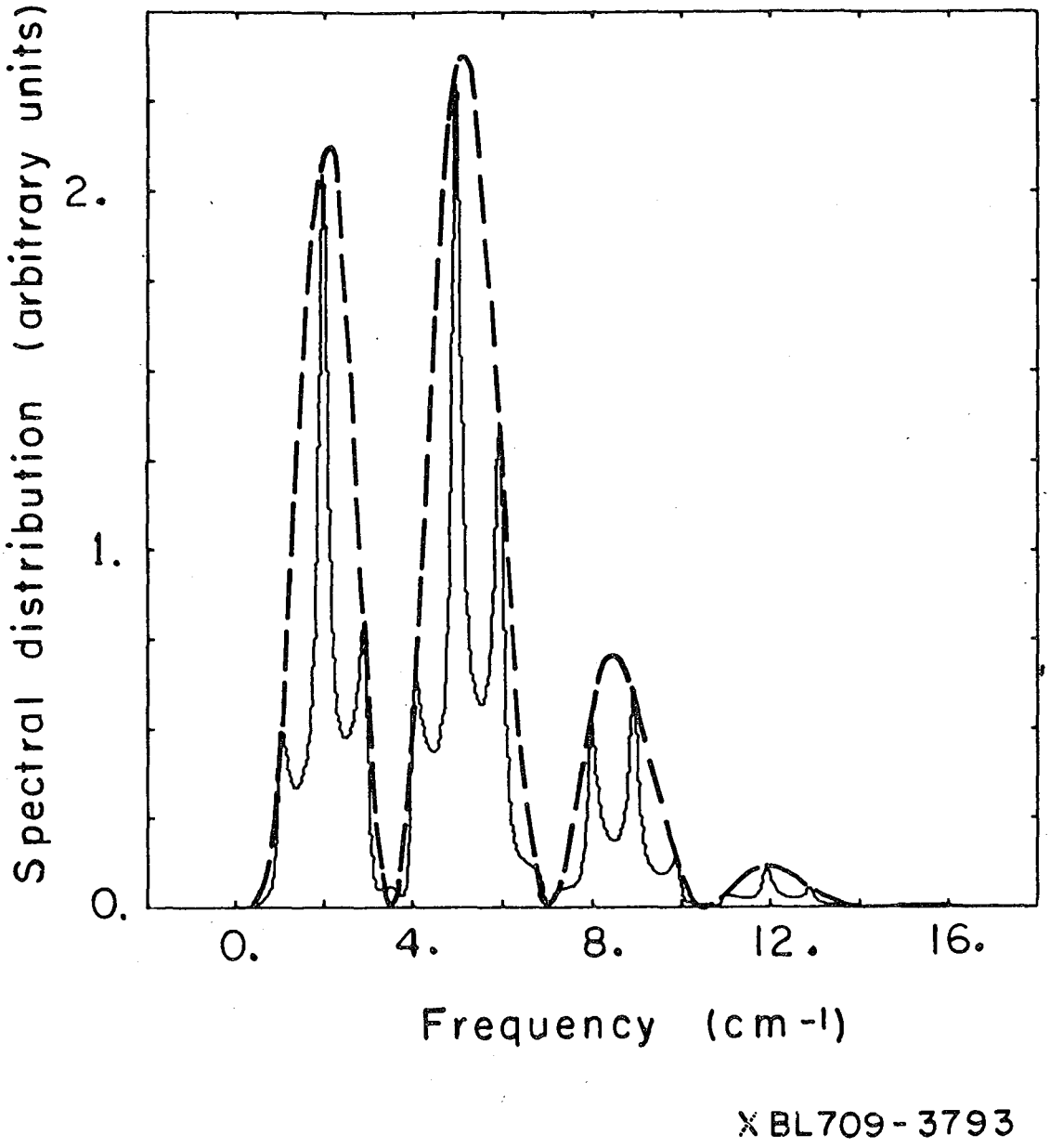

Fig. 18.

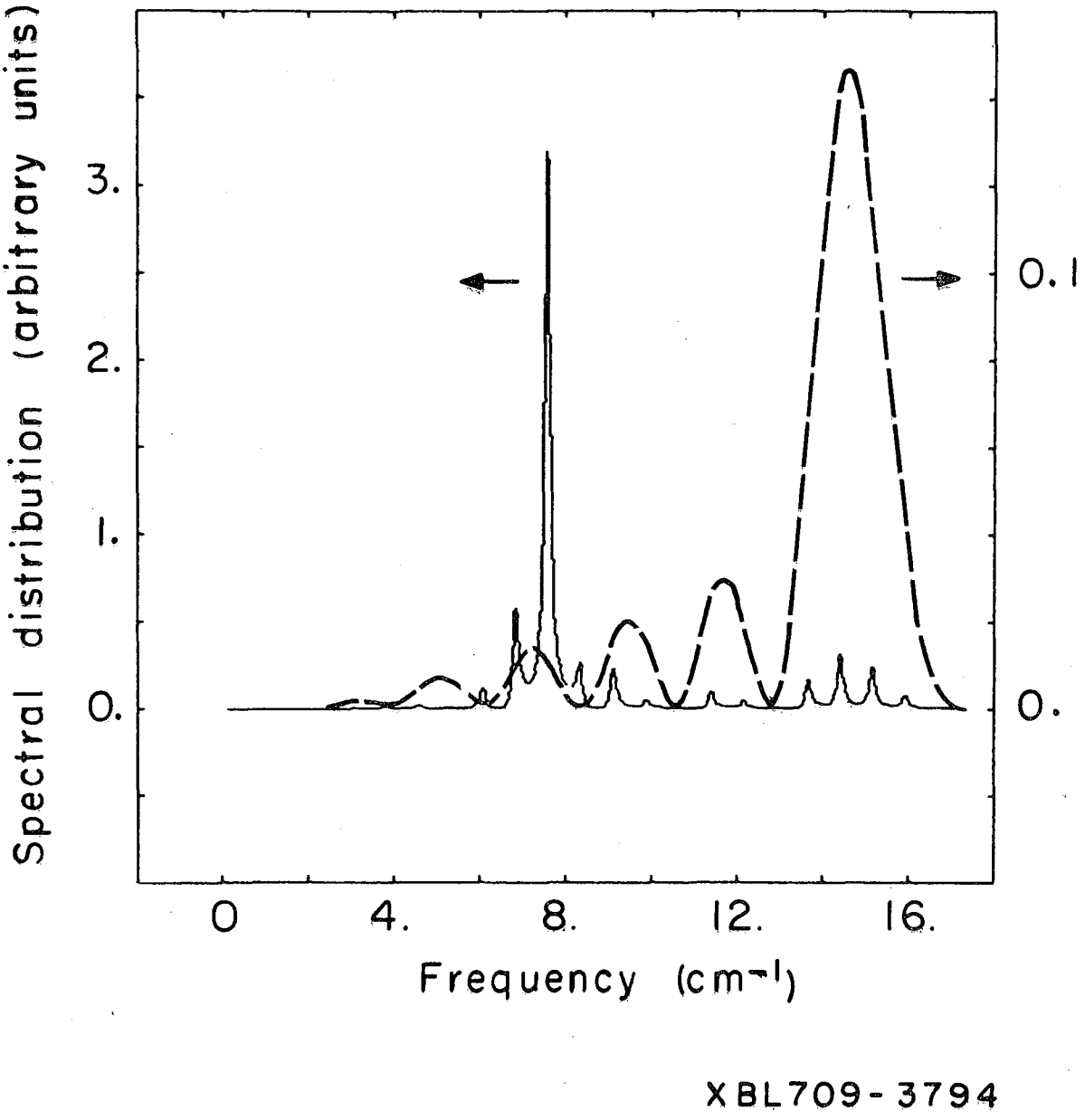
Spectral distribution (arbitrary units)
3.
2.
1.
0.
0.1
0.
0
4.
8.
12.
16.
Frequency (cm⁻¹)
XBL709-3794

Fig. 19.

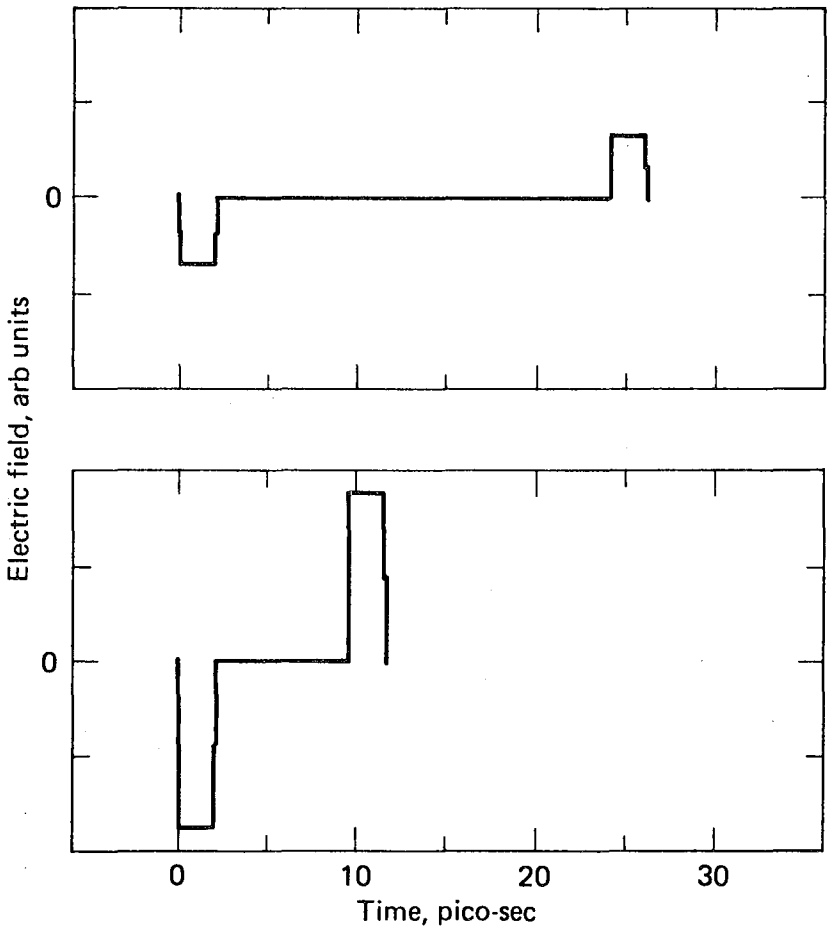

Fig. 20.

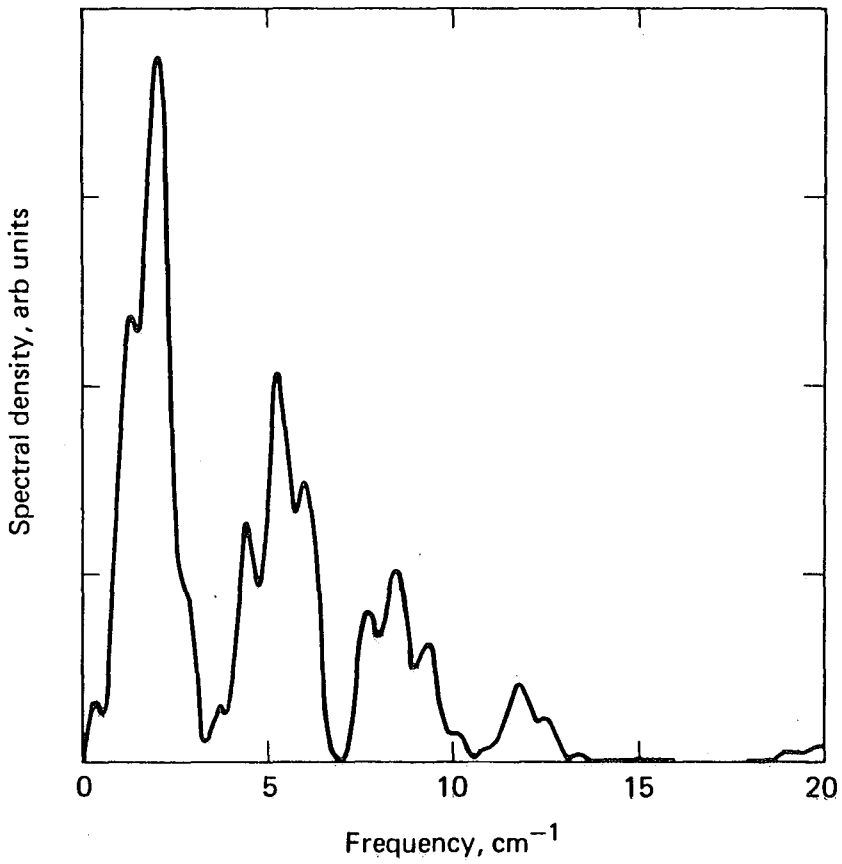

Fig. 21.

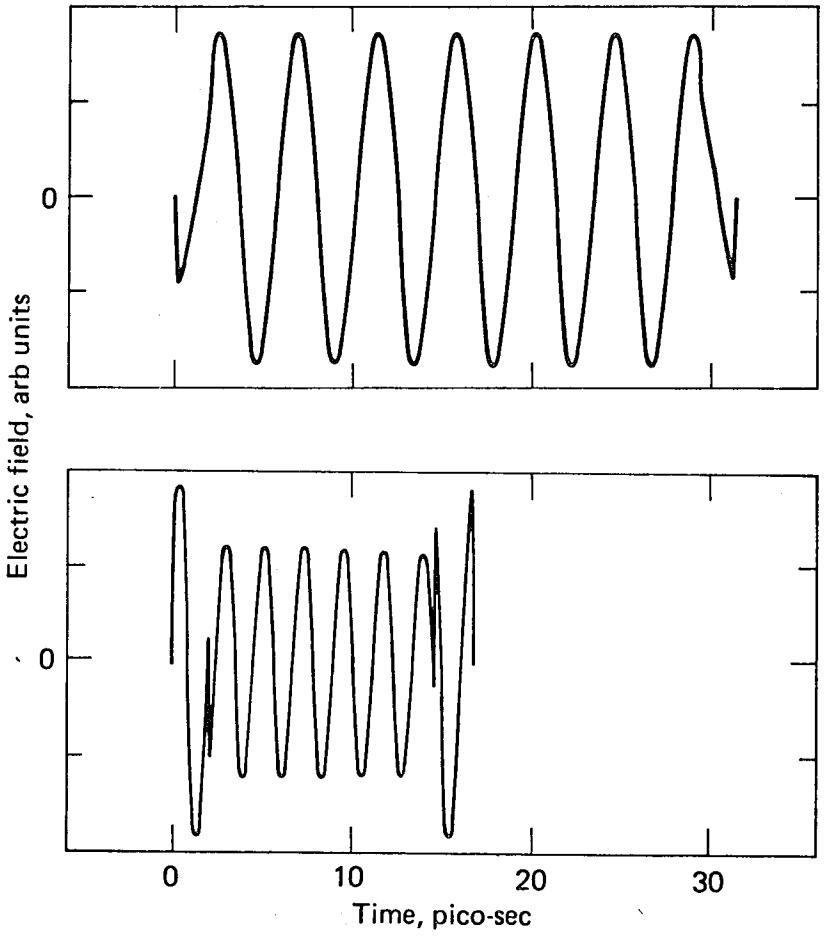

Fig. 22.

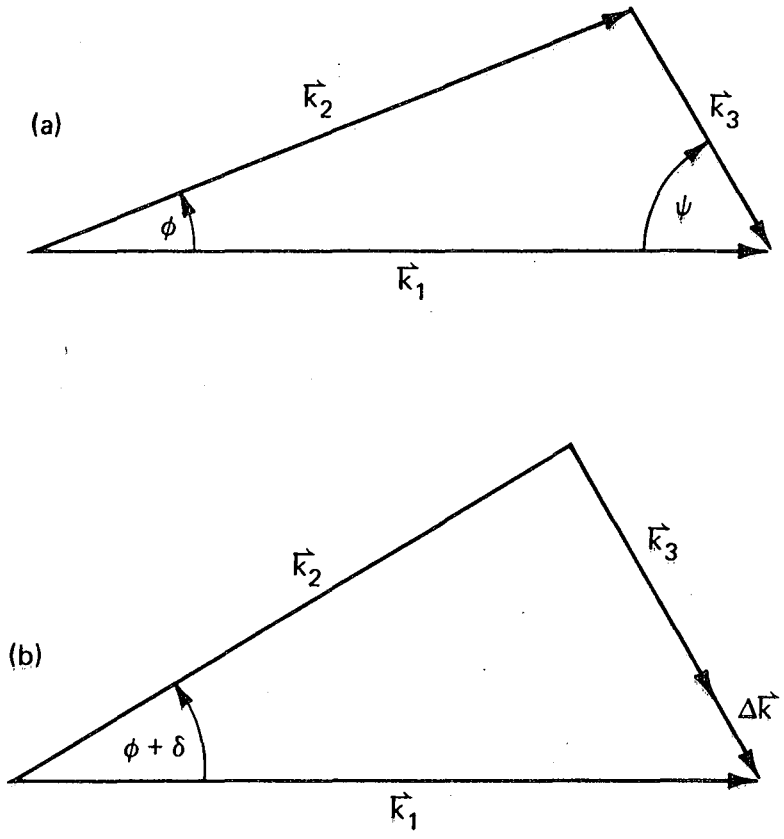
(a)
$\vec{k}_2$
$\vec{k}_3$
ϕ
ψ
$\vec{k}_1$
(b)
$\vec{k}_2$
$\vec{k}_3$
$\Delta\vec{k}$
$\phi + \delta$
$\vec{k}_1$

Fig. 23.

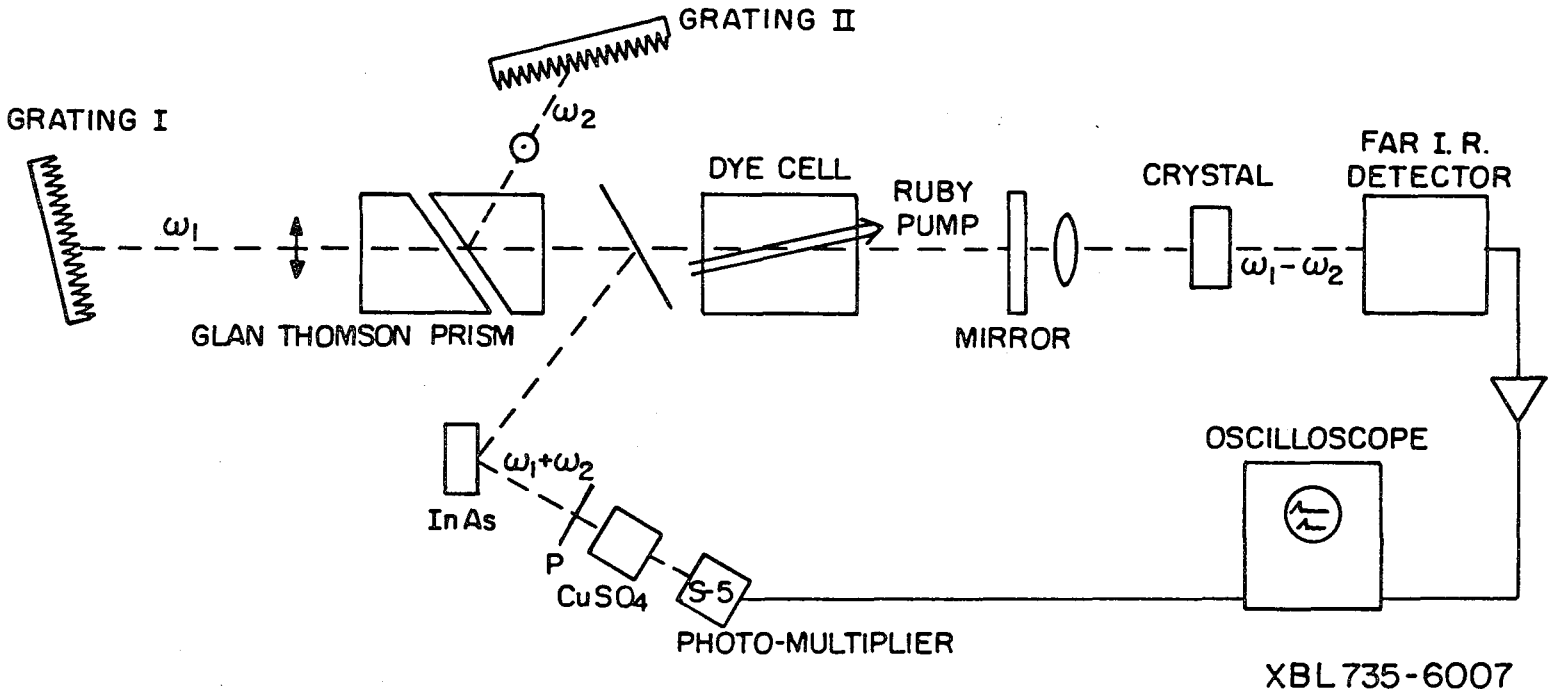
GRATING II
GRATING I
ω_2
ω_1
DYE CELL
RUBY
PUMP
CRYSTAL
FAR I. R.
DETECTOR
$\omega_1-\omega_2$
GLAN THOMSON PRISM
MIRROR
OSCILLOSCOPE
$\omega_1+\omega_2$
InAs
P
$CuSO_4$
S-5
PHOTO-MULTIPLIER
XBL735-6007

Fig. 24.

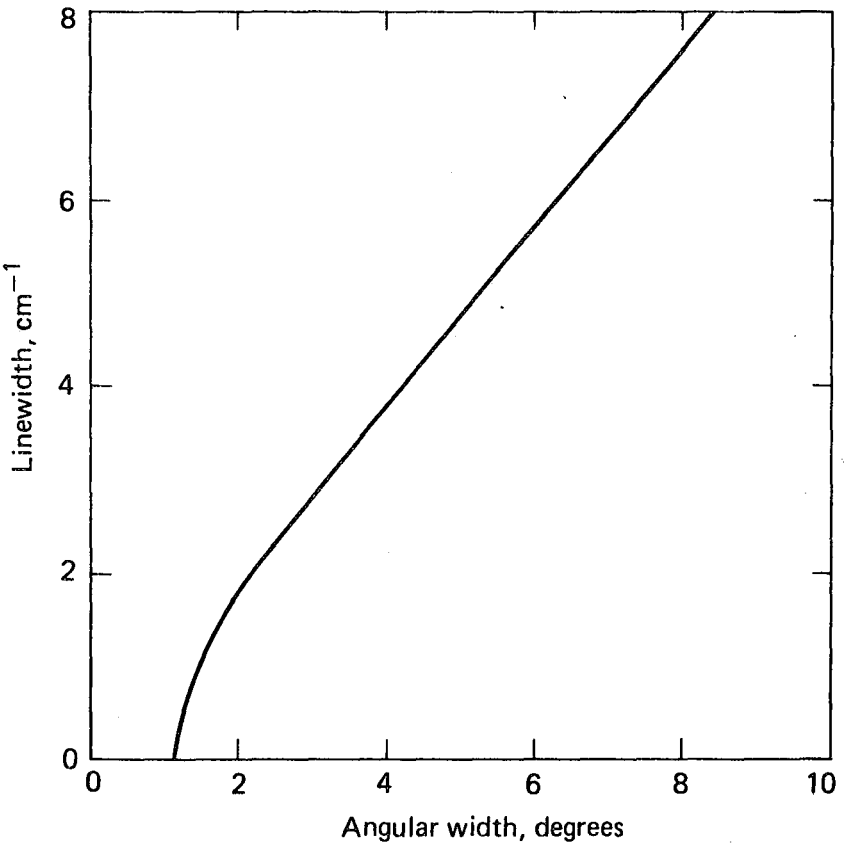

Fig. 25.

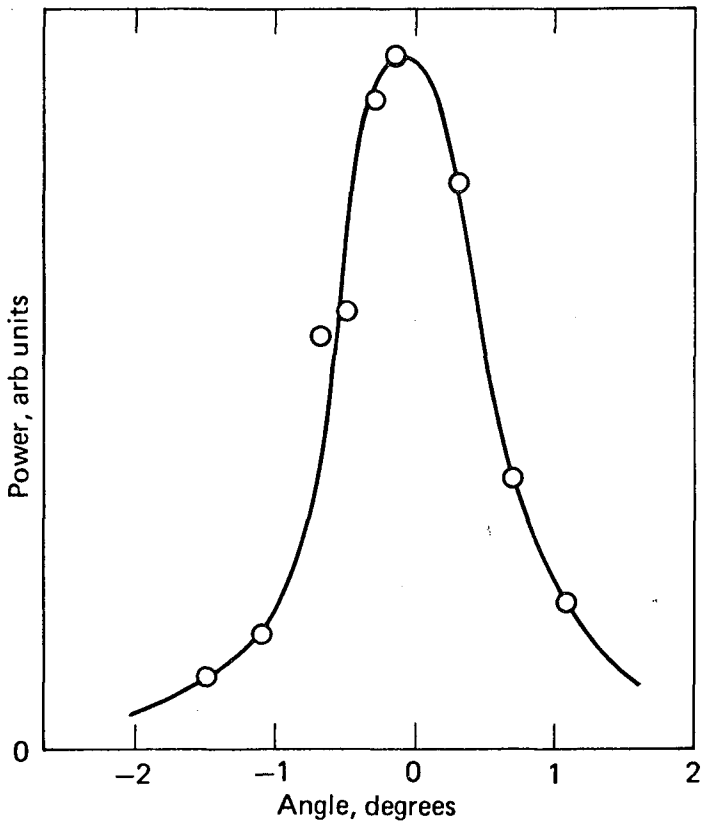

Fig. 26.

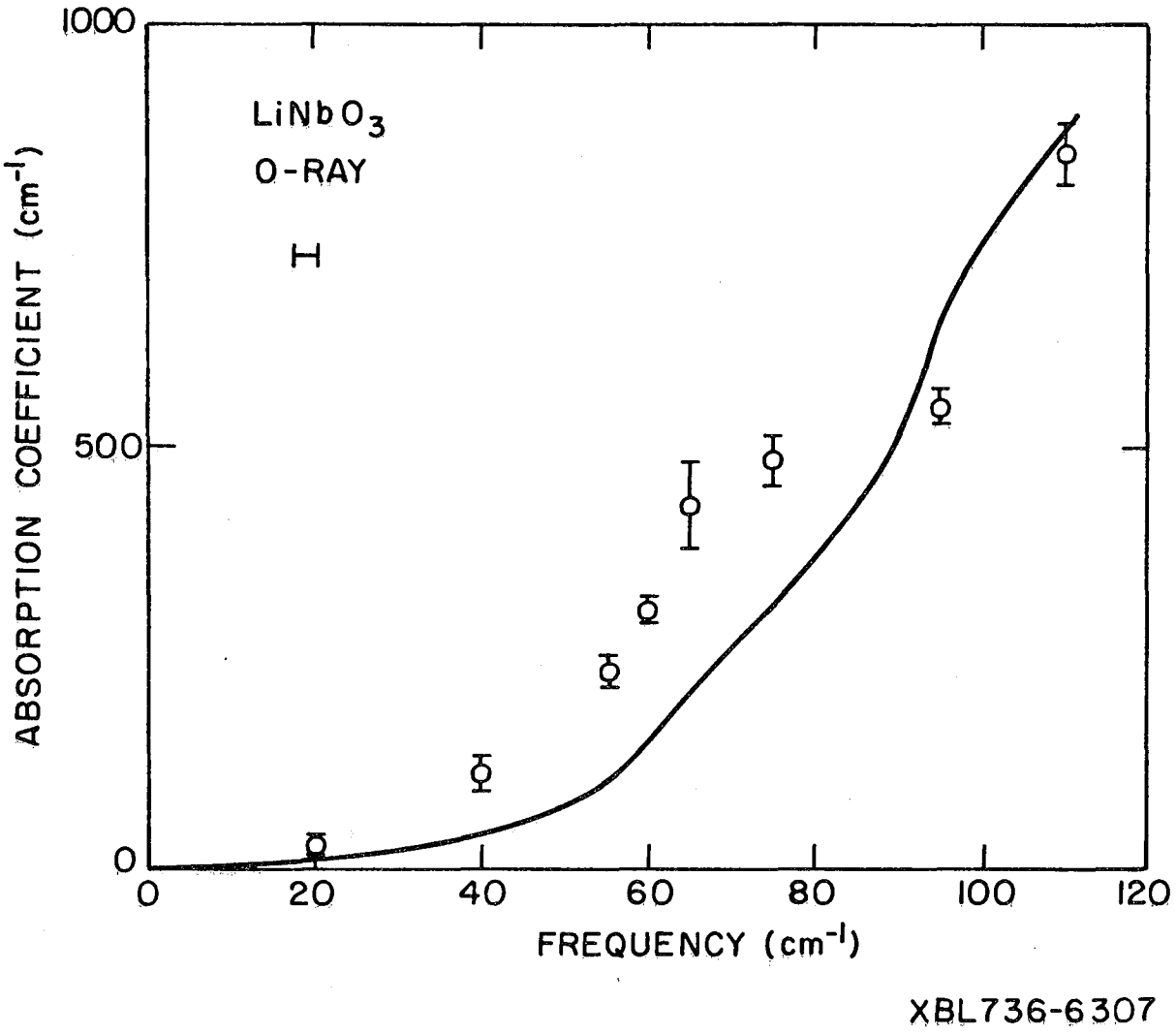
1000
500
0
LiNbO3
O-RAY
ABSORPTION COEFFICIENT (cm-1)
0
20
40
60
80
100
120
FREQUENCY (cm-1)
XBL736-6307

Fig. 27.

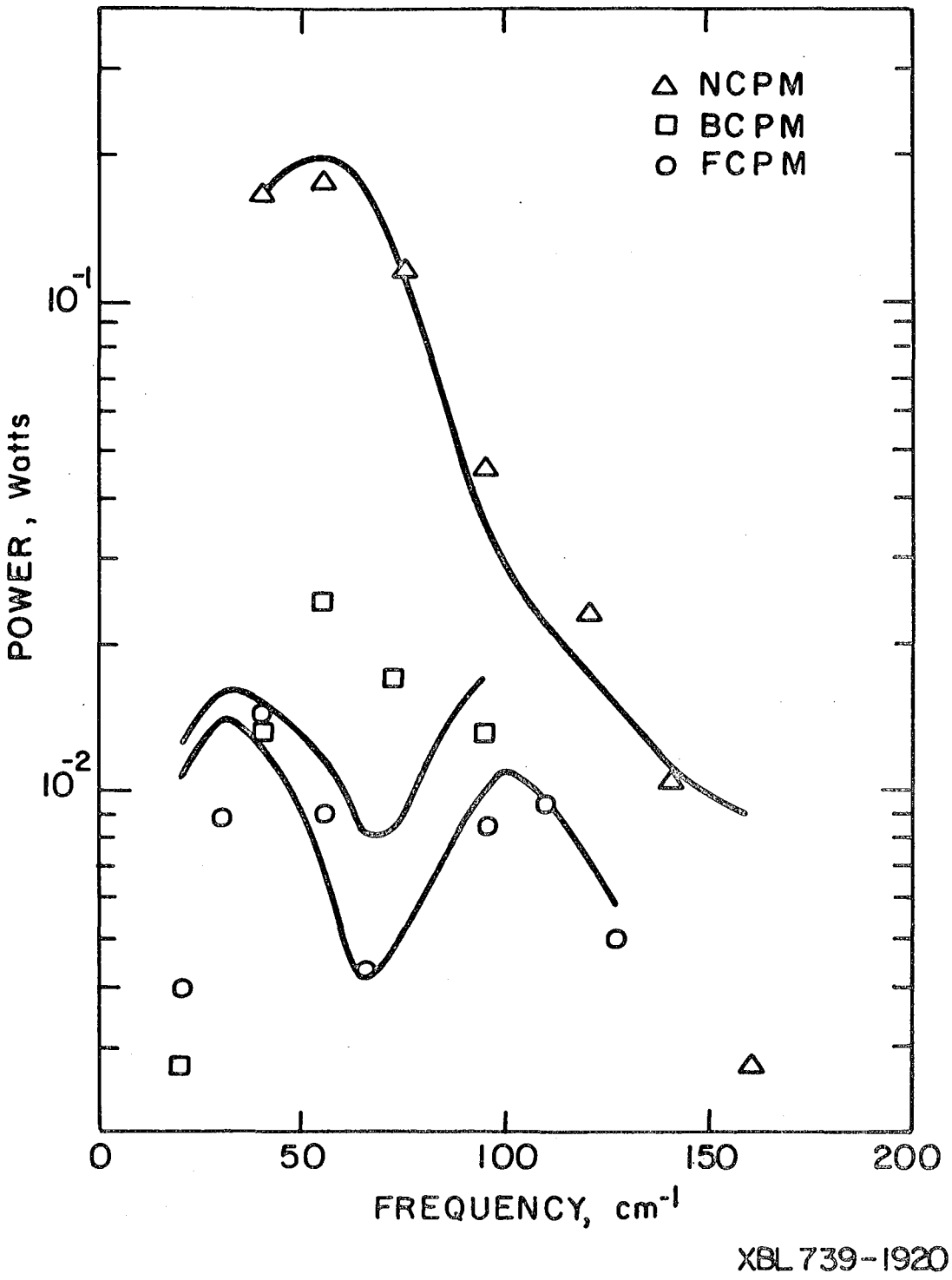

Fig. 28.

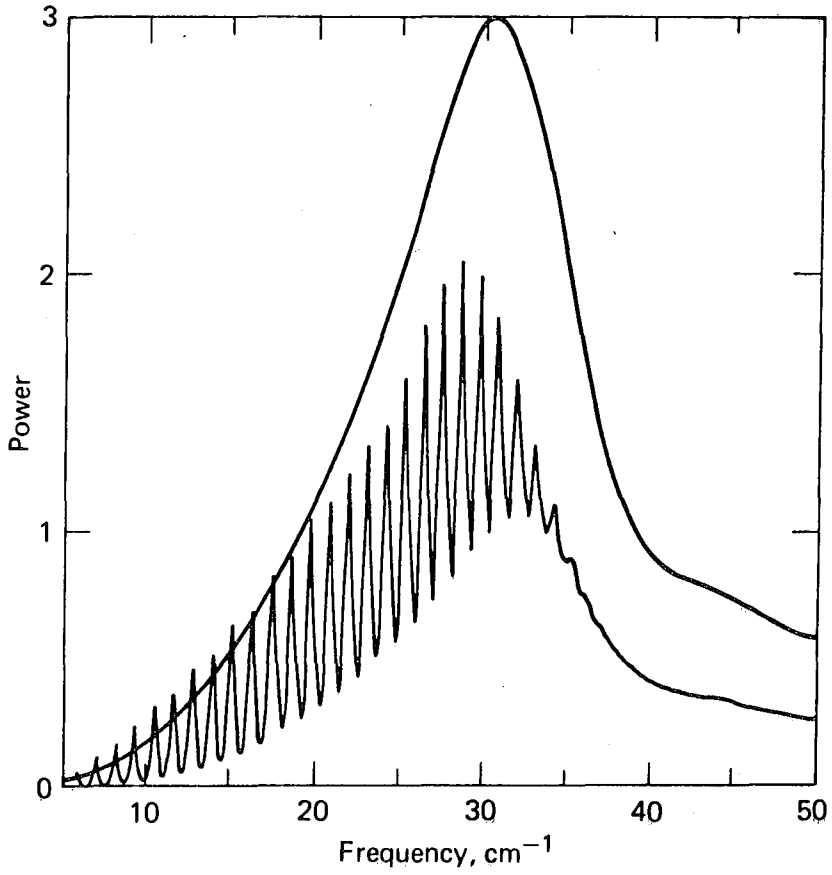

Fig. 29a.

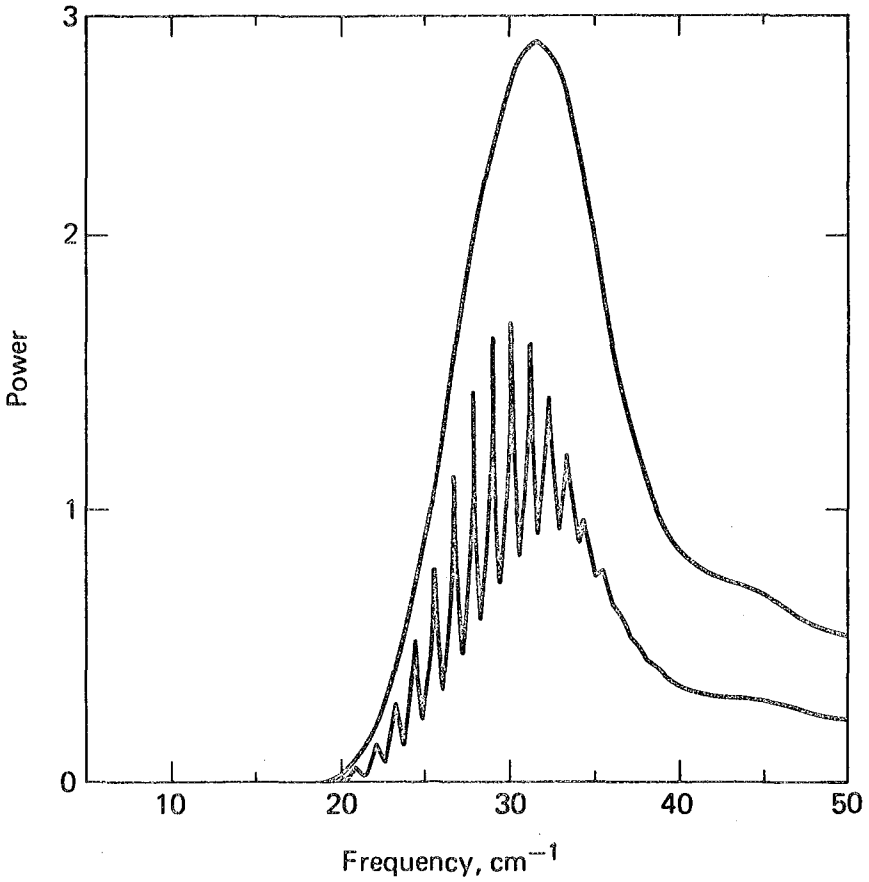

Fig. 29b.

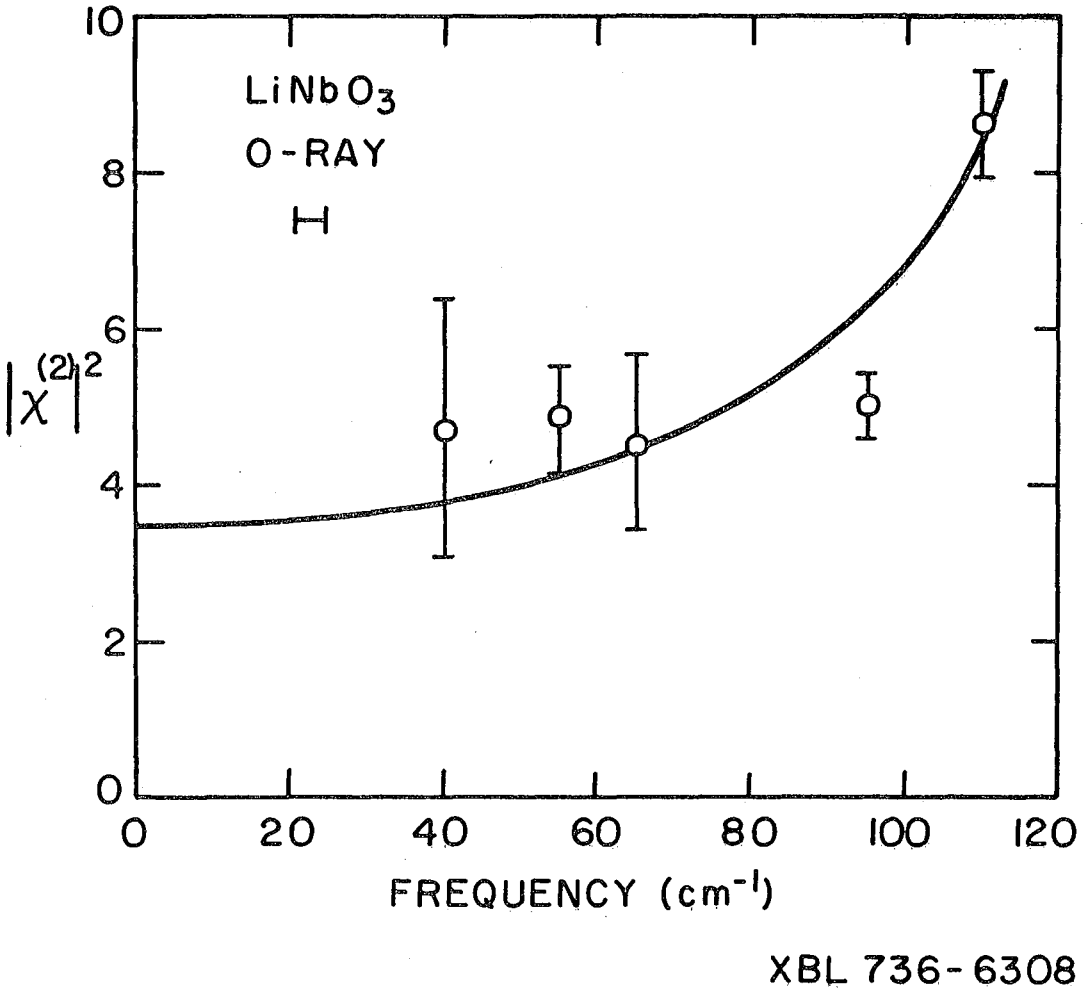
LiNbO3
O-RAY
H
$|\chi^{(2)}|^2$
10
8
6
4
2
0
0
20
40
60
80
100
120
FREQUENCY (cm^{-1})
XBL 736-6308

Fig. 30.

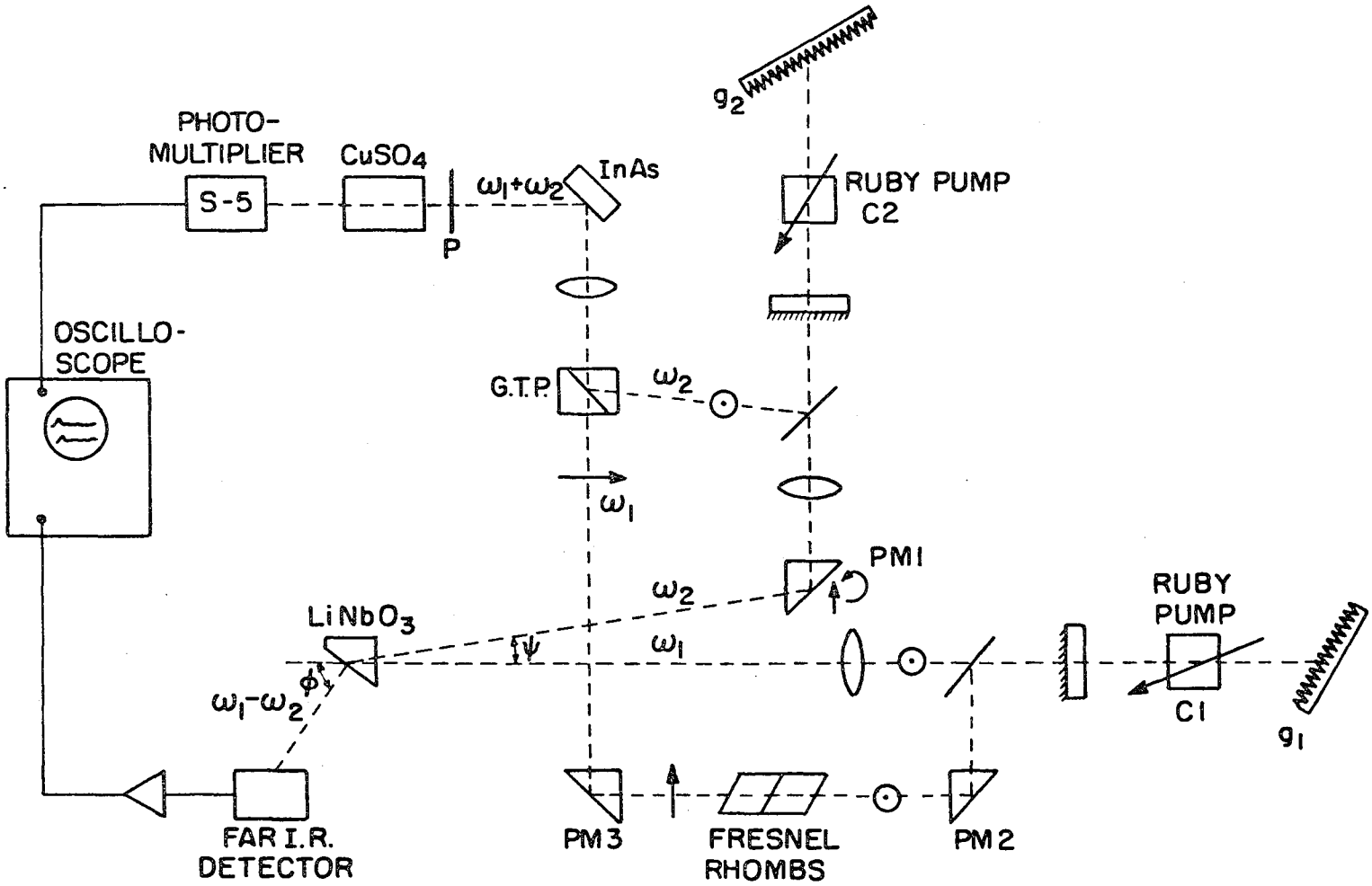

XBL 736-6306

Fig. 31.

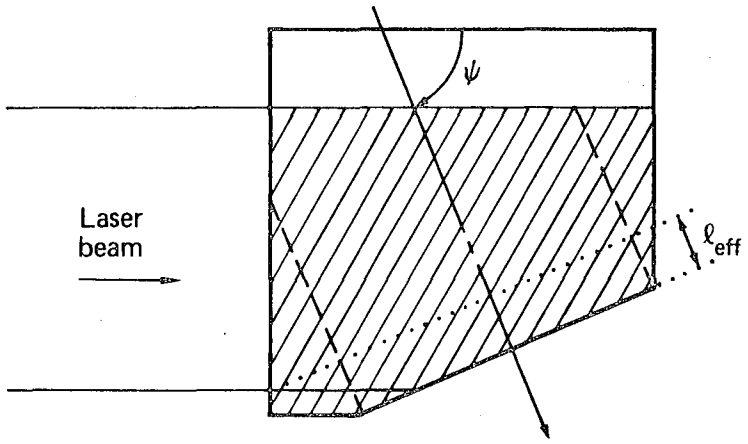

Fig. 32.

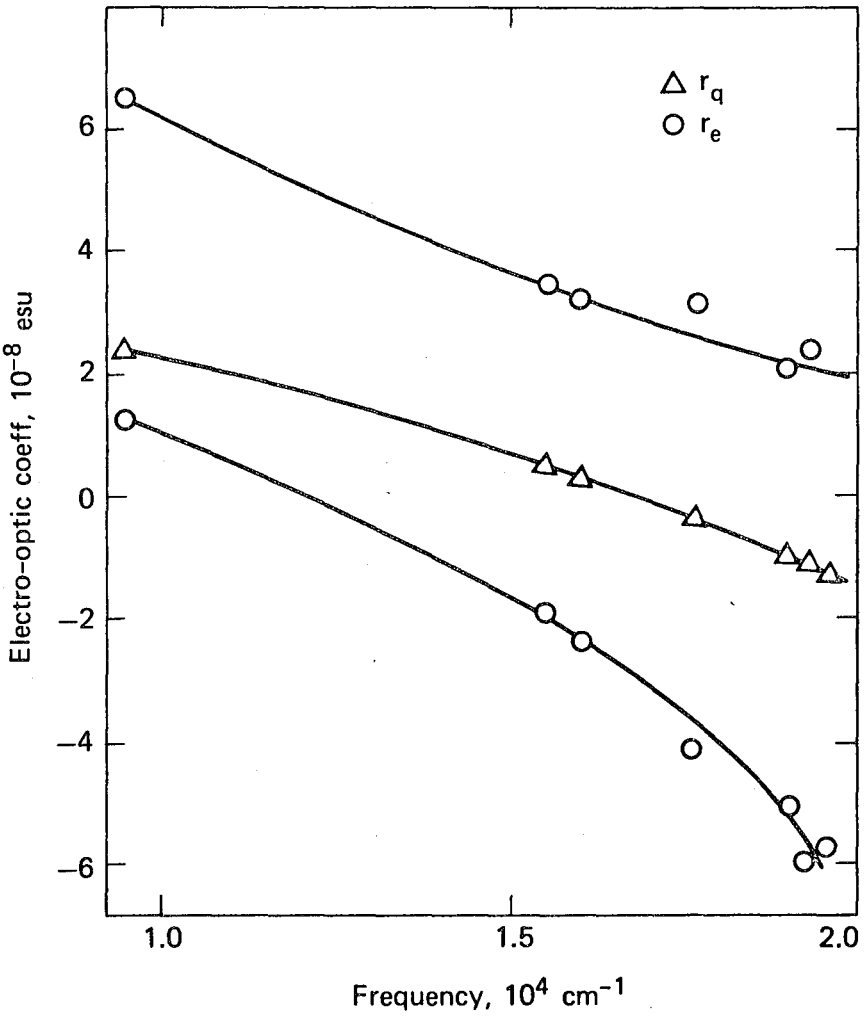
△ r_q
○ r_e
6
4
2
0
−2
−4
−6
Electro-optic coeff, 10^{-8} esu
1.0
1.5
2.0
Frequency, 10^4 cm^{-1}

Fig. 33.

This report was done with support from the United States Energy Research and Development Administration. Any conclusions or opinions expressed in this report represent solely those of the author(s) and not necessarily those of The Regents of the University of California, the Lawrence Berkeley Laboratory or the United States Energy Research and Development Administration.